„Rock Physics Template“- Application on different rocks and different scales

Masterarbeit

Zur Erlangung des akademischen Grades eines Diplomingenieurs
der Studienrichtung Angewandte Geowissenschaften
an der Montanuniversität Leoben

BSc. Judit Pupos

eingereicht am
Lehrstuhl für Angewandte Geophysik
im Department Angewandte Geowissenschaften und Geophysik

Leoben, September 2014

EIDESSTATTLICHE ERKLÄRUNG

Ich erkläre an Eides statt, dass ich diese Arbeit selbständig verfasst, andere als die angegebenen Quellen und Hilfsmittel nicht benutzt und mich auch sonst keiner unerlaubten Hilfsmittel bedient habe.

AFFIDAVIT

I declare in lieu of oath, that I wrote this thesis and performed the associated research myself, using only literature cited in this volume.

September 2014

Judit PUPOS

Acknowledgements

While working on this diploma thesis I have been supported by many people. I would like to express my deepest appreciation to all those who provided me the possibility to complete this thesis.

First of all, I would like to express my sincere gratitude towards my supervisors Hon.Prof.Dr.rer.nat.habil. Jürgen Schön and Ass.Prof.Dr. Nina Gegenhuber. I benefited substantially from their guidance and advice and was supported whenever and wherever they could. I am happy to have had the opportunity to work with them.

Further, I would like to offer my special thanks to Emma Tyler, who impressed me with her knowledge and willingness to share it at any time. I am deeply grateful to her for her technical and amicable support.

Additionally I would like to thank the department of Reservoir Geophysics of the OMV AG, especially Linda Kirchberger for giving me the opportunity to consolidate my knowledge in geophysics and work in a professional and friendly environment.

Finally, I wish to thank my parents for their support and encouragement throughout my study.

Abstract

The Rock Physics Template (RPT), which is a cross plot of acoustic impedance versus ratio of compressional and shear wave velocity, is used as a tool for efficient lithology- and pore fluid interpretation of well log data and elastic inversion results. In this study were investigated (a) results of laboratory measurements at dolomite, limestone and sandstone samples from the Vienna Basin and (b) processed data in well-log and seismic scales. Different model calculations, such as Kuster and Toksöz inclusion model, Hashin-Shtrikman bounds and Gassmann fluid substitution model, for dry and brine saturated samples were carried out to achieve a better understanding about the elastic properties of the investigated rocks. It was observed that the calculated model lines describe our data set similarly in scale of laboratory measurements and well-logs. Using laboratory results and interpreted well logs, RPTs, which include the geological constraints of the Vienna Basin, were created for sandstone and carbonate rocks. Simultaneous AVO inversion was performed that delivers absolute acoustic impedance, v_p/v_s (or shear impedance) and density cubes. The elastic inversion results were also used to verify the validity of the generated RPTs. It could be considered that generation of RPTs for siliciclastic system provides a better result than for carbonate system. Possible explanations can be the low porosity, a more complex pore system of the carbonates and influences of the mineral matrix.

Zusammenfassung

Das Rock Physics Template (RPT), welches ein Diagramm der akustischen Impedanz in Abhängigkeit von Kompressions- und Scherwellengeschwindigkeit ist, wird als ein Werkzeug für die effiziente Lithologie- und Porenflüssigkeitsinterpretation von Bohrlochdaten und elastischen Inversionsergebnissen verwendet. Es wurden (a) Ergebnisse von Labormessungen an Dolomit-, Kalkstein- und Sandstein-Proben aus dem Wiener Becken und (b) verarbeitete Daten von Bohrlochprofilen und seismischen Skalen untersucht. Verschiedene Modellrechnungen, wie das Kuster und Toksöz Inklusionsmodell, die Hashin-Shtrikman Grenzen und das Gassmann Flüssigkeitssubstitutions Modell für trockene und mit Wasser gesättigte Proben wurden durchgeführt, um ein besseres Verständnis über die elastischen Eigenschaften der untersuchten Gesteine zu erhalten. Es wurde beobachtet, dass die berechneten Modelllinien unserer Daten sowohl bei Labormessungen, als auch bei Bohrlochdaten gut übereinstimmen. Mit Laborergebnissen und interpretierten Bohrlochdaten, welche die geologischen Rahmenbedingungen des Wiener Beckens erfassen, wurden RPT´s für Sandstein und Karbonatgesteine erstellt. Gleichzeitig wurde eine AVO Inversion durchgeführt, welche die absolute akustische Impedanz, v_p/v_s (oder Scher Impedanz) und Dichte cubes liefert. Die elastischen Inversions-Ergebnisse wurden auch verwendet, um die Gültigkeit der erzeugten RPT's zu überprüfen. Es kann erwogen werden, dass die Erzeugung von RPT's für siliziklastische Systeme zu besseren Ergebnissen führen als für Karbonat-Systeme. Mögliche Erklärungen hierfür können die geringere Porosität, ein komplexeres Porensystem der Karbonate und der Einfluss der Matrixminerale sein.

Contents

1. Introduction

The interpretation of seismic data in terms of elastic properties is one of the most important tools for reservoir geophysicists. Rock physics represents the link between geologic reservoir parameters (for instance porosity, clay content, sorting, lithology, saturation) and seismic properties (e.g. v_p/v_s ratio, density, elastic moduli).

In this study, we build up a rock physics template using laboratory results and borehole data and plot it along with the inverted elastic properties to aid the efficient interpretation. The Rock Physics Template (RPT) was first published by Ødegaard and Avseth (2004) for sandstone and shale. RPT is used as a tool for efficient lithology- and pore fluid interpretation of well log data and elastic inversion results. Authors present model calculations to describe the relationship between v_p/v_s ratio and acoustic impedance. They mention that the RPT is basin-specific and influenced by local geological factors. Gupta (2012) presented data for the sand reservoir and mentioned that the interpretation worked well, especially for the thin and discrete reservoirs.

Chi and Han (2009) presented their constructed RPT for the deep-water Gulf of Mexico. Inverted elastic properties as results of seismic inversion were plotted in cross-plots with the rock physics template. They state that the cross plots provide the opportunity to clearly delineate the lithology and fluid content. Moreover, they pronounced that the lithology and fluid content of undrilled areas can be predicted using the drilled well information as a reference if the undrilled areas have a similar geological deposition environment to the drilled area.

Ba (2013) used the rock physics template for gas and water saturated carbonate reservoirs. They compare data in different scale (ultrasonic, sonic and seismic data) for a direct gas detection and porosity estimation. The RPT is validated through all three scales.

Seismic responses in carbonate rocks are poorly understood, however, carbonate (limestone and dolomite) reservoirs account for approximately 50% of oil and gas production worldwide (Xu, 2009).

Carbonates are characterized by a complex pore structure which controls compressional and shear wave velocity (Scotellaro and Mavko, 2008). An additional influencing factor, which was observed, is a shear weakening effect for saturated samples. This can have an impact on the geo-mechanical behaviour in a reservoir (Sharma, 2011). Therefore, laboratory measurements are important for the exploration and modelling of carbonate reservoirs (Gomez, 2007).

Rogen (2005) presented the results of chalk samples and stated that the porosity is the main controlling factor for v_p and v_s. Sharma (2006) agreed with this statement and mention as additional influencing factors: pore type, pore fluid compressibility and variation in shear modulus. The variations in shear modulus for saturated samples are also presented by Baechle (2005), where also the shear weakening effect is discussed. Especially with a lot of microporosity the shear weakening becomes observable and results in a higher v_p/v_s ratio. They also mentioned that the pore shape is not easy to quantify but is one important rock property for the elastic properties.

Model calculations for carbonate rocks –compared to clastic rocks- are more complicated as result of the diversity of pore geometries. Demonstrated at the velocity-porosity relationship of carbonates, a systematic analysis was published by Eberli (2003). Eberli (2003) noted that predominantly pore type influences the sonic velocity of the carbonate rocks. There is a general inverse porosity-velocity relationship but significant deviation occurs from this correlation for certain pore types. Frame-forming pore types such as moldic and intraframe porosity, result in significantly higher velocity values than do pore types that are not embedded in a frame such as intercrystalline and interpraticle pores (Eberli, 2003).

Xu and Payne (2009) give an overview and good solution for modelling the elastic properties for carbonate rocks, where problems still appear. They used the theory by Kuster and Toksöz (1974), the differential effective medium theory (Mavko, 2011) and the Xu and White model (1995 and 1996). Correlation between v_p and v_s for carbonates are given for instance by Catagna (1985), as a part of their mudstone study.

The main goal of this study is to construct an appropriate Rock Physics Template for the Vienna Basin using core, well-log and seismic data. Three different carbonate rock types

from Austria and core plugs (carbonates and sandstones) from different wells are selected to measure their compressional and shear wave velocity as well as the effective porosity in laboratory. Different model calculations, like Kuster and Toksöz inclusion model, Hashin-Shtrikman bounds and Gassmann fluid substitution model, for dry and brine saturated samples are carried out. Moreover, the results of the model calculations in scale of laboratory are compared with borehole data. Using laboratory results and interpreted well logs, RPTs, which include the geological constraints of the Vienna Basin, are created for sandstone and carbonate rocks. Simultaneous AVO inversion was performed that delivers absolute acoustic impedance, v_p/v_s and density cubes. The elastic inversion results were also used to verify the validity of the generated RPTs.

2. Geological overview

The Vienna Basin is the most significant petroleum oil and gas region in Austria and beyond in middle Europe. Therefore, a large number of publications provide information about the formations and geological evolution of the Vienna Basin. The basin is elongated in SW-NE direction with a length of about 200 km and a width of 55-60 km. It is located in Austria, the Czech Republic and Slovakia. It is divided into a northern and a southern part by the Danube (Figure 2.1).

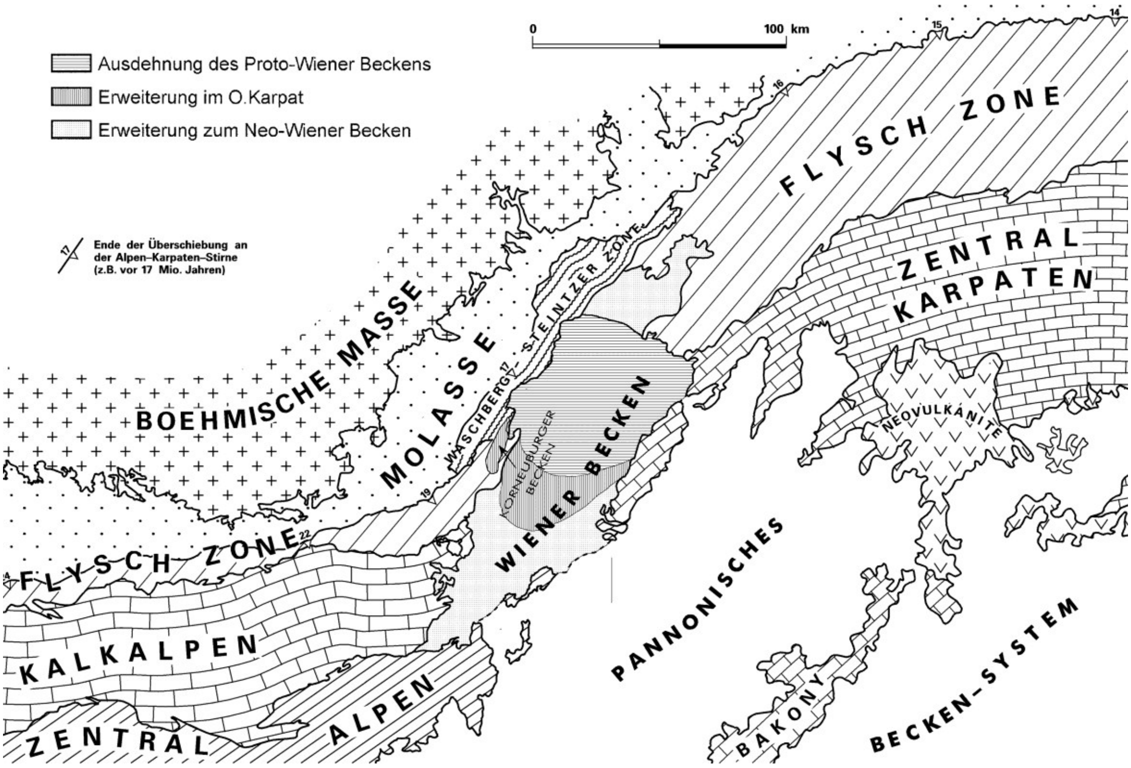

Figure 2.1. Location of the Vienna Basin within the Alpine-Carpathian thrust belt (Wessely, 2006).

If we observe the geological structure of the region, which represents the geographical area of Vienna Basin, we have to differentiate considerably between the Neogene sedimentary fill of the basin and the allochthonous thrust terrains of the Alpine-Carpathian system (Figure 2.2).

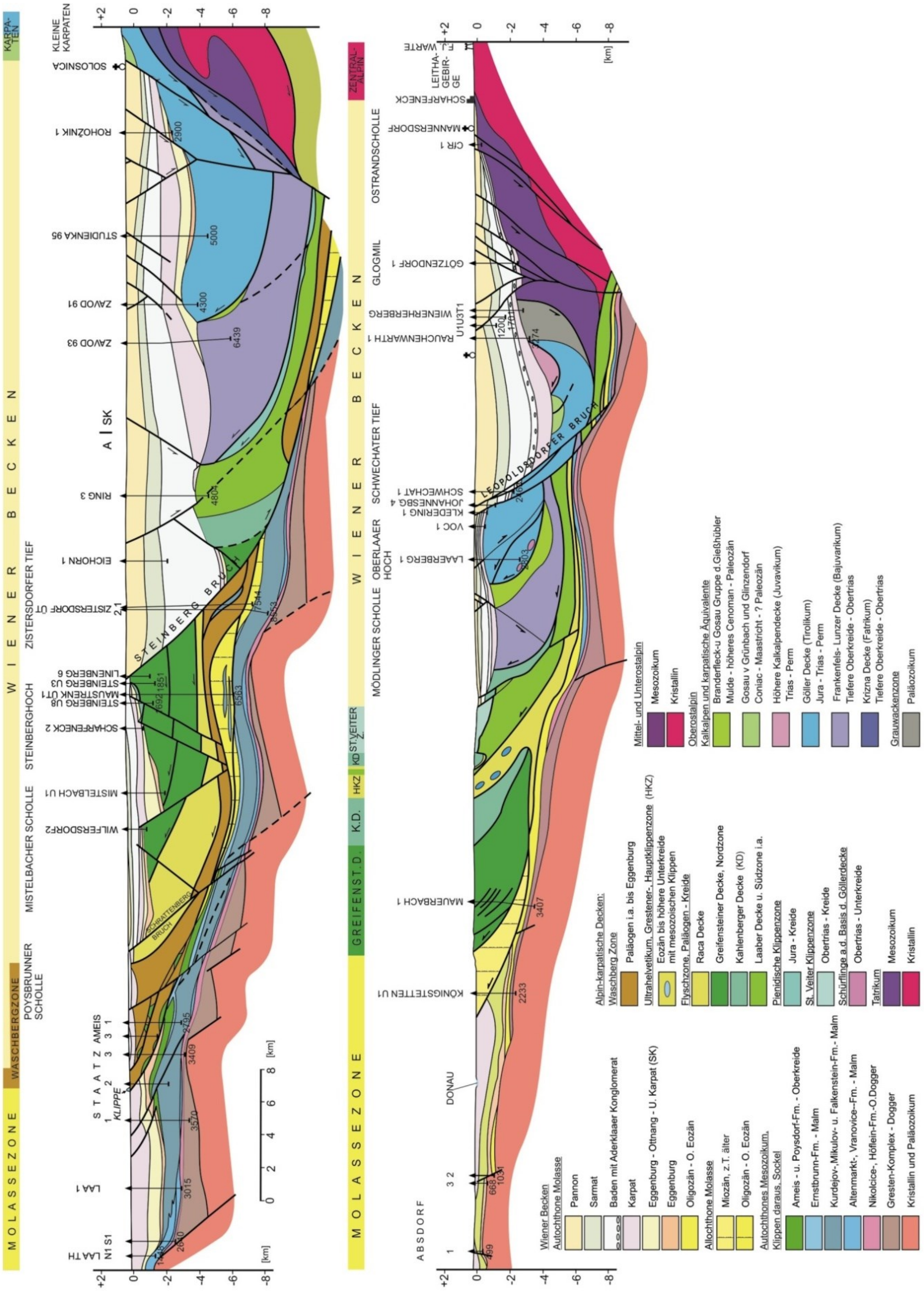

Figure 2.2. Schematic sections across the Vienna Basin (Wessely, 2006).

For over 20 million years, the Alps and the Carpathians were not separate, but formed a continuous mountain range. They originate from a common geological event which started at the end of the Jurassic period about 140 million years ago and continued with varying activities until the Neogene, until about 15-20 million years ago. During this time huge masses of rock have pushed several thousand meters in thickness over each other and formed what we see today in the Alps. Towards the end of this mountain building process strains occurred deep in the Earth's mantle in the area of today's Vienna Basin, which caused sinking of large crust parts. This sinking also extends, varying degrees, over a period of about 15 million years. The depression area was flooded by the sea, which has filled the resulting basin in conjunction with sediments from rivers coming from the Alps and the Carpathians. The influence of the open sea in geological history was varying intense at different times. Its deposits appear us today in the form of sands and sandstones, clay marl and partly as conglomerates and gravel. Also algae limestones are occasionally found.

To understand the structure and the presence of oil and natural gas deposits, it is necessary to discuss the layer arrangement and their lithological formation.

It is very clear to see how the first deposit, in the time of Eggenburgian occurs in the northern part of the basin. During the Eggenburgian a transgression (flooding) took place with marine sediments, which were mainly formed by marls and marly sandy rocks in fine rhythmic layers (Figure 2.3). The underground pressure was significant, which was formed mainly from rocks of the flysch zone (upper Cretaceous) and caused a separation and delimitation in the south of the central basin, in the area of Matzen-Spannberg.

This first marine transgression was followed by another one in upper Eggenburgian, which existed in the recent Northern Vienna basin and remained until the upper Ottnangian. The sediments as sandy-marly layers have continued. In the central basin, in the southern part of the Spannberger ridge the Bockfliesser layers occur in form of a brackish sediment which mainly consists of clay, marl and sand with interposition of rubble and gravel that build up from flysch rocks and alpine calcareous material.

The movement of the underground brought a temporary regression of the sea towards the end of the Ottnangian. In the central basin, the already existing ridge emerged even more in the area of Spannberg and causing a separation of the sediments north and south of the ridge. With the Karpatian came the renewed thrust of the sea, which means the area of the basin had lowered more. South of the Matzen-Spannberger ridge, a very high sedimentation rate of terrestrial-lacustrine rocks took place, which begins with the Gänserndorfer layers that show only a limited distribution in the area of Matzen-Protes to Fischamend. It is predominantly coarse clastic deposition- sand and conglomerates- originating from the closed basin underground. Above that a more and more transgressive layer sequence, the Aderklaa layers spread southward. The influence of limnic remained preserved and thus also sandier and in the hanging a conglomeratic Formation was built.

The movements in the underground of the Vienna Basin had increased again towards the end of the Karpatian. Strong bends and foldings occurred and also an erosion of the already deposited sediments took place. At that time, the mountain-forming movements in the Alps and Carpathians were in their final stages. Thus a strong erosion is released, while a large amount of rubble from the Alps and Carpathian mountains were deposited in connection with a further sinking of the Vienna Basin. This rubble exists today in the form of the Aderklaa conglomerate. The mentioned Matzen-Spannberger ridge has retained its function even at this time. The stream of rubble could not spread northwards over it. In that area, abundant sand and clay complexes were deposited at the same time (Figure 2.3).

With the turn of the Karpatian to the Badenian, the present-day basin placed a wide area and the sea flooded the southern part of it (Figure 2.3). A purely marine layer sequence of clay marl, moreover deposition of sand and clay marl took place varying above it.

The layers of the Badenian were followed by the deposits of the Sarmatian, consisting of interbedded strata of sand and clay marl. The marine character decreased slowly in the Sarmatian, moreover brackish influence can be found more often.

The freshening of the basin continued in the layers of the Pannonian, which lies above the Sarmatian, and is completed in the upper Pannonian. The sediments of the Lower Pannonian are similar as in the Sarmatian, so sand and clay marl, and developing in layers with predominantly sand and gravel character to the end of Middle Pannonian that then continues in the Upper Pannonian (Figure 2.3).

With the end of the Pannonian, an extensive aggradation occurred, so only rubble and gravel from different age, which were transported by the rivers from the Alps and Carpathians, were deposited at the top.

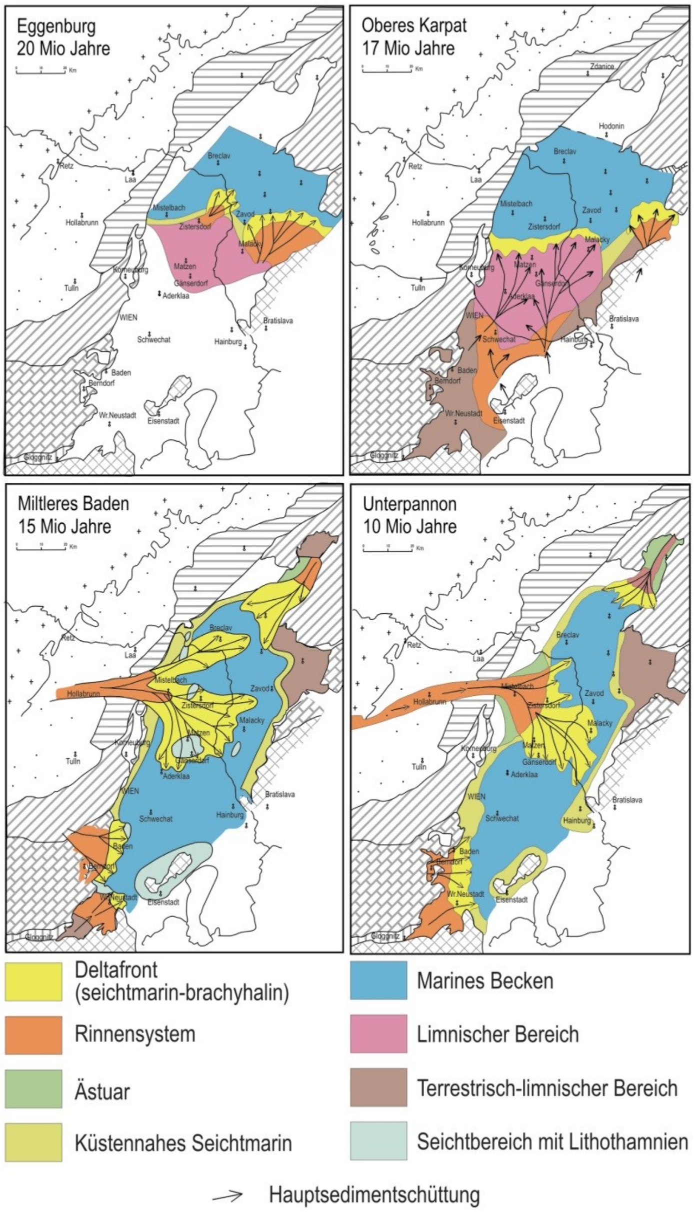

Figure 2.3. Depostirional environments that took place in the Vienna Basin during the Eggenburgian, the late Carpatians, the middle Badenian and the early Pannonian (Wessely, 2006).

The basement of the Vienna Basin is basically geologically different than the filling of the basin. The basement is composed of different zones that cross the Vienna Basin and draw in the Carpathian. The deposits of the zones were flaked from their original formation place by the movement of the Earth’s crust, additionally they were shifted. Within these zones there is a strong overthrusting characteristic. Following units can be distinguished from North to South:

- Flysch zone
- Calcareous Alps
- Greywacke zone
- Central zone

The rocks of the flysch zone, which mainly consisting of marl shale and clay in alternating sequence with calcareous sandstone, siliceous sandstone and partly glauconitic sandstone, were deposited as Turbidites in the upper Cretaceous and early Tertiary.

The Calcareous Alp is located south of the flysch zone and is overthrusting it. It is a rock complex that builds up mainly of carbonates and draws from the Alps to the Carpathian Mountains. The bulk of this carbonate rocks deposited during the Triassic. It was at that time a shelf landscape with vast lagoons, abundant reef platforms and adjoining, vast deep-sea areas.

The Limestone Alps zone has a wide distribution in the subsurface of the Vienna Basin, and there is a huge importance also for oil and natural gas enrichment. The widespread of the upper Triassic dolomite play an important role for the petroleum and natural gas extraction (Bachmayern, 1980).

3. Data

In this study different carbonates (limestone and dolomite samples) were used which were selected in Austria, namely the “Wetterstein”-dolomite, “Haupt”-dolomite and “Dachstein”-limestone. “Wetterstein”-dolomite is part of the middle Triassic and the lower part of the upper Triassic section. In contrast, “Haupt”-dolomite and “Dachstein”-dolomite are upper Triassic units of the Northern Calcareous Alps. The samples were selected using geological maps and are also classified according to these descriptions. Generally the carbonates have a low porosity (0.001-0.15 []). There are hardly any clay minerals in the samples. “Dachstein”-limestone is described as a clean limestone. “Haupt”-dolomite is mainly formed in shallow lagoon areas and shallow water zones. “Wetterstein”-dolomite is also described as a clean dolomite, also formed in shallow water zones.

The “Dachstein”-limestone is from a stone pit in Ebensee (Upper Austria). The dolomite samples are also from pits from lower Styria, whereas the “Haupt”-dolomite samples are from a pit in Gaaden/Mödling (Lower Austria) and the “Wetterstein”-dolomite samples are from a stone pit in Rohrbach (Upper Austria). All samples from the stone pits were fresh and had no alteration marks.

In the laboratory compressional and shear wave velocity for dry and saturated samples were determined. Figure 3.1 gives an overview of the measured v_p and v_s data for the three rock types (dry and brine-saturated).

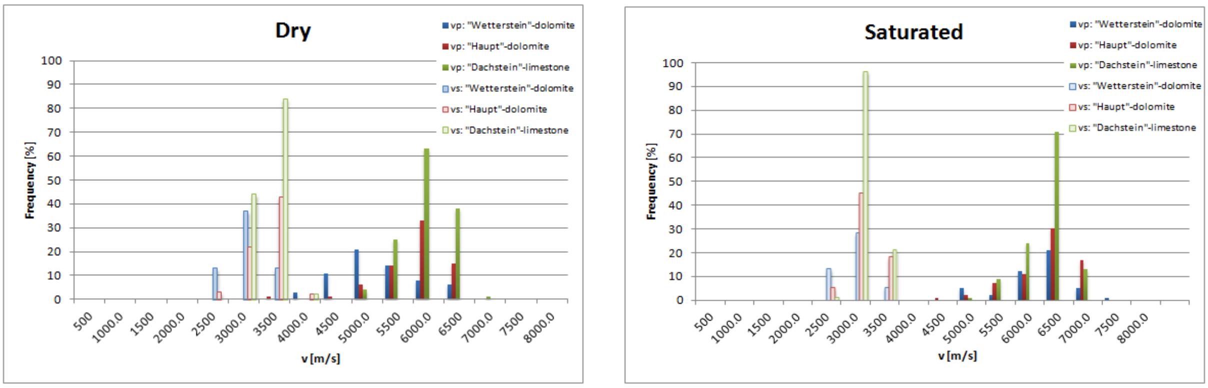

Figure 3.1. Left: v_p and v_s data for the dry samples, right: v_p and v_s data for the saturated data, green: „Dachstein“-limestone, red: „Haupt“-dolomite, blue: „Wetterstein“-dolomite.

The “Dachstein”-limestone has one high peak which means the data are homogenous and do not scatter. The v_p data for the dry data show a separation between the “Wetterstein”-dolomite and the others, which is not visible within the saturated data. The saturated data are homogenous in the data set for all three rock types. This can be explained due to the higher porosity of “Wetterstein”-dolomite.

Furthermore, we received well log data from 8 different wells and core plugs from 5 wells out of the 8 wells. From a geological point of view all wells, which were included in this study, are located in the Vienna basin, and the following map shows the position of the area under investigation (Figure 3.2). Generally in this region the sediments are layered horizontally in several areas deposition. Partly they are found in autochthonous position or they were delivered in form of alpine thrust bodies. Thus three floors are formed: the first floor consists of neogenetic sediments and represents the actual Vienna Basin. The second floor is below, allochtonous and made of Alpine-Carpathian thrustsheets. The third and the deepest floor is the autochthonous, Subalpine-Carpathian floor. All well locations are located in the Neogen of the Vienna Basin.

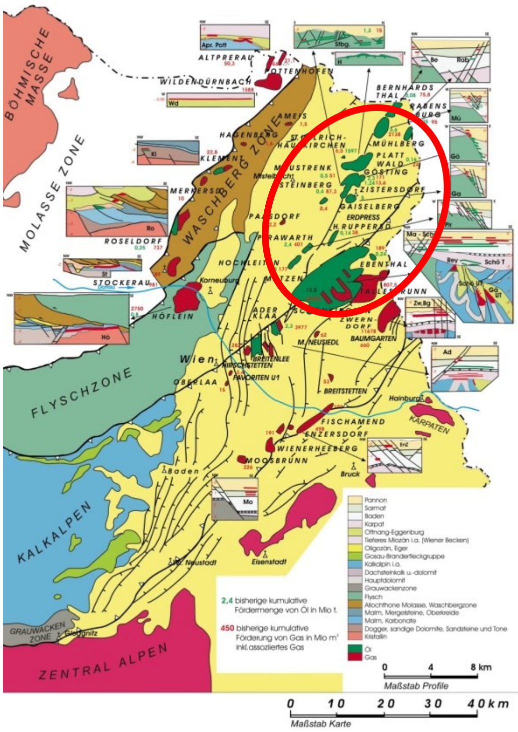

Figure 3.2. The location of the studied area within the Vienna Basin (Wessely, 2006).

Using the well logs, formation evaluation was carried out to determine the lithology and fluid content. For formation evaluation and obtaining the rock physics template we worked with the following well log data:

Table 3.1. Applied well logs.

CAL	GR	NPOR	RHOZ	DTCO	DTSM	HLLD/RD	RXOZ
Caliper	*Gamma Ray*	*Neutron Porosity*	*Bulk Density*	*Compressional Slowness*	*Shear Slowness*	*Deep Resistivity*	*Micro Resistivity*
cm	*GAPI*	*[-]*	*g/cm^3*	*us/ft*	*us/ft*	*Ohmm*	*Ohmm*

Compressional and shear velocities were computed from compressional and shear slowness. Moreover, v_p/v_s ratio, Poisson´s ratio and acoustic and shear impedance were determined using the computed compressional and shear wave velocity and the bulk density (Figure 3.3).

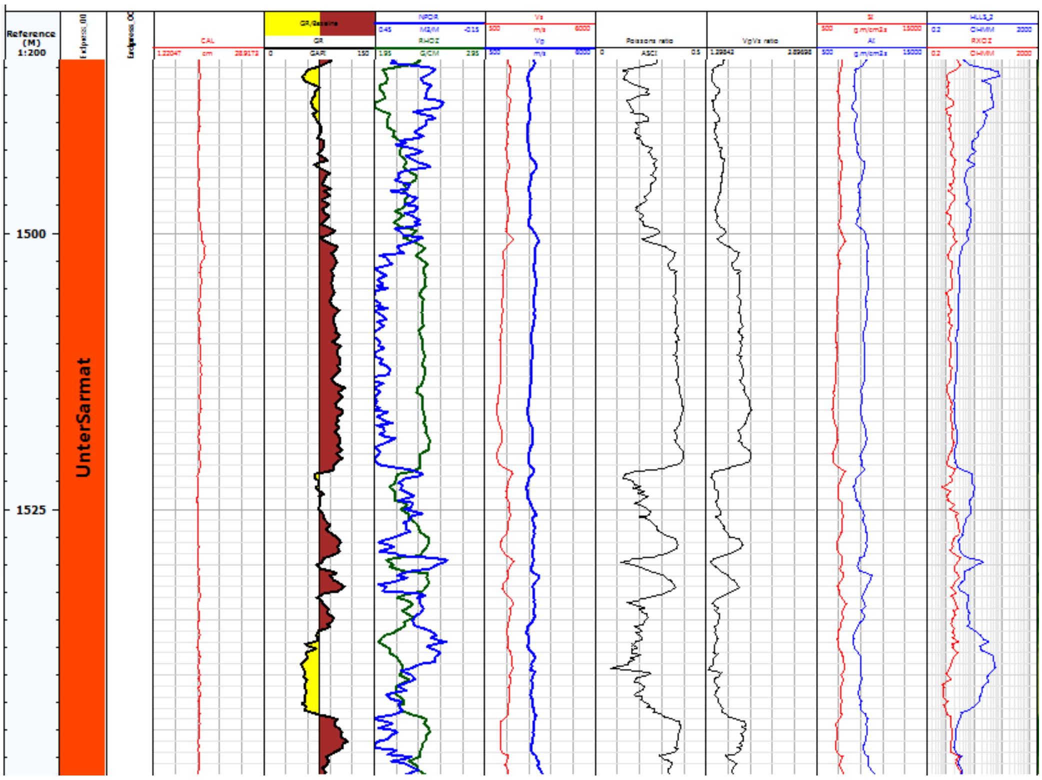

Figure 3.3. The applied well logs during this study.

The wells that were included in this study were drilled to the depth of about 3000-4000 meters. Therefore, they provide information about important formations of the Vienna Basin, for instance Aderklaa Formation, Aderklaa Conglomerate, Gänserndorfer Formation and Bockflies Formation. “Haupt”-dolomite occur also in some of the applied wells that means we had the chance to compare their data with data of the “Haupt”-dolomite from the stone pit.

As core plugs we received 41 samples from the 5 wells from the studying area, which are carbonate and sandstone samples. The carbonate types are mostly “Haupt”-dolomite and limestone. In the laboratory compressional and shear wave velocity for dry and saturated samples were determined. Figure 3.4 gives an overview of the measured v_p and v_s data for the carbonate and sandstone rocks (dry and brine-saturated).

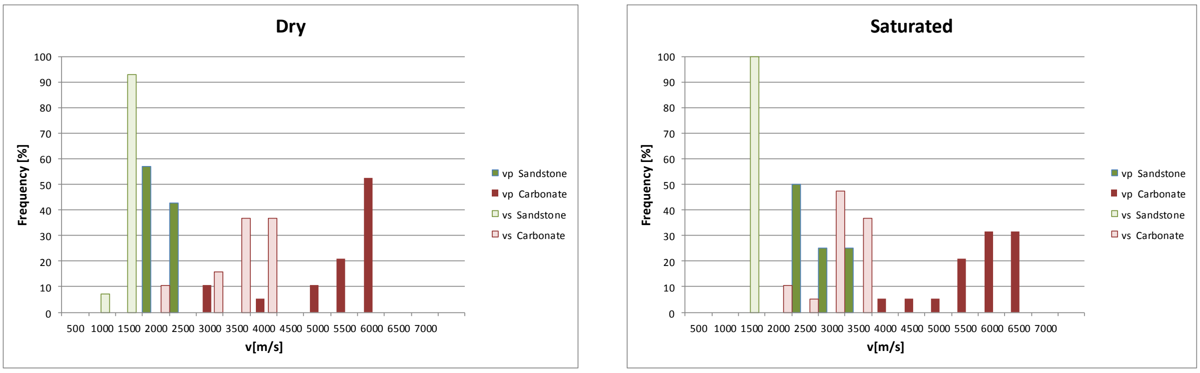

Figure 3.4. Left: v_p and v_s data for the dry samples, right: v_p and v_s data for the saturated data, red: carbonate samples, green: sandstone samples.

It can become clearly visible that the sandstone samples have a lower compressional and shear wave velocity in case of dry and saturated condition, whose reason is the higher porosity of sandstone rocks than carbonates and the higher matrix velocity of carbonates compared with sandstone (quartz). The v_s data of sandstones (dry and brine-saturated) has one high peak. However, the v_p data of sandstone show a wider distribution. The v_p data of carbonates present a different distribution in case of dry than saturated condition. The v_s values of carbonate have a similar character for dry and saturated samples.

OMV provided also a seismic dataset, which comprise of pre-stack data (offset gathers with offset ranges of 213 to 2532) and full stack dataset covering an area of approximately 7,4 km^2.The limits of the dataset are shown in Table 3.2. Additionally Figure 3.5. represents the given seismic cube within the three wells (X-001, X-006, X-016).

Table 3.2. The limites of the seismic dataset.

Direction	Minimum	Maximum	Increment	Spacing (m)
Inline	1886	1991	1	25
X-line	2851	2966	1	25

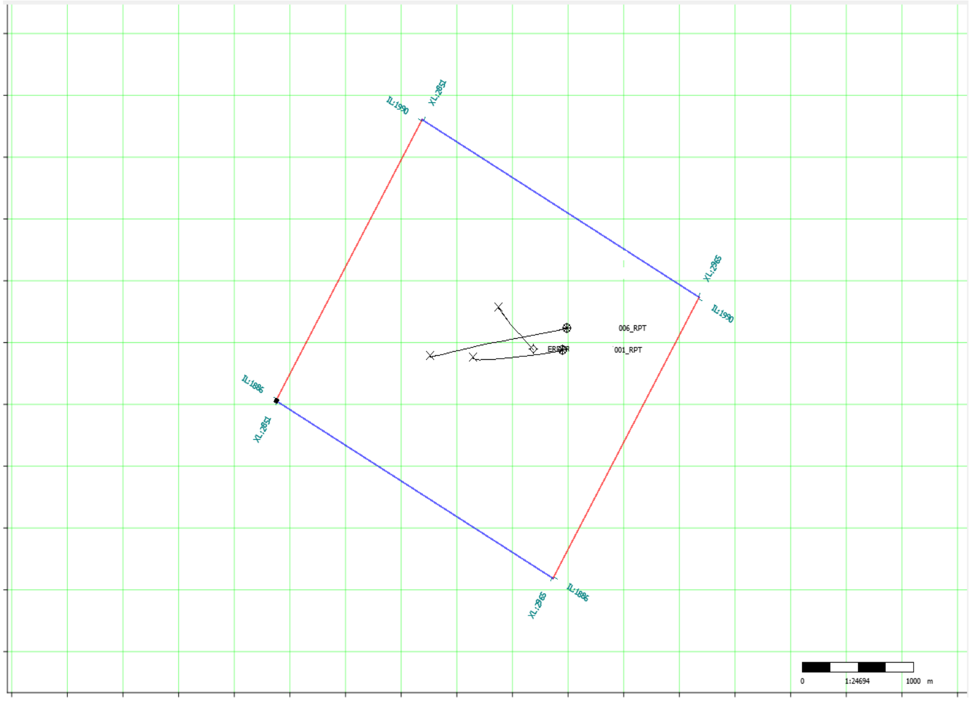

Figure 3.5. Displayed the seismic cube within the three wells (X-001, X-006, X-016).

Four interpreted horizons (11SH, 7BSH, 7UTH, 8TH) were provided by OMV. The horizons were loaded, extrapolated to fill any missing points and gentle smoothing applied.

The seismic dataset within the three wells and with the four horizons were used to perform a simultaneous AVO seismic inversion that assists to characterize the reservoir properties of the studying area.

4. Measuring Method

In the laboratory effective porosity as well as compressional (v_p) and shear wave velocity (v_s) for dry and saturated various carbonate types (limestone and dolomite, Austria) were determined. Further, I would like to introduce these rock properties and their measuring method.

4.1. Porosity and its determination

Total or absolute porosity is the total volume fraction of void space of the medium. It describes the potential storage volume of fluids and influences most physical rock properties such as elastic wave velocity, density and electrical resistivity (Schön, 2011) .Effective porosity represents that part of the pores which are interconnected and contribute to the flow of fluids. The porosity and mainly the effective porosity are one of the most important reservoir properties.

Porosity of a sediments clastic rock is primarily controlled by shape, size, distribution and arrangement of the rock grain. Difference tendencies in porosity can be observed by sandstone and carbonates. In general, porosities of sandstone tend to be lower in deeper and older rocks. In contrast, the depositional environment is affected more the porosity of carbonates than the depth of burial. The shape of the grains and the presence of intragrain porosity as well as sorting have also a large effect on porosity in carbonate sediment (Lucia, 2007).

For determining the effective porosity of the samples bulk and grain densities were measured. The bulk density is the mean density of the considered rock volume which includes also the pores. The grain density, also known as a matrix density is the density of a rock or mineral with no porosity. Two types of measurements were carried out to get these values.

First, the buoyancy method was used which is based on the principle of Archimedes. By this technique the saturated samples submerged in a bath of brine and the increase in weight of the bath was observed.

Firstly, the samples were dried at 105°C for 12 hours and weighted. Afterwards they were saturated with salt water (1g NaCl and 1l distilled water) under vacuum overnight. The saturated samples were weighted in air and then again once immersed. Using the following formula the effective porosity of the samples was calculated:

$$\phi = \frac{m_{s,a} - m_d}{m_{s,a} - m_{s,w}}$$

where $m_{s,a}$ is the mass of the saturated sample in the air,

m_d is the mass of dry sample and

$m_{s,w}$ is the mass of the saturated sample under buoyancy.

The advantage of this method is that the volume of the plug does not play an important role. Therefore the result is not influenced by the deviation of the sample volume from the cylinder volume.

Secondly, helium pycnometer was used which is a fully automated measuring instrument for determining the volume and grain density of materials. This measurement is based on the Boyle-Mariotte's law which describes how the pressure of a gas tends to decrease as gas expands.

In the first step we have to weight our samples, because the mass of the dry sample is one of the inputs which is needed to start with pycnometer measurement. Then the sample is placed in the helium-pycnometer which uses helium with well-known density and volume at the determined pressure. Subsequently the effective porosity of the rock can be defined easily from the calculated bulk density (ρ_{bulk}) and the measured density of grain ($\rho_{(grain)}$) by using the following formula:

$$\phi = \left[1 - \frac{\rho_{bulk}}{\rho_{grain}}\right] \times 100$$

4.2. Compressional and shear wave velocity and their determination

Compressional (longitudinal) and shear (transversal) wave velocities, the elastic properties of an isotropic material can be described by theory of elasticity. Moreover, if the longitudinal and transversal velocities are determined and the bulk density is known from measurement, the elastic parameters such as Young's modulus (E), compressional wave modulus (M), bulk compressional modulus (k), shear modulus (µ) and Poisson's ration (ν) can be calculated.

Just like using two well-known elastic parameters of the media compressional and shear wave velocities can be also determined by using the following equations (Schön, 2011):

$$V_P = \sqrt{\frac{M}{\rho}} = \sqrt{\frac{E(1-\nu)}{\rho(1+\nu)(1-2\nu)}} = \sqrt{\frac{\lambda + 2\mu}{\rho}} = \sqrt{\frac{k + \left(\frac{4}{3}\right)\mu}{\rho}}$$

$$V_S = \sqrt{\frac{\mu}{\rho}} = \sqrt{\frac{E}{\rho 2(1+\nu)}}$$

The velocity is a function of rock rigidity that is a function of a several variables such as lithology, porosity and pore type (Lucia, 2007). The two body wave velocities of a rock depend mainly on the solid rock skeleton and the pores, fractures and cracks that exist in the rock. Some tendencies can be mentioned like increasing porosity decreases both wave velocities. The type of pore fluid (gas, fluid) affects more strongly the compressional wave velocity than the shear velocity. As it is known that fluids do not have a shear resistance and the shear modulus of fluids is zero (Schön, 2011).

A broad range of velocity is shown by sedimentary rock, by denser (lower porosity) rock high velocities can be measured than the porous, gas-bearing samples.

The following figure (Figure 4.1) shows the principle of the measurement of body waves. An ultrasonic device was used to determine the velocities of dried and saturated (1g NaCl with 1 liter distilled water) core samples (diameter=1 inch, length about 2.2 cm). The sample is located between transmitter and receiver (UPG-S and UPE-S, Geotron Elektronik, Germany) with a contact agent and a pressure of 2bar is applied. A pulse generator sends signal spikes to the transducer, and simultaneously a “trigger signal” is sent to the recording device to tell it when the pulse was sent. The transducer active element is excited and sends a mechanical pulse across a specimen, where it is received by a second identical sensor. The mechanical signal is converted into electrical voltage. The oscilloscope records the received pulse, as well as the start time from the trigger.

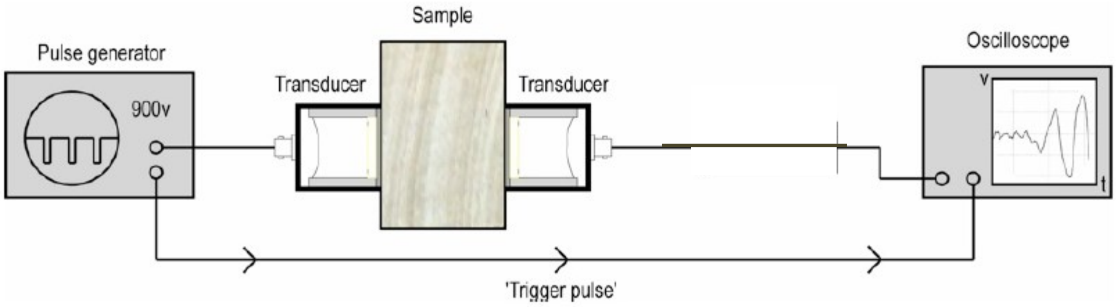

Figure 4.1. Principle of ultrasonic measurement.

Firstly, we measure a dead time that means that without a sample a sent signal is recorded after a short delay time as result of electrical-mechanical signal conversion. The frequency and the voltage of the sent signal are 80 kHz and 9V. All measurements are corrected for dead time. Probes show a primary low amplitude onset which indicates the compressional wave and a secondary high amplitude onset that indicates the shear wave. This property of samples assists in defining both body wave velocities with one measurement under identical conditions.

The signal of the measurement looks similar as a seismogram, thus the onset of v_p and $v_{S,}$ respectively are detected with the Akaike Information Criterion Picker (AIC). AIC is an autoregressive technique which is based on the assumption that the seismogram can be divided into locally stationary segments as an autoregressive (AR) process and the intervals before and after the onset are two different stationary processes (Sleeman and Eck, 1999). A phase onset can be identified by the position where the AIC-values show a minimum in the least-square sense (Gegenhuber, Steiner-Luckabauer, 2012).

As v_p and v_s are measured, the v_p-v_s relations can be determined that are the key to the determination of lithology from seismic or sonic log data as well as for direct seismic identification of pore fluid using, for instance, AVO analysis (Mavko, 2011).

5. Interpretation of the results of laboratory measurements

For modelling of RPTs the first step is to calculate velocity-porosity trends for the expected lithologies, for various burial depths, and this requires geological and petrophysical input. Our lab-based rock physics results are also used as input to the generation and validation of RPTs. In this section I present the results of porosity as well as compressional and shear wave velocity measurements. Additionally, bulk and shear modulus, acoustic and shear impedance, Poisson’s ratio were computed by using the measured values.

To demonstrate the difference between the results from the two porosity measurements a cross-plot is used (Figure 5.1). If the two methods would give the same values, all data points would lie on the diagonal line (black). The cross-plot dots also represent the different lithological groups of samples. It can be observed that in most cases the results of the helium pycnometer measurements reach higher values than the measured values by using the Buoyancy process. The reason of this observation can be based on the difference in pore throats dimensions and the difference in the size of helium and water molecules. We assume that in the majority of cases the pore throats are as big so the helium molecules can flow through them but the water molecules are too big to enter to that pores.

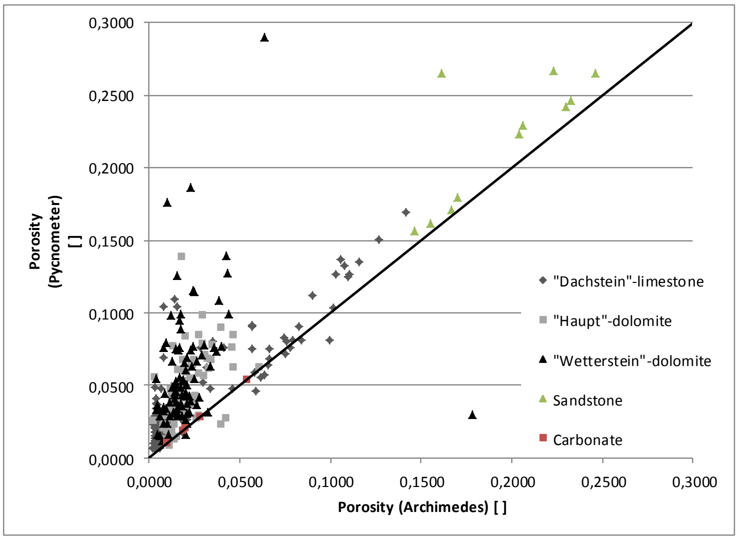

Figure 5.1. Porosity from helium pycnometer versus porosity measured with the principle of Archimedes for different carbonates and sandstone.

Figure 5.1 shows the results of the porosity measurements. It can be seen that the porosity of the sandstone samples varies from 15% to 26%, and the porosity of the carbonate samples ranges from nearly zero to about 15%. Furthermore, the porosity values which based on the principle of Archimedes are used for the next cross-plots.

Porosity is the most important factor controlling sonic velocity. However, pore type, pore fluid compressibility and variation in shear modulus due to saturation are also important factors for velocities in carbonate rocks (Baechle, 2005). The relationship between compressional- and shear velocities and porosity for dry and saturated samples is shown in Figure 5.2 and Figure 5.3.

The lithologic and mineralogic influence upon velocity can be seen in the cross-plots, as the clastic and carbonate rocks can be differentiated easily. Compressional wave velocities show a stronger dependence on porosity as compared to shear wave velocity. However, there is a lot of scatter in data, which indicates the influence of other variables on velocities apart from porosity, like mineral composition, grain contact, and pore shape.

Many compressional velocities of our brine-saturated samples are higher than the dry samples, and most shear wave velocities decrease in the saturated samples. Shear velocity decreases mostly, if the pores are saturated with brine instead of gas, because water has a higher density than gas.

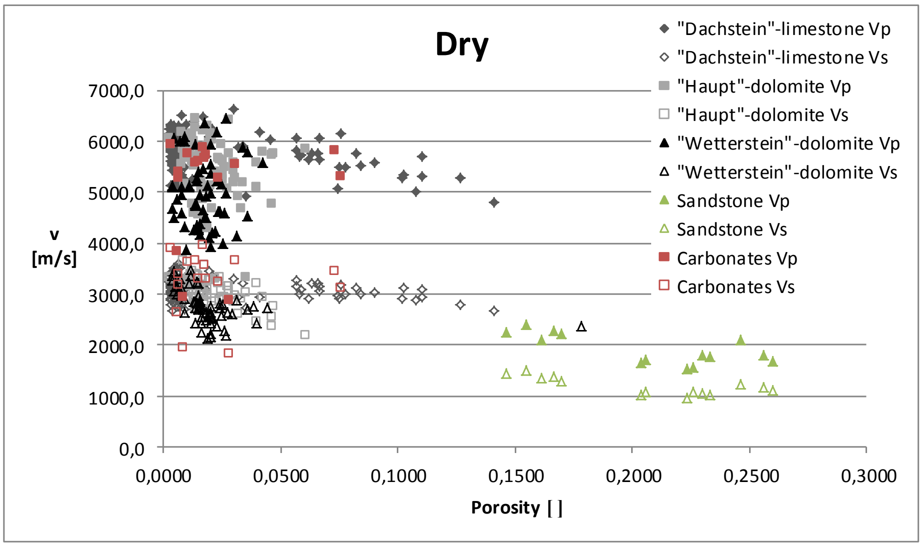

Figure 5.2. Compressional and shear wave velocities versus porosity for dry samples.

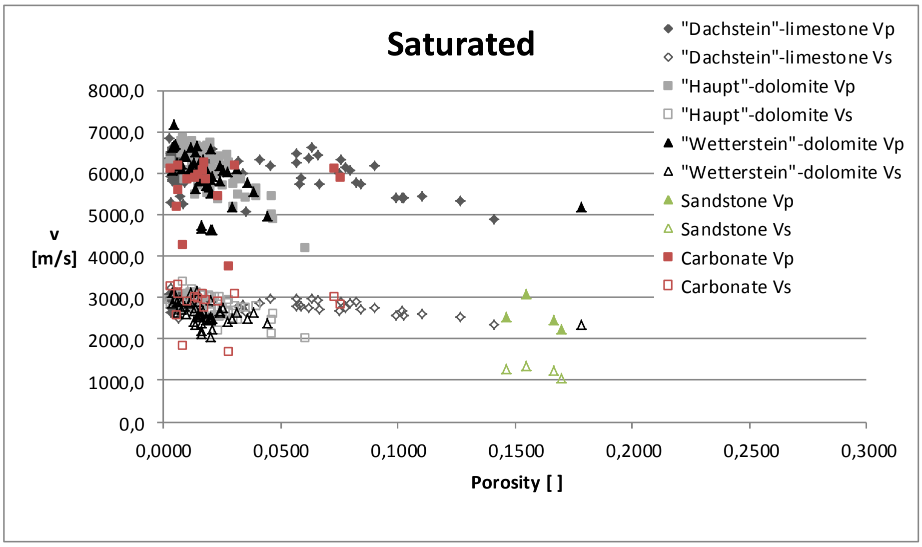

Figure 5.3. Compressional and shear wave velocities versus porosity for saturated samples.

Figure 5.4 shows the general trend of decreased shear wave velocities and increased P-wave velocities with saturation. This trend helps discriminate between dry and saturated rocks. This discrimination between dry and saturated samples can be seen also in the shear versus acoustic impedance cross-plot, where the same trend can be observed as before (decreased shear impedance and increased acoustic impedance with saturation (Figure 5.5).

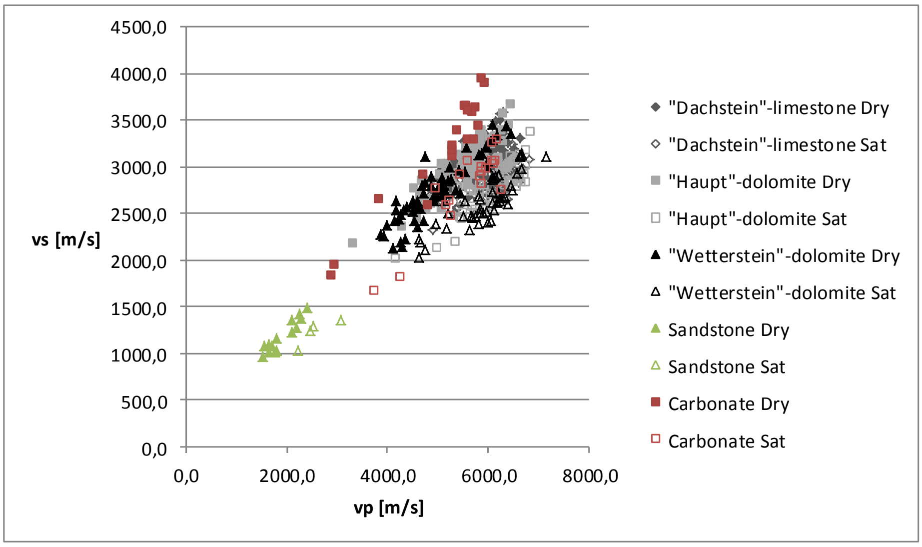

Figure 5.4. v_p versus v_s for dry and saturated samples.

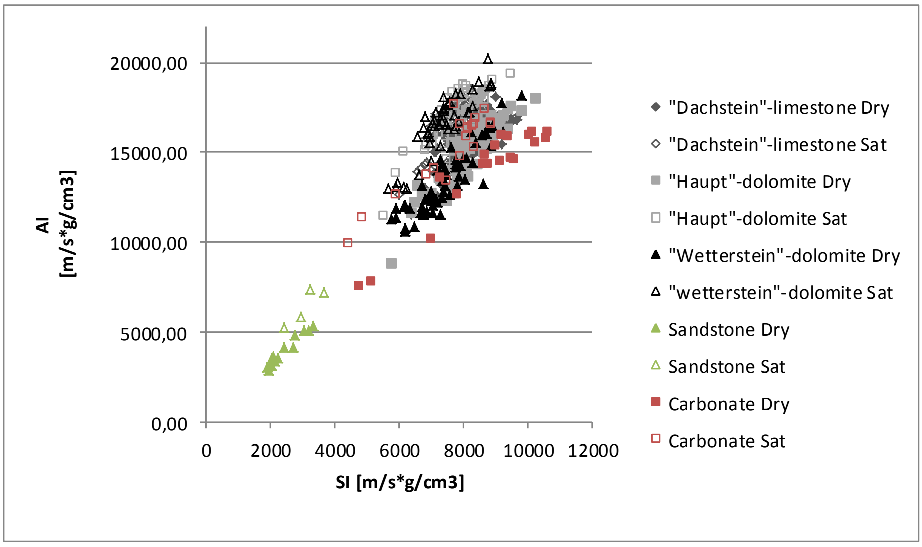

Figure 5.5. Shear and acoustic impedance for dry and saturated samples are displayed.

Using the measured density, compressional and shear wave velocities bulk (*k*) and shear modulus (μ) for the dry and saturated samples were calculated due to the following equations:

$$k = \rho(V_P^2 - 2V_S^2)$$

$$\mu = \rho V_S^2$$

Bulk modulus can be defined as ratio of hydrostatic stress to volumetric strain, additionally shear modulus is the ratio of shear stress to shear strain (Schön, 2011).

The fluid effect is evident as shown in Figure 5.6 and Figure 5.7. The fluid effect is large on the bulk modulus and small but significant on the shear modulus in case of carbonates. Similar observations have also been published by Eberli et al. (2003). These observations and the results of Rogen et al. (2005) indicate that Gassmann model, which assumes no fluid control of shear modulus, might not be appropriate for this group of carbonate rocks.

A plot of shear modulus under dry condition versus shear modulus under saturated conditions documents that the shear modulus decreases in carbonate samples with saturation. Shear weakening occur in our carbonate samples (Figure 5.6).

Gas-brine substitution causes an increase in bulk modulus in carbonates. The bulk modulus is dependent on the fluid (Figure 5.7).

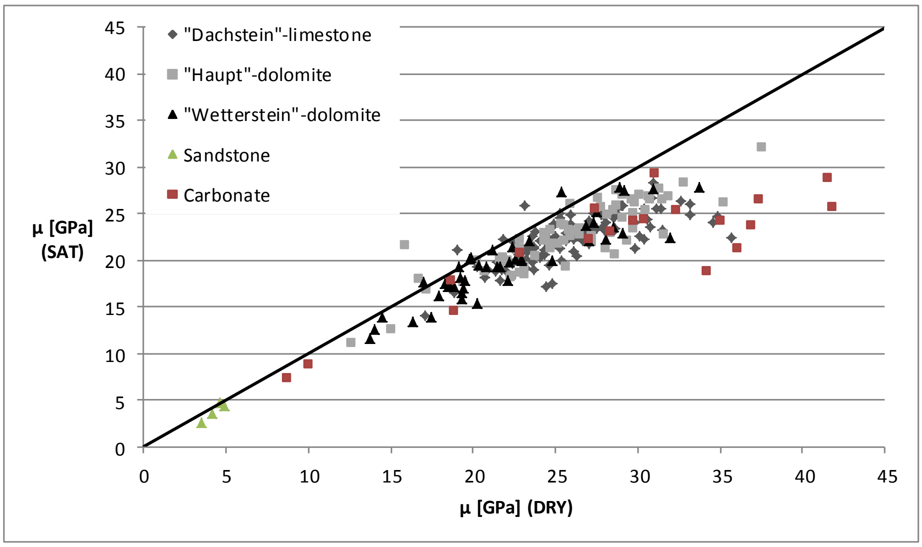

Figure 5.6. Changes of shear modulus with saturation are displayed.

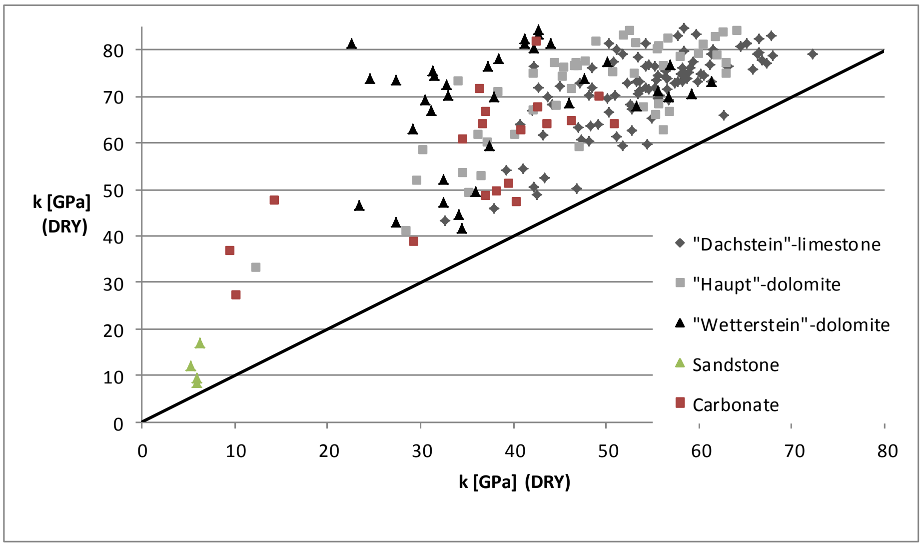

Figure 5.7. Changes of bulk modulus with saturation are displayed.

The Poisson’s ratio, that is defined as the ratio of lateral strain to axial strain in a uniaxial stress state, is controlled mainly by rock type and pore fluid (Schön, 2011). Figure 5.8 shows this trend, as the clastic and carbonate rocks can be discriminated clearly.

Moreover, the different pore fluid (gas and brine) demonstrates dissimilar character, as the gas-saturated samples have a lower Poisson’s ratio than the brine-saturated ones.

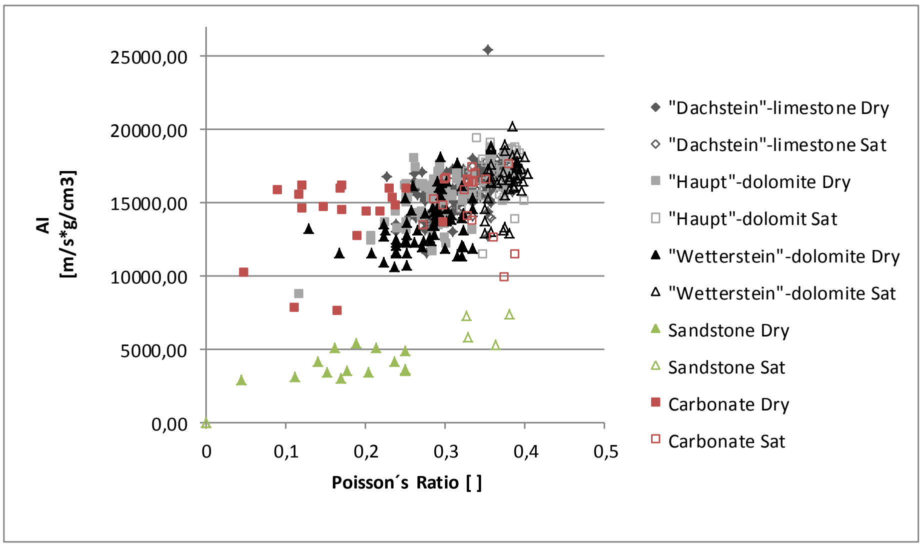

Figure 5.8. Poisson’s ratio and acoustic impedance for dry and saturated samples are displayed.

6. Model Calculation

The purpose of using models in rock physics is to idealize or simplify the rocks which are heterogeneous systems with internal structure in order to formulate elastic rock properties in terms of volume fractions and properties of the components, the rock texture, pressure, etc. (Schön, 2011).

According to the type of the geometrical idealization of the rock we can classify the models. For instance, bound models, sphere pack models, inclusion models and pore fluid effect models can be applied in regard to the difference simplification method of rock geometry.

In this study different models were carried out such as Hertz-Mindlin's theory (1949) and friable-sand model and constant-cement theory, Hashin-Shtrikman Bounds (1963) as a bound model, Kuster and Toksöz (1974) formulation as an inclusion model and Gassmann (1951) model for modeling of fluid effects.

6.1. The friable-sand model and constant-cement theory

Dvorkin and Nur (1996) introduced two theoretical models for high-porosity sands. The contact-cement model assumes that porosity reduces from the initial porosity of a sand pack due to the uniform deposition of cement layers on the surface of the grains. The contact cement dramatically increases the stiffness of the sand by strengthening the grain contacts.

The second theoretical model is the friable-sand model that assumes that porosity reduces from the initial sand-pack value due to the deposition of the solid matter away from the grain contacts. This non-contact additional solid material weakly affects the stiffness of the rock.

Avseth and Dvorkin (1999) introduced another, constant-cement, model which assumes that sand of varying porosity all have the same amount of contact cement. Porosity variation is alone due to non-contact pore-filling matter. Mathematically, this model is a combination of the two previously mentioned models (Avseth, 1999).

Before the constant-cement model was performed, the elastic moduli of the dry well-sorted end member at critical porosity were modeled as an elastic sphere pack subject to confining pressure (Avseth, 2005). These moduli are given by the Hertz-Mindlin theory (1949).

Hertz-Mindlin's theory is one of the elastic sphere pack model that assume that the grains are spheres of the same diameter and the centers of the spheres built a lattice system. It is mostly used for unconsolidated rocks to predict the compressional and shear behavior of the rocks under for instance reservoir pressure.

The dry rock bulk (k_{HM}) and shear moduli (μ_{HM}) can be calculated, if the porosity (ϕ), the effective pressure (i.e., the difference between the overburden pressure and the pore pressure (P), the shear modulus (μ) and Poisson's ratio (ν) of the solid phase and the coordination number (n) (the average number of contacts per grains) are known.

$$k_{HM} = \left[\frac{n^2(1-\phi_c)^2\mu^2}{18\pi^2(1-\nu)^2}P\right]^{1/3}$$

$$\mu_{HM} = \frac{5-4\nu}{5(2-\nu)}\left[\frac{3n^2(1-\phi_c)^2\mu^2}{2\pi^2(1-\nu)^2}P\right]^{1/3}$$

Effective pressure versus depth is obtained by the following formula:

$$P = g\int_0^z \left(\rho_b - \rho_{fl}\right)dz$$

Where g is the gravity constant, and ρ_b and ρ_{fl} are the bulk density and the fluid density, respectively, at a given depth, Z.

The coordination number, n, depends on porosity, as shown by Murphy (1982). The relationship between coordination number and porosity can be approximated by the following empirical equation:

$$n = 20 - 34\phi + 14\phi^2$$

At porosity ϕ the concentration of the pure solid phase (added to the sphere pack to decrease porosity) in the rock is $1 - \phi/\phi_c$ and that of the original sphere-pack is ϕ/ϕ_c. Then the bulk (K_{dry}) and shear (μ_{dry}) moduli of the dry friable sand mixture are:

$$K_{dry} = \left[\frac{\phi/\phi_c}{K_{HM} + 4\mu_{HM}/3} + \frac{1 - \phi/\phi_c}{K + 4\mu_{HM}/3}\right]^{-1} - \frac{4}{3}\mu_{HM}$$

$$\mu_{dry} = \left[\frac{\phi/\phi_c}{\mu_{HM} + z} + \frac{1 - \phi/\phi_c}{\mu + z}\right]^{-1} - z$$

where,

$$z = \frac{\mu_{HM}}{6}\left(\frac{9K_{HM} + 8\mu_{HM}}{K_{HM} + 2\mu_{HM}}\right)$$

The saturated elastic moduli, K_{sat} and μ_{sat}, can now be calculated from Gassmann's equations.

6.2. Hashin-Shtrikman Bounds

For prediction of elastic moduli of a rock (which is a mixture of grains and pores) it is needed to know the volume fractions of grains and pores, the elastic moduli of the phases and the relative arrangement of phases to each other. If only the volume fractions and the constituent moduli are specified, only the upper and the lower bounds can be predicted (Figure 6.1.).

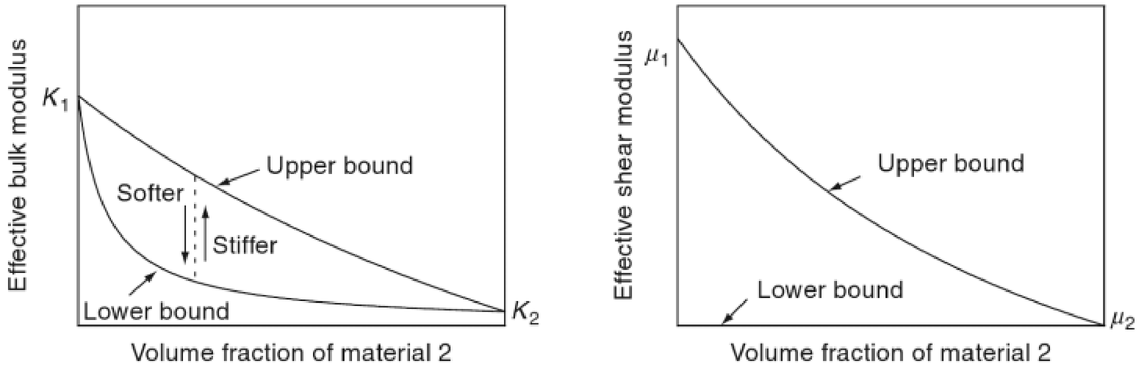

Figure 6.1. Schematic representation of the upper and lower bounds on the elastic bulk and shear moduli. (Mavko, 1998).

Hashin-Shtirkman bounds provide the narrowest possible range without specifying anything about the geometries of the components. The following equations present a comfortable calculation for a two-component medium (Mavko, 1998):

$$K^{HS\pm} = K_i + \frac{f_2}{(K_2 - K_1)^{-1} + f_1\left(K_1 + \frac{4}{3}\mu_1\right)^{-1}}$$

$$\mu^{HS\pm} = \mu_1 + \frac{f_2}{(\mu_2 - \mu_2)^{-1} + \frac{2f_1(K_1 + 2\mu_1)}{5\mu_1\left(K_1 + \frac{4}{3}\mu_1\right)}}$$

where

$K_1, K_2 =$ bulk moduli of individual phases

$\mu_1, \mu_2 =$ shear moduli of individual phases

$f_{1,}f_2 =$ volume fractions of individual phases

The upper bound is computed when the stiffest material is termed 1, and the lower bound can be calculated when the softest material is termed 1. For porous rock the solid matrix is termed 1 and fluid, that fills the pores, is the component 2. In this case the lower bound of shear moduli is equal to 0. Due to the Hashin-Shtrikman lower bound describes exactly the moduli of a suspension of grains in a pore fluid where there is no shear resistance and no shear wave (Schön, 2011).

6.3. Inclusion Model, Kuster and Toksöz

Inclusion models are mostly used in case of hard rocks with low porosity. Pores, vugs, or cracks are modeled as ellipsoidal inclusion in a solid host material (Schön, 2011). Furthermore, with increasing porosity more ellipsoidal inclusions can be added to the host media. The aspect ratio (α) characterizes the shape of inclusions (Figure 6.2).

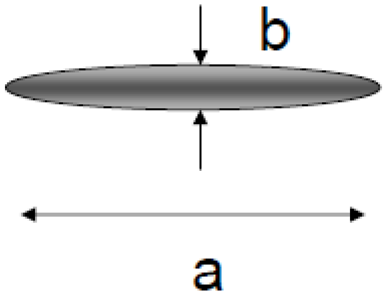

Figure 6.2. Definition of aspect ratio α=b/a.

Kuster and Toksöz (1974) developed a theory based on long-wavelength first-order scattering theory to express P- and S wave velocities of an isotropic material which contains randomly oriented spherical or spheroidal inclusions. According to their theory effective moduli k_{KT} and μ_{KT} can be calculated:

$$\frac{k_{KT} - k_S}{k_{KT} + \frac{4}{3}\mu_S} = \frac{\sum_{i=1}^{n} \phi_i (k_i - k_S) P^{si}}{k_S + \frac{4}{3}\mu_S}$$

$$\frac{\mu_{KT} - \mu_S}{\mu_{KT} + \varsigma_S} = \frac{\sum_{i=1}^{n} \phi_i (\mu_i - \mu_S) Q^{si}}{\mu_S + \varsigma_S}$$

where

$$\varsigma_S = \frac{\mu_S}{6} \frac{9k_S + 8\mu_S}{k_S + 2\mu_S}$$

where

ϕ_i is the volume fraction related to inclusion material *i*

k_i, μ_i are moduli of inclusion material *i*

k_S, μ_S are moduli of the solid host material (background)

The coefficients P^{si}, Q^{si} are related to the shape of the inclusions and describe the effect on an inclusion of material in a background medium. The following table represents the applied equations to calculate P^{si}, Q^{si} parameters for different shape of inclusions with random distribution (Table 6.1):

Table 6.1: Coefficients P and Q for some specific shapes. The subscripts m and i refer to the background and inclusion materials (Berryman, 1995, Mavko, 1998).

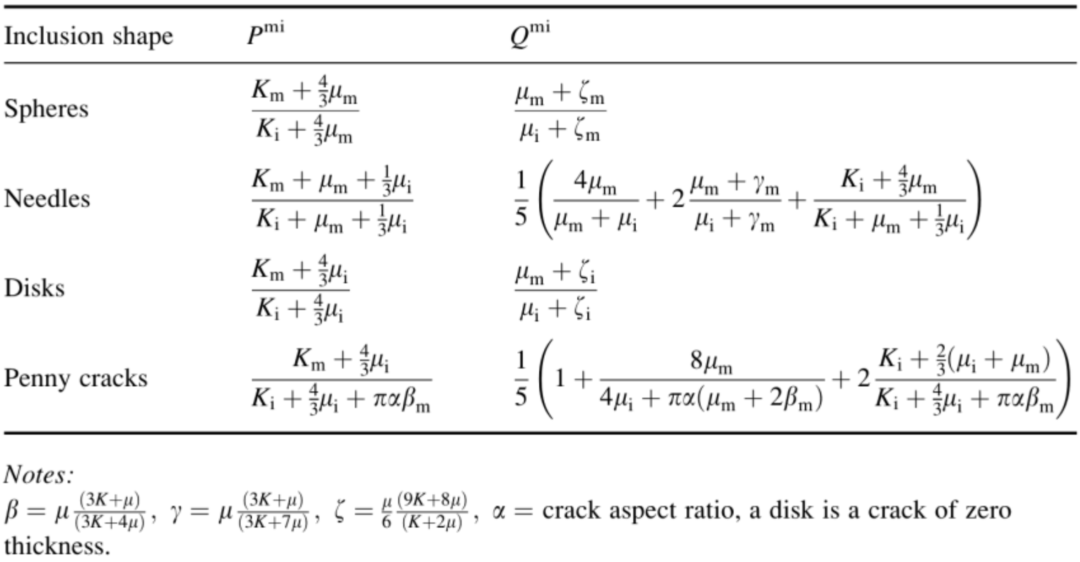

Inclusion shape	P^{mi}	Q^{mi}
Spheres	$\frac{K_m + \frac{4}{3}\mu_m}{K_i + \frac{4}{3}\mu_m}$	$\frac{\mu_m + \zeta_m}{\mu_i + \zeta_m}$
Needles	$\frac{K_m + \mu_m + \frac{1}{3}\mu_i}{K_i + \mu_m + \frac{1}{3}\mu_i}$	$\frac{1}{5}\left(\frac{4\mu_m}{\mu_m + \mu_i} + 2\frac{\mu_m + \gamma_m}{\mu_i + \gamma_m} + \frac{K_i + \frac{4}{3}\mu_m}{K_i + \mu_m + \frac{1}{3}\mu_i}\right)$
Disks	$\frac{K_m + \frac{4}{3}\mu_i}{K_i + \frac{4}{3}\mu_i}$	$\frac{\mu_m + \zeta_i}{\mu_i + \zeta_i}$
Penny cracks	$\frac{K_m + \frac{4}{3}\mu_i}{K_i + \frac{4}{3}\mu_i + \pi\alpha\beta_m}$	$\frac{1}{5}\left(1 + \frac{8\mu_m}{4\mu_i + \pi\alpha(\mu_m + 2\beta_m)} + 2\frac{K_i + \frac{2}{3}(\mu_i + \mu_m)}{K_i + \frac{4}{3}\mu_i + \pi\alpha\beta_m}\right)$

Notes:
$\beta = \mu\frac{(3K+\mu)}{(3K+4\mu)}$, $\gamma = \mu\frac{(3K+\mu)}{(3K+7\mu)}$, $\zeta = \frac{\mu}{6}\frac{(9K+8\mu)}{(K+2\mu)}$, α = crack aspect ratio, a disk is a crack of zero thickness.

For a simple case when one inclusion type with volume fraction and a fluid inclusion filling are assumed, the moduli of the rock can be expressed, as:

$$k_{KT} = \left(k_S + \phi \frac{\frac{4}{3}\mu_s\left(k_{fl} - k_s\right)}{k_s + \frac{4}{3}\mu_s} P^{si} \right) \left(1 - \phi \frac{\left(k_{fl} - k_s\right)}{k_s + \frac{4}{3}\mu_s} P^{si} \right)^{-1}$$

$$\mu_{KT} = \mu_s \left(1 - \phi Q^{si} \frac{\varsigma_s}{\mu_s + \varsigma_s} \right) \left(1 + \phi Q^{si} \frac{\mu_s}{\mu_s + \varsigma_s} \right)^{-1}$$

For the simplest case the inclusions are spherical and P^{si}, Q^{si} parameters can be determined by using the equations that are given in Table 1 (Schön, 2011).

Applying this model calculation it is possible to receive a better understanding about the texture of samples that is connected with the aspect ratio.

Using this model we have to realize that the Kuster-Toksöz formulations have some assumption and limitation. For instance, the media is isotropic, linear and elastic. Furthermore, there is no fluid flow between the pores or fractures. They are limited to dilute concentrations of the inclusions, and the ellipsoidal inclusion shapes are assumed idealized (Mavko, 1998).

6.4. Gassmann Model- Modelling of Fluid Effects

The fluid substitution problem, that describes the prediction of seismic velocities in saturated and dry rock, is one of the most important questions in the rock physics analysis. The Gassmann model (Gassmann, 1951) provides a solution that estimates the elastic properties of a porous medium at one fluid state, and predicts the elastic properties for another fluid state (Schön, 2011).

Some assumptions and limitations of Gassmann’s theory should be kept in mind if it is applied:

- The rock is macroscopically homogeneous and isotropic. Although, the Gassmann’s equation is free of assumption about the pore geometry.
- The pore pressures are equilibrated throughout the pore space, thus the low seismic frequency provides the best results by using the Gassmann’s equation.
- Non viscous and frictionless fluids fill completely the pores. Therefore, the rock-fluid system is closed, so there is no fluid flow within the pores. In addition, the pore fluid does not interact with the solid material or rock frame.

Due to the changing in pore fluid, the elastic moduli and density of rock also change. Hence, the velocities of elastic waves are influenced by pore fluid. The density change can be described by the following equation:

$$\rho = (1-\phi)\rho_s + \phi\rho_{fl}$$

The pore fluid does not affect the shear modulus of the rock. However, the compressional bulk modulus is strongly dependent on fluid compressional modulus (Schön, 2011).

Using the Gassmann’s equation bulk modulus for saturated rock can be calculated, that result is greater than for the dry rock:

$$k_{sat} = k_{dry} + \frac{\left(1-\frac{k_{dry}}{k_s}\right)^2}{\frac{\phi}{k_{fl}} + \frac{1-\phi}{k_s} - \frac{k_{dry}}{k_s^2}}$$

$$\frac{k_{sat}}{k_s - k_{sat}} = \frac{k_{dry}}{k_s - k_{dry}} + \frac{k_{fl}}{\phi\left(k_s - k_{fl}\right)}$$

$$\mu_{sat} = \mu_{dry}$$

where

k_{sat} is the effective bulk modulus of the rock with pore fluid

k_{dry} is the effective bulk modulus of the drained or dry rock

k_s is the bulk modulus of the solid rock component

k_{fl} is the bulk modulus of the pore fluid

ϕ is the porosity (Schön, 2011).

Applying the calculated bulk and shear modulus and the density the velocities can be defined:

$$V_P = \sqrt{\frac{k + \frac{4}{3}\mu}{\rho}} = \sqrt{\frac{\frac{k_{dry} + \left(1 - \frac{k_{dry}}{k_s}\right)^2}{\frac{\phi}{k_{fl}} + \frac{1-\phi}{k_s} - \frac{k_{dry}}{k_s^2}} + \frac{4}{3}\mu_{dry}}{(1-\phi)\rho_s + \phi\rho_{fl}}}$$

$$V_S = \sqrt{\frac{\mu}{\rho}} = \sqrt{\frac{\mu_{dry}}{(1-\phi)\rho_s + \phi\rho_{fl}}}$$

7. Results of Model Calculation

In this chapter I am going to present the results of the model calculations, such as Hertz-Mindlin theory, Hashin-Shtrikman bounds, Kuster and Toksöz inclusion model calculations and Gassmann theory, which were performed using our sandstone and carbonate samples.

7.1. Modelling elastic properties in sandstone samples

Our aim was, by applying the different model calculation in sandstone samples, to be able to compare the laboratory results with the borehole data. The Hertz-Mindlin contact theory was used to present the alteration of the rock elastic properties due to the changing in the effective pressure. It can be observed that the bulk moduli of the sandstone samples become higher due to the effective pressure, which was computed by applying the information of the measured depth of the cores (Figure 7.1).

Afterward, Gassmann fluid substitution was carried out to determine the bulk moduli of the water saturated samples (Figure 7.1). Substitution of gas with water causes increasing bulk moduli of the samples, because the water is less compressible than gas.

Furthermore, Hashin-Shtrikman upper and lower bounds were calculated to determine the upper and lower limits of elastic parameters of the composite medium (Figure 7.1). The input parameters of model calculations were determined according to the mineral constitutions moduli of our samples that were defined in the literature (Table 7.1).

Table 7.1. Mineral composition of sandstone samples due to the literature (OMV, Core documentation, Sedimentological and Petrographical analyses).

	Quartz	Feldspar	Limestone	Dolomite	Illite	Calcite Cement	Quartz Cement
1A	0,48	0,07	0,04	0,29	0,03	0,02	0,01
1C	0,49	0,05	0,07	0,18	0,04	0,03	0,01
1F	0,69	0,10		0,10	0,08	0,04	0,04
1G	Grey, heavily bioturbated, partly shaly, fine-grained calcareous sandstone, isolated occurrence of carboneized plant debris.						

Using the elastic properties of the minerals, the input parameters of the model calculations were predicted that are summarized in the following table (Table 7.2):

Table 7.2. Input parameters for calculation of Hashin-Shtrikman bounds.

	K [GPa]	μ [GPa]	ρ[g/cm^3]
Mineral	44,63	38,97	2,69
Water	2,56	0,021	0,10

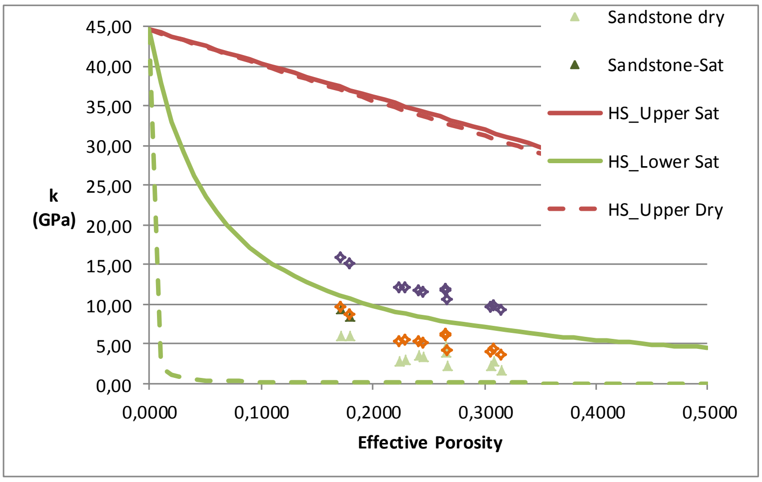

Figure 7.1. Displayed is bulk modulus versus effective porosity for dry sandstone samples. Additionally, Hashin-Shtrikman bounds and the result of the calculation of Hertz-Mindlin and Gassmann theory are displayed.

Cross plots were also used to represent the bulk modulus versus effective porosity values of borehole data. The applied well logs were measured in the same well than the sandstone cores are coming from. Hashin-Shtrikman lower and upper bounds were computed by using the same input parameters than by the laboratory results. Therefore, the comparison of the laboratory and the borehole data was possible. It can become clearly visible in both cases (Figure 7.1 and Figure 7.2) that the water saturated points lie above the lower bound, and the gas saturated points are located near or below the line. The Hashin-Shtrikman bounds characterized our data set with these input parameters well.

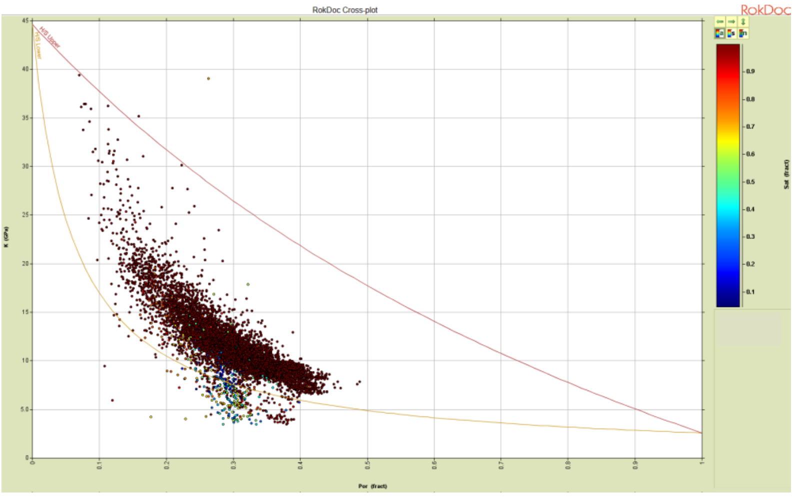

Figure 7.2. Displayed is bulk modulus versus effective porosity for borehole data that is colour coded by water saturatuion. Hashin-Shtrikman lower and upper bounds (saturated) are also represented.

7.2. Modelling elastic properties in carbonate samples

Different model calculations were performed also in carbonate samples. However, the carbonate rocks have a more complex pore system than the clastics, which means that development of a carbonate rock physics model is extremely difficult. Pore shape appears to be the dominant factor in carbonate rock physics. Whereas clastic rocks have granular structure based on individual particles/grains the carbonates frequently are more a homogeneous solid block with pores. Therefore, inclusion model was computed to predict the dominant pore shape of the samples.

7.2.1. Results of Hashin-Shtrikman bounds

Hashin-Shtrikman (1962) upper and lower bounds were calculated for our carbonate samples. Only the upper and the lower bounds of the elastic moduli can be predicted, if only the volume fractions and the constituents' moduli are defined.

Figure 7.3 and 7.4 show the calculated bulk modulus from measured velocity values versus effective porosity with the calculated Hashin-Shtrikman bounds. The input data of the model calculation were the values of the solid matrix that is characterizes by k_s= 95 GPa and μ_s= 34 GPa.

The used bounds are the upper one and additionally calculated lines with 75% and 50% of the upper bound. It becomes visible that the calculated model lines can display the correlation for the saturated samples. The 75% line shows good results for the "Haupt"-dolomite and the "Dachstein"-limestone, the 50% bound for the "Wetterstein"-dolomite. The "Carbonate" samples can be characterised by the 50% line and the lower bound. In contrast to the dry samples can be described but not as good as for the saturated samples. This is originated by the extreme low compressional modulus of the air, which controls the low bound. The upper bound describes the "Haupt"-dolomite and the 75% bound displays the correlation for the "Dachstein"-limestone and a part of the "Wetterstein"-dolomite. Our "Carbonate" samples lie again around the 50% line and the lower bound.

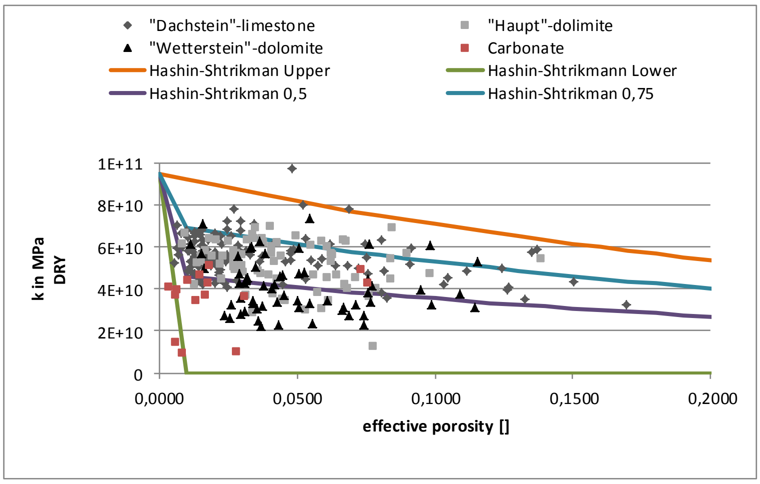

Figure 7.3. Displayed is bulk modulus for dry samples versus (effective) porosity, additionally displayed are the calculated lines from Hashin-Shtrikman (1963), (upper bound, lower bound, 0.5 upper bound and 0.75 upper bound).

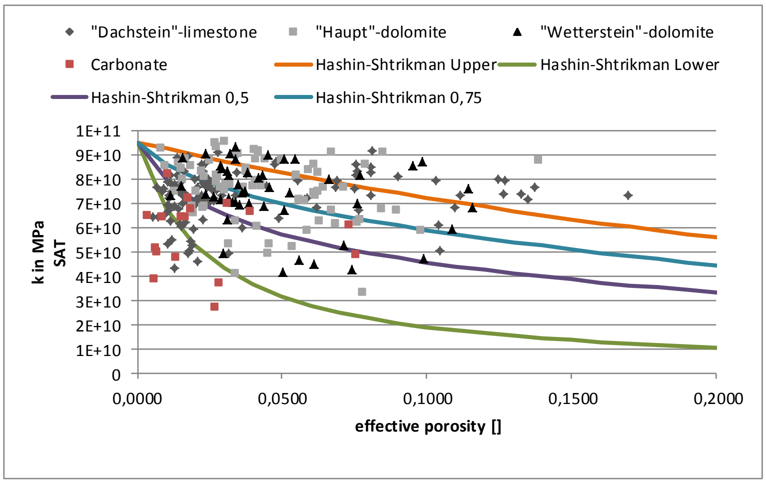

Figure 7.4. Displayed is bulk modulus for saturated samples versus (effective) porosity, additionally displayed are the calculated lines from Hashin-Shtrikman (1963), (upper bound, lower bound, 0.5 upper bound and 0.75 upper bound).

Bulk modulus versus effective porosity values of borehole data was also plotted. The displayed well contains dolomite layer. Hashin-Shtrikman lower and upper bounds were computed by using the same input parameters than by the laboratory results. Therefore, the comparison of the laboratory and the borehole data was possible. According to the well log data it is known that the chosen well contains mainly dolomite whose pores are mainly filled with gas in the investigated zone. It can become clearly visible in both cases (Figure 7.3 and Figure 7.5) that the chosen input parameters describe our data set well in both scales. In both cases our data points lie between the upper and lower Hashin-Shtrikman bounds.

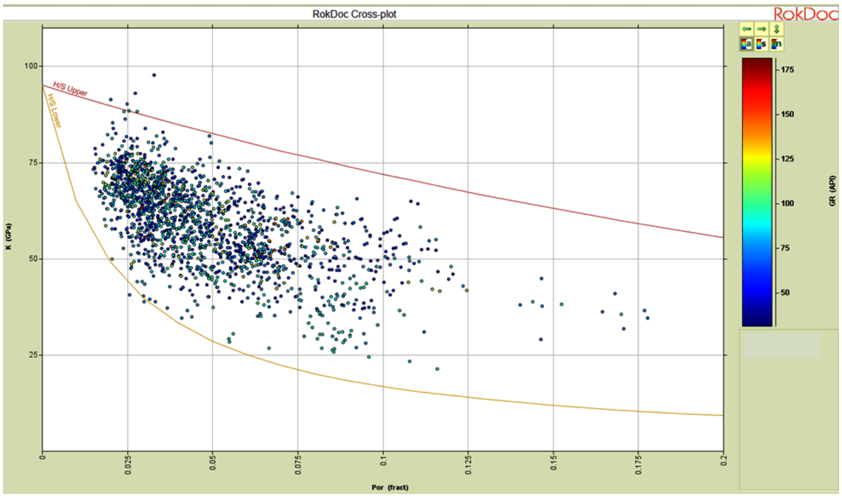

Figure 7.5. Displayed is bulk modulus versus effective porosity for borehole data that is colour coded by Water-Saturation. Hashin-Shtrikman lower and upper bounds are also represented.

7.2.2. Results of the Kuster and Toksöz theory

Kuster and Toksoz (1974) used in their calculations a long-wavelength first order scattering theory with an inclusions model. The inclusions implemented are isolated with respect to the flow suitable for ultrasonic laboratory measurements. The model is limited to low porosity, which would be a perfect assumption for our samples with low porosity and low permeability.

Different equations are available for spheres, needles, discs or penny shaped cracks. Penny shaped cracks with different aspect ratios (0.005-0.5) were used. Values for the solid matrix are k_s= 95 GPa and μ_s= 34 GPa. Grain density was taken from the measurements from the heliumpycnometer, where the mean value of the data is ρ_s=2.77 g/cm^3. This value indicates that the dolomite contains also some calcite. For the comparison with our measured data, spherical inclusions, needles and penny-shaped cracks were first tested. Results showed that the spherical inclusions and needles cannot describe our data, so penny-shaped cracks with different aspect ratios (0.005-0.05) were used for the optimal description.

The next step was to describe the data with the Kuster-Toksöz model. Same input values were also used for the calculation of the upper and lower Hashin- Shtrikman bounds.

Figure 7.6 and 7.7 show the results for Kuster-Toksöz for different aspect ratios: 0.2; 0.1; 0.05; 0.025; 0.01; 0.005, where compressional and shear wave velocity (dry samples) were plotted versus the porosity from the effective helium porosity. An aspect ratio of 0.025 for the v_p can describe for one group of the "Dachstein"-limestone. The second group needs an aspect ratio of 0.2. Therefore the assumption can be made, that the groups differ in their pore geometry. "Wetterstein"-dolomite scatter, but most data are between α=0.0025 and 0.005. The v_s data need a little bit lower aspect ratios for their description, which means that the group of "Dachstein"-limestone now is between an aspect ratio of 0.01 and 0.025 and the upper group is described with an aspect ratio of 0.1.

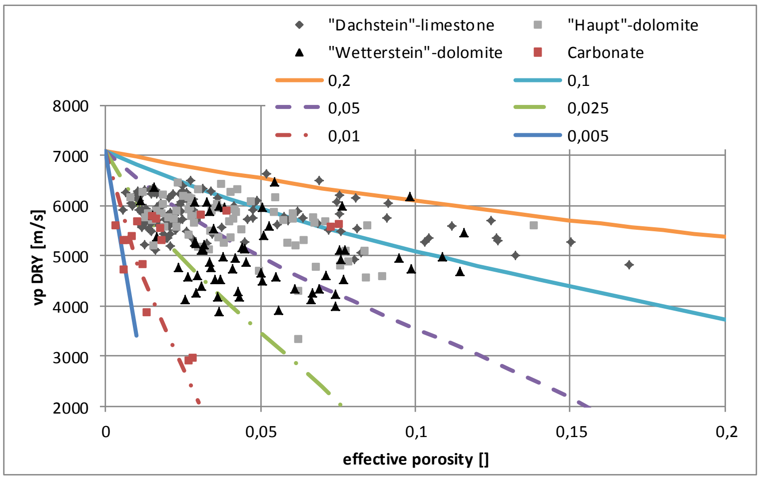

Figure 7.6. Displayed is v_p for dry samples versus (effective) porosity, additionally displayed are the calculated lines from Kuster and Toksöz (1974), for different aspect ratios (0.2, 0.1, 0.05, 0.025, 0.01, 0.005).

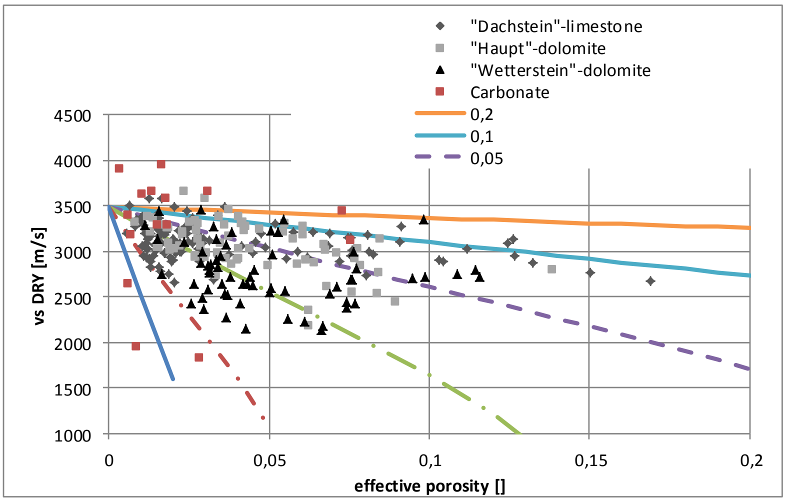

Figure 7.7. Displayed is v_s for dry samples versus (effective) porosity, additionally displayed are the calculated lines from Kuster and Toksöz (1974), for different aspect ratios (0.2, 0.1, 0.05, 0.025, 0.01, 0.005).

Figure 7.8 and 7.9 shows the data for the saturated samples with the calculated lines with the Kuster and Toksöz model. Again the different aspect ratios are used. Compressional wave velocity can be explained with the same aspect ratios like before. Shear wave velocity is lower than before and therefore also needs again a little bit lower aspect ratios. This could be a result from the discussed shear “weakening” (Page 2).

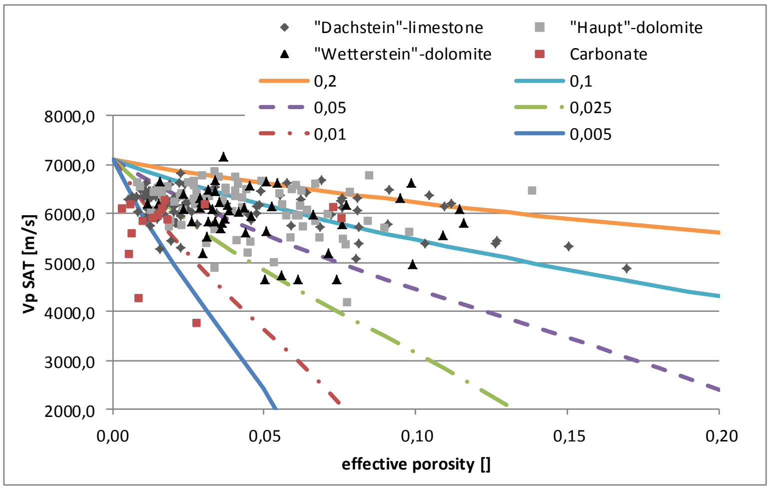

Figure 7.8. Displayed is v_p for saturated samples versus (effective) porosity, additionally displayed are the calculated lines from Kuster and Toksöz (1974), for different aspect ratios (0.2, 0.1, 0.05, 0.025, 0.01, 0.005).

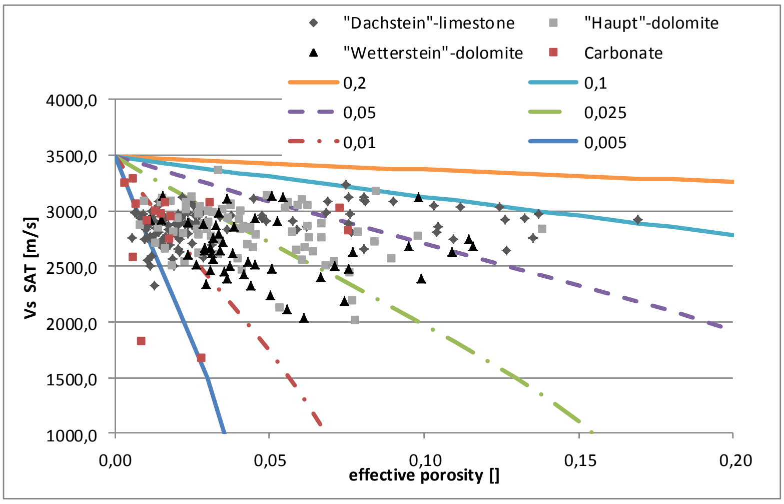

Figure 7.9. Displayed is v_s for saturated samples versus (effective) porosity, additionally displayed are the calculated lines from Kuster and Toksöz (1974), for different aspect ratios (0.2, 0.1, 0.05, 0.025, 0.01, 0.005).

The borehole data is also displayed in a cross plot of compressional velocity versus porosity (Figure 7.10). Furthermore, Kuster and Toksöz inclusion model calculation was performed using the same input and aspect ratio parameters as previously by laboratory results. It is visible that the borehole data can be described by lower aspect ratio than laboratory results. However, our core data (Carbonate) represent a good correlation with the borehole data.

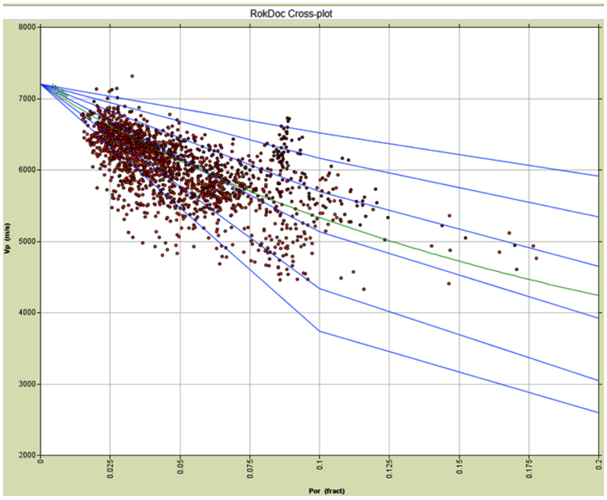

Figure 7.10. Displayed is compressional velocity versus effective porosity for borehole data, additionally displayed are the calculated lines from Kuster and Toksöz (1974), for different aspect ratios (0.2, 0.1, 0.05, 0.025, 0.01, 0.005) (blue lines) and the Time-average equation (green).

7.2.3. Results of the Gassmann theory

Gassmann theory (1951) is based on the fact that rocks become more resistant to compression if their pore space is filled with a fluid that is less compressible than gas. Due to the theory, bulk modulus change can be computed. One important assumption of the Gassmann calculation is that the fluid does not alter the rock frame properties, with the exception of the additional stiffening of the rock frame by the fluid. Under this assumption the shear modulus should not change during saturation (Baechle, 2005).

Figure 7.11 shows the calculated bulk modulus based on the laboratory measurements and the Gassmann equation. It can be observed that bulk modulus from the Gassmann calculation give mostly lower results than the values that was computed from the measured compressional and shear wave velocity.

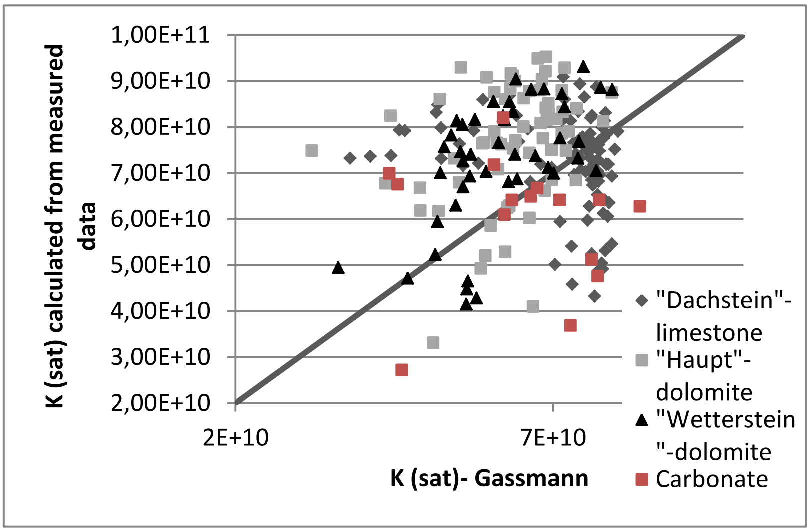

Figure 7.11. Displayed is the calculated bulk modulus based on the laboratory measurements and using the Gassmann equation.

Gassmann-predicted compressional and shear velocity can be calculated. If the shear modulus of the rocks changes during saturation, the calculated Gassmann velocities will either over- or underpredict the measured saturated velocities. Our experiments with ultrasonic frequencies show that the shear modulus indeed changes with saturation and consequently the Gassmann-predicted velocities may also be inaccurate under low-frequency conditions. Figure 7.12 displays the differences between the measured and Gassmann-predicted compressional and shear wave velocities. It can be seen that the predicted v_p values either under- or overestimate the measured saturated velocities. In case of shear wave velocity the calculated results are overestimate the measured ones. The reason of this inaccurate result is that the model ignores the fact that the shear modulus changes during saturation.

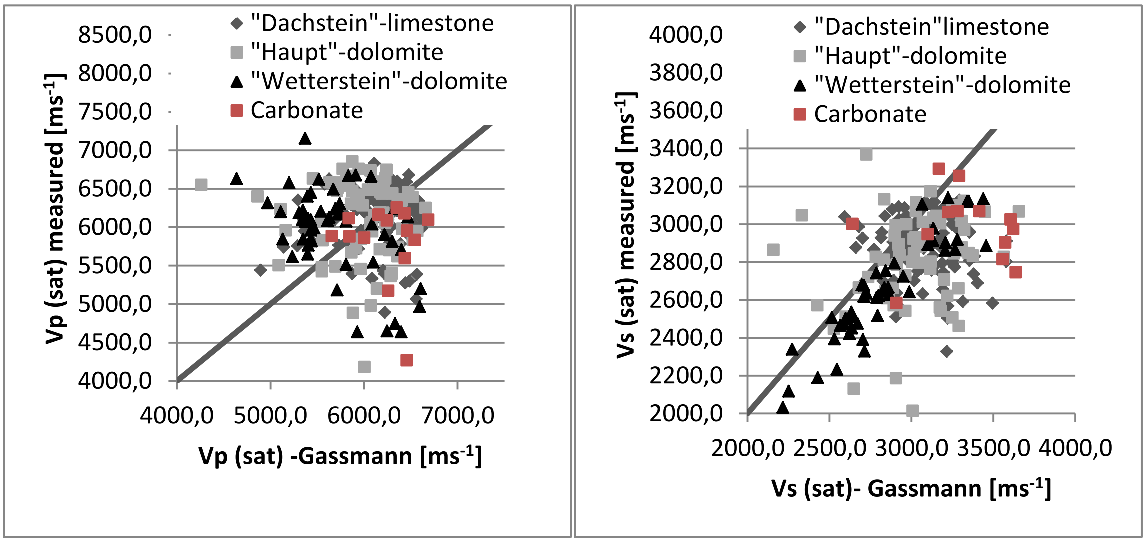

Figure 7.12. Measured compressional (left) and shear (right) velocity versus calculated compressional and shear velocity using the Gassmann equations.

Figure 7.13 shows the change in shear modulus versus difference between Gassmann-predicted and measured saturated velocity. Gassmann-derived velocities both over- and underestimate saturated velocities in carbonates by as much 500 and 600 m/s, respectively. In our dataset shear weakening occur during saturation. Rock-fluid interactions are assumed to cause the shear modulus change in the saturated rock by alteration of the rock frame properties. The assumption of constant shear modulus in Gassmann's theory seems not to be valid for our carbonate samples.

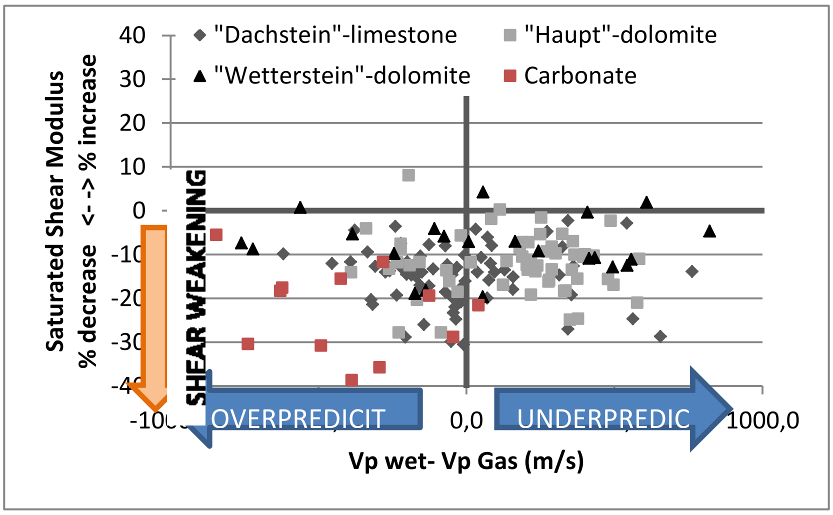

Figure 7.13. Display of changing shear moduli and its effect on velocity prediction of saturated rocks using Gassmann´s equation.

8. Formation Evaluation

The general goal of log measurements is to define the lithologic profile along the well and the exact depth of the formation and rock boundaries. Furthermore, the general tasks of formation evaluation are the detection and characterization of the potential reservoir zones, and to determine their porosity, fluid saturation and permeability.

8.1. Formation evaluation using well logs

In this study, gamma ray logs were applied to separate the “clean sections” from the shaly section, due to the assumption that shale and clay are the only radioactive components in rocks and there are no other radioactive minerals present.

To characterize the assumed reservoir zones, neutron-log (that is calibrated for limestone matrix and pore fluid fresh water), density-log and resistivity-logs (micro and deep resistivity) were used. Neutron-log and density-log were displayed in the same trace, and are plotted from right to left increasing neutron porosity (limestone calibrated) and decreasing density. The reason behind this display is to be able to detect gas easier. Gas reservoirs show lower neutron porosity and also a lower density, which means the two logs cross each other if we use the earlier mentioned scale (Figure 8.1).

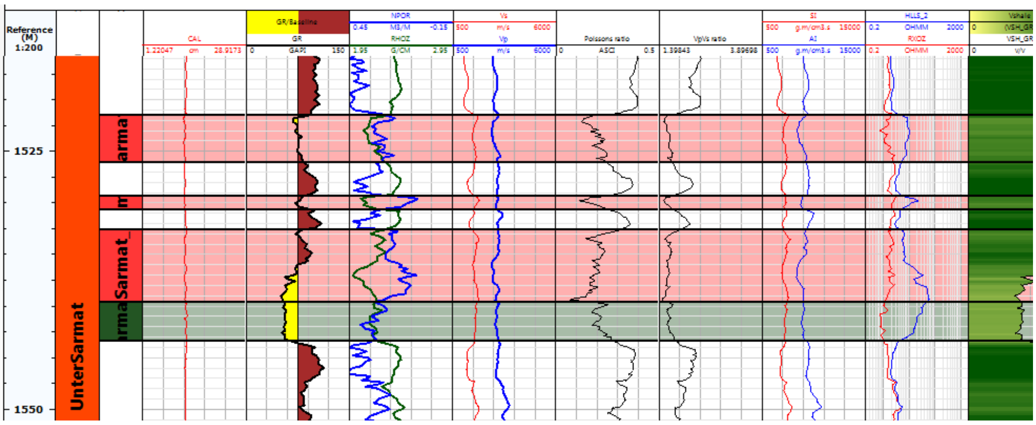

Figure 8.1. Gas reservoirs detection using neutron, density and resistivity logs.

To receive information about the pore fluid, micro and deep resistivity logs were investigated. The micro resistivity log provides observation about the resistivity of invaded zone, whereas the deep resistivity log presents the resistivity of the formation. In case of water, micro and deep resistivity logs show low and similar values. If the pores are filled with gas or oil, the deep resistivity log represents higher values, but the micro resistivity log stays still low. That is the reason why we are able to discriminate the oil bearing and water saturated reservoirs (Figure 8.2).

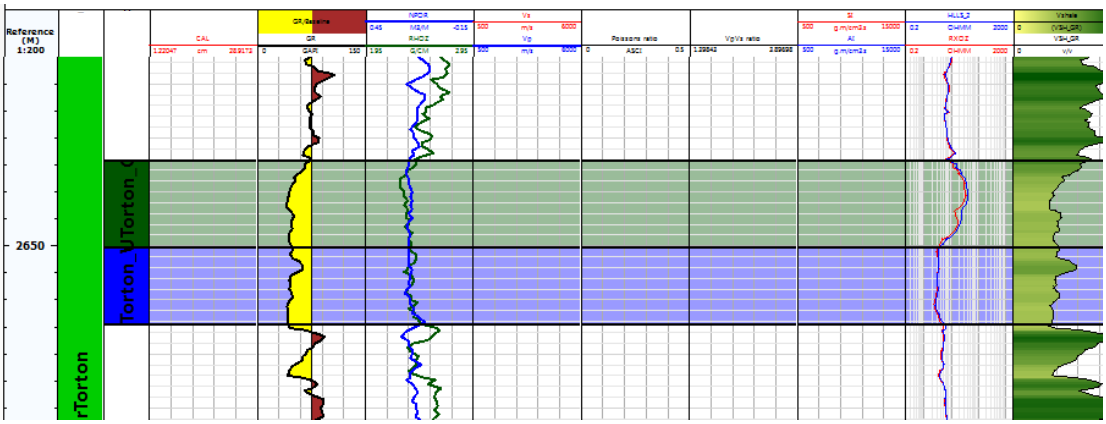

Figure 8.2. Separation of oil bearing and water saturated reservoirs using well logs.

8.2. Formation Evaluation using Cross-plots

Density-neutron-plot is used mostly to present the variation of two of the "porosity-sensitive" properties. Moreover, three linear equations were defined for limestone, dolomite and sandstone which are also imaged as a line in the cross-plot. The individual plots are designed for specific tools and different fluid properties (water). Additionally plots allow an estimation of lithology and the determination of a consistent porosity.

In case of shaly sands the shale content shifts the points from the sand line towards the dolomite line. Gas bearing zones shift the points towards low neutron porosity (Figure 8.3.).

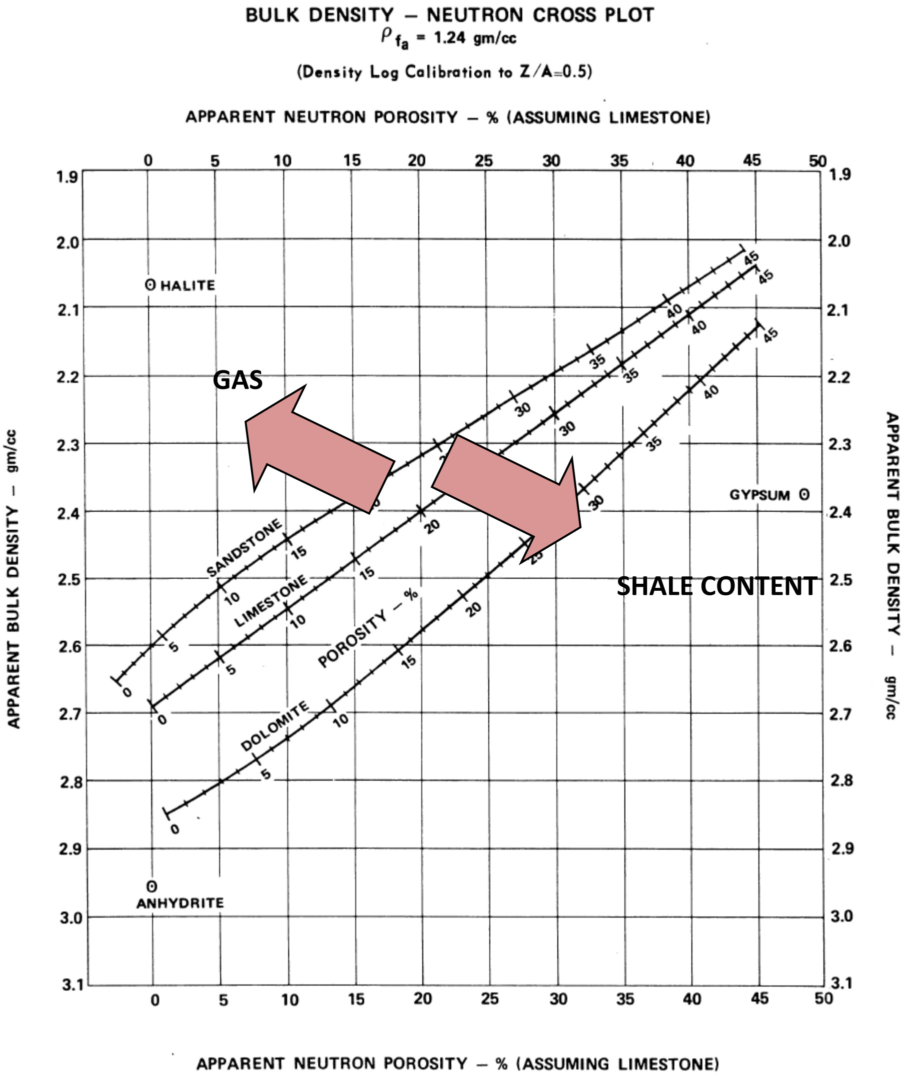

Figure 8.3. Bulk density versus neutron cross plot, additionally displayed are the lithology lines and the impact of gas and shale content.

The bulk density and neutron plot was also applied in our dataset to achieve a better understanding about the distribution of the lithology and the pore fluid in the studied area.

Figure 8.4 represents our “Haupt”-dolomite formation that lies exactly on the dolomite-line, which affords a good correlation between our dataset and the lithology lines. Furthermore, it can be seen that the different formations can be distinguished from each other clearly.

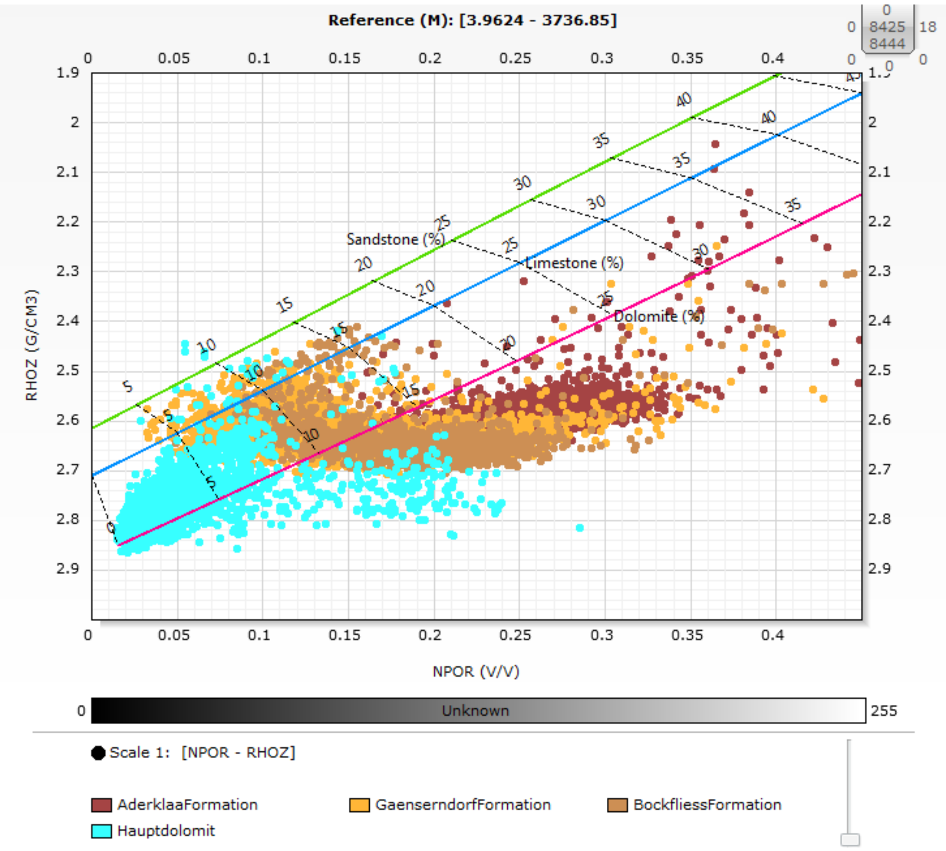

Figure 8.4. Bulk density log versus neutron log, additionally displayed are different formations which represents well the lithology lines.

Figure 8.5 shows our data points that are colour coded using the gamma Ray log. It can be observed that the increasing shale content influences the location of the data point. With increasing shale content (with higher Gamma Ray values), the points are shifted from the sand line towards the dolomite line.

Figure 8.6 Illustrates our interpretation of the pore fluid, that demonstrates moreover that the gas saturated points are shifted to the left corner of the cross plot. In addition, the water saturated sandstone points do not lie exactly on the sandstone line, which means that these sandstone reservoirs contain not only quartz minerals. According to the literature, it is known that these sandstones also contain more or less 20% dolomite that could be the reason of this shifting of the data points towards to dolomite.

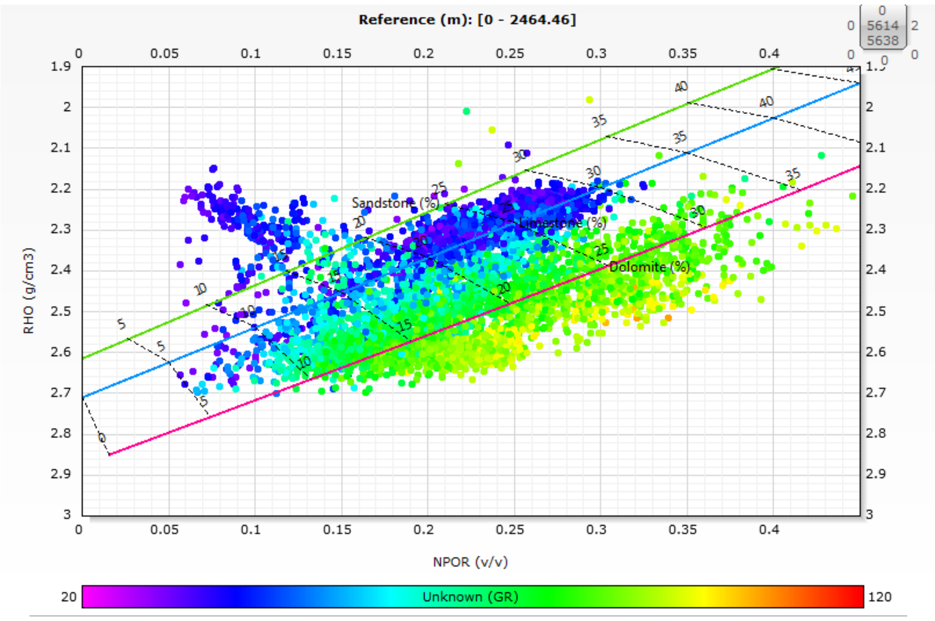

Figure 8.5. Density-neutron plot, the data points are colour coded using the Gamma Ray log.

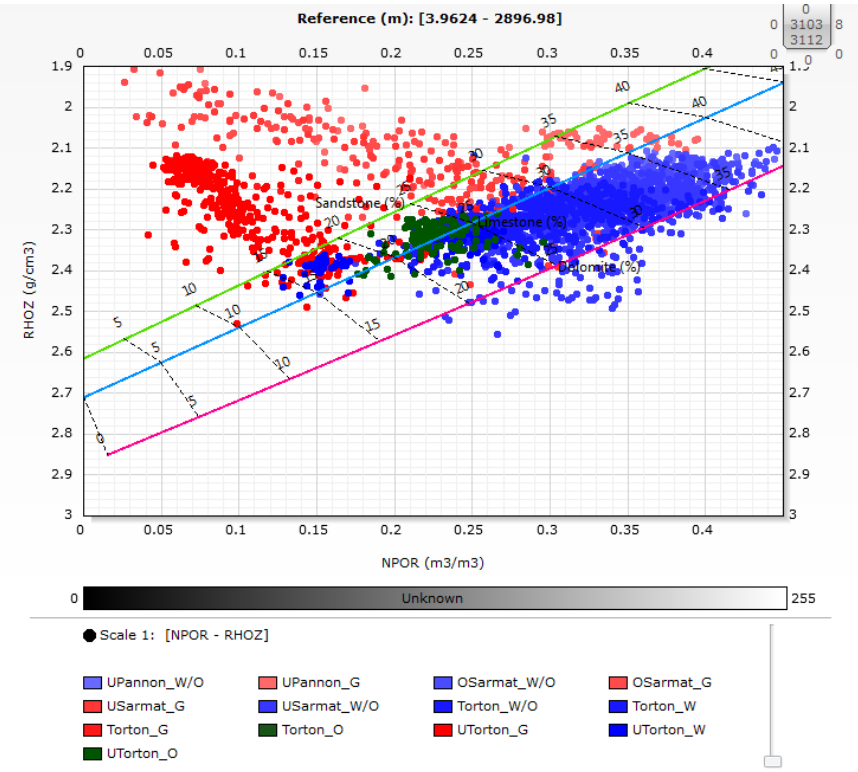

Figure 8.6. Density-neutron plot, displayed is the interpretation of the pore fluids.

9. Seismic inversion and its application in reservoir characterization

Seismic inversion is a successful tool to estimate the elastic properties from seismic data with wide vertical resolution. Seismic inversion is a complex process of inverting the seismic data into elastic properties of the reservoir. The aim of this technique is to make quantitative interferences about the elastic properties of the Earth's subsurface from remote observations (Nair, 2012).

Prediction of elastic properties, acoustic impedance, the ratio P to S velocity and density from seismic and well data is an inverse problem. The spiked response -at geological boundaries is transformed into layer properties such as acoustic impedance that may be used in the characterization of the reservoir. If all works well there is relation between the elastic properties and the reservoir characteristics like porosity, permeability, net-to-gross and hydrocarbon saturation. One of the other benefits of inversion is that the seismic resolution is increased (Veeken, 2007).

For a seismic inversion study, well logs, horizons and seismic data are used to model the earth in terms of layers and acoustic and elastic rock properties. It is assumed that the measurement at the well is correct. The well logs, in combination with the seismic data, are used to fill the inter-well spaces with log properties.

Post and pre-stack inversion methods can be discriminated according to the available input data. Inversion can be done in time or even in the frequency domain. In this study, time domain pre-stack inversion (simultaneous inversion) was performed. The simultaneous inversion methods, that is an AVO inversion technique, uses the Aki and Richards formula (1980) to compute the reflectivity at various offset in the pre-stack domain (Veeken,2007). Furthermore, this process delivers absolute acoustic impedance, v_p/v_S ratio (or shear impedance), and density cubes.

The algorithm uses initial input models to compute synthetic gathers and compares them with the real seismic data (Veeken, 2007). It is simultaneous in the sense that it works on several angle ranges at the same time, which has been shown to be more stable than inversion of a single angle range.

The Aki and Richards formula (1980) calculated the approximate P-wave reflectivity at the various angles (ϴ) in the pre-stack domain.

$$R_{(\theta)} = 0.5\left(\frac{\Delta V_P}{V_P} + \frac{\Delta \rho}{\rho}\right) - 2\left(\frac{V_S}{V_P}\right)^2 \left(2\frac{\Delta V_S}{V_s} + \frac{\Delta \rho}{\rho}\right)\sin^2\theta + 0.5\frac{\Delta V_P}{V_P}\tan^2\theta$$

Where v_p is the average P-velocity between two uniform half spaces, v_S is the average S-velocity and ρ is the average density. This equation can be rewritten in term of P-wave and S-wave impedances:

$$R_{(\theta)} = (1 + \tan^2\theta)\frac{\Delta I_P}{2I_P} - 8\left(\frac{V_S}{V_P}\right)^2 \sin^2\theta\left(\frac{\Delta I_S}{2I_S}\right) - \left(\tan^2\theta - 4\left(\frac{V_S}{V_P}\right)^2 \sin^2\theta\right)\left(\frac{\Delta\rho}{2\rho}\right)$$

It is assumed that the relative changes in ($\Delta v_p/ v_p$), ($\Delta v_S/v_S$) and (Δρ/ρ) are small and the incidence angle θ is much less than 90 degree. This makes that second order terms can be ignored. Inversion is carried out under the assumptions that the earth has approximately horizontal layers and each layers is described by both acoustic and shear impedances (Veeken, 2007).

The simultaneous AVO inversion uses a model driven approach. Independent wavelet estimations are carried out for each partial stack. Inversion is done directly for the desired rock properties like acoustic impedance, shear impedance, v_p/v_S ratio and density. One of the advantages in inversion is that it provides a better resolution and accuracy in the extracted rock properties than the seismic data in itself.

Figure 9.1 illustrates the fundamental inversion workflow that comprises conditioning the well logs to the seismic data, wavelet estimation, low-frequency model building and the seismic inversion itself.

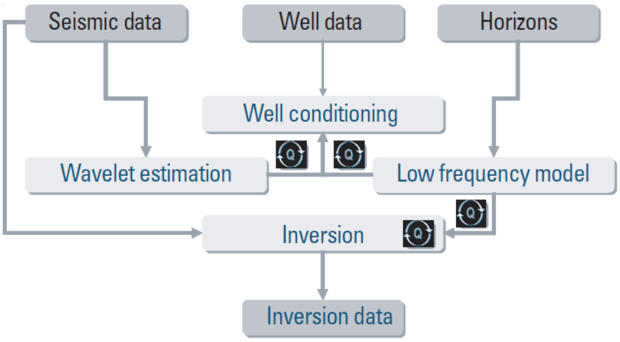

Figure 9.1. Fundamental inversion workflow for seismic data (Schlumberger, 2007).

9.1. Seismic Data Conditioning

Pre-conditioning of the seismic data, which is used as an input to final simultaneous inversion, was performed such as generation of angle stack and applying trim statics. Aim of the preconditioning to align gathers and remove any noise in the data that may impact the AVO trend in the data to provide seismic data that is fit for purpose. In this case only alignment was required.

CDP Trim statics is a process that can fix migration move-out problems on pre-stack data and optimizes trace alignments within a CDP gather. It attempts to determine an optimal time shift to apply to each trace in gather. The shift is determined by cross-correlating of each trace with a reference trace to make the input trace better match than the reference trace. Usually the reference trace is the CDP stacked trace.

In this investigation, the full stack dataset was selected as reference stack for performing the trim statics process to ensure the events are aligned to the interpretation that was picked on the full stack data. This procedure was applied in a time window between 700ms and 2500ms that interval is slightly larger than the selected time window for inversion. Multiple cross correlation window was used which means that cross correlation window length, cross correlation window step and maximum allowed time shift could be defined (Figure 9.2). The following table (Table 9.1) summarises the tested parameters and highlight the best result.

Table 9.1. Summary of tested parameters during the trim statics procedure.

Cross Correlation window length	40ms		120ms		**160ms**	
Cross Correlation window step	2ms		**4ms**		20ms	
Maximum allowed time shift	4ms	**6ms**	8ms	12ms	16ms	

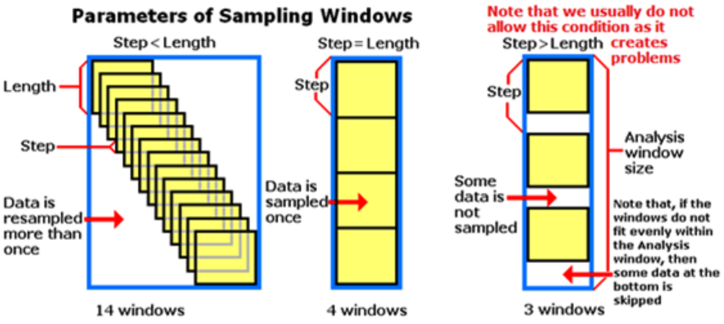

Figure 9.2. Parameters of sampling window by Trim Statics process.

Wavelet estimations and test inversions were performed before and after the statistical alignment in order to evaluate the feasibility of the alignment procedure. Following these tests, it was decided to use the aligned data to generate angle stacks.

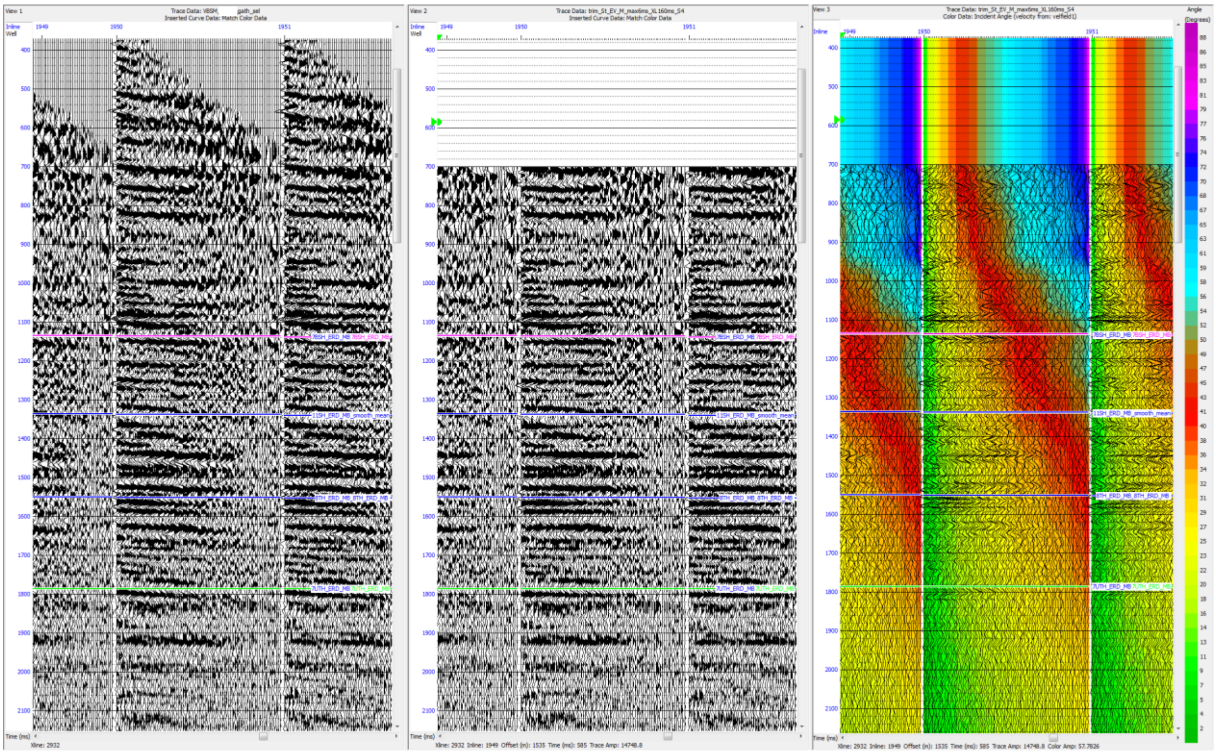

Figure 9.3. Displayed offset gathers before (left) and after (middle) alignment. Additionally, displayed the offset gathers after alignment (right) that are colour coded by angle incident.

Generation of angle gather were necessary as simultaneous AVO inversion was carried out. Figure 9.3 displays the same angle ranges with using the same colours. According to this picture we were able to define the angle range easier which is needed to be used for completion of seismic inversion. First, the offset domain gathers were transformed into incident angle domain (Figure 9.4) using the smoothed migration velocities. Ranges of angle gathers can be stacked together to procedure a set of anglestacks, with better signal to noise, and allowing more stable angle dependent wavelet estimation. Stacks of different angle ranges and angle numbers were tested (Table 9.2) to achieve the optimum seismic inversion results. The final utilised parameters are written by boldface type in Table 9.2.

Table 9.2. Summary of tested parameters during the generation of angle stacks.

<table>
<tr><td>Number of angles</td><td>3</td><td>5</td><td>6</td><td>7</td><td colspan="2">9</td><td>10</td><td>11</td><td colspan="2">12</td><td>14</td></tr>
<tr><td>Angles ranges</td><td>1to45</td><td>1to35</td><td>5to30</td><td colspan="2">5to35</td><td colspan="2">5to37</td><td colspan="2">5to40</td><td colspan="2">8to40</td></tr>
</table>

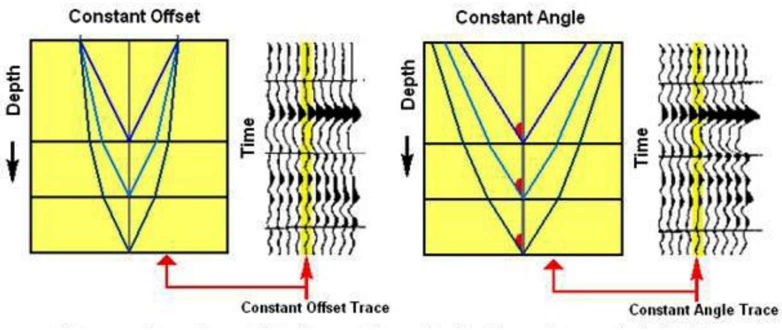

Figure 9.4. Ray paths for traces for offset and angle gathers.

Figure 9.5 (left) illustrates the angle stack by using the previous highlighted angle range and angle numbers. This result is accomplished after the alignment procedure, so this represents the final input for the simultaneous AVO inversion.

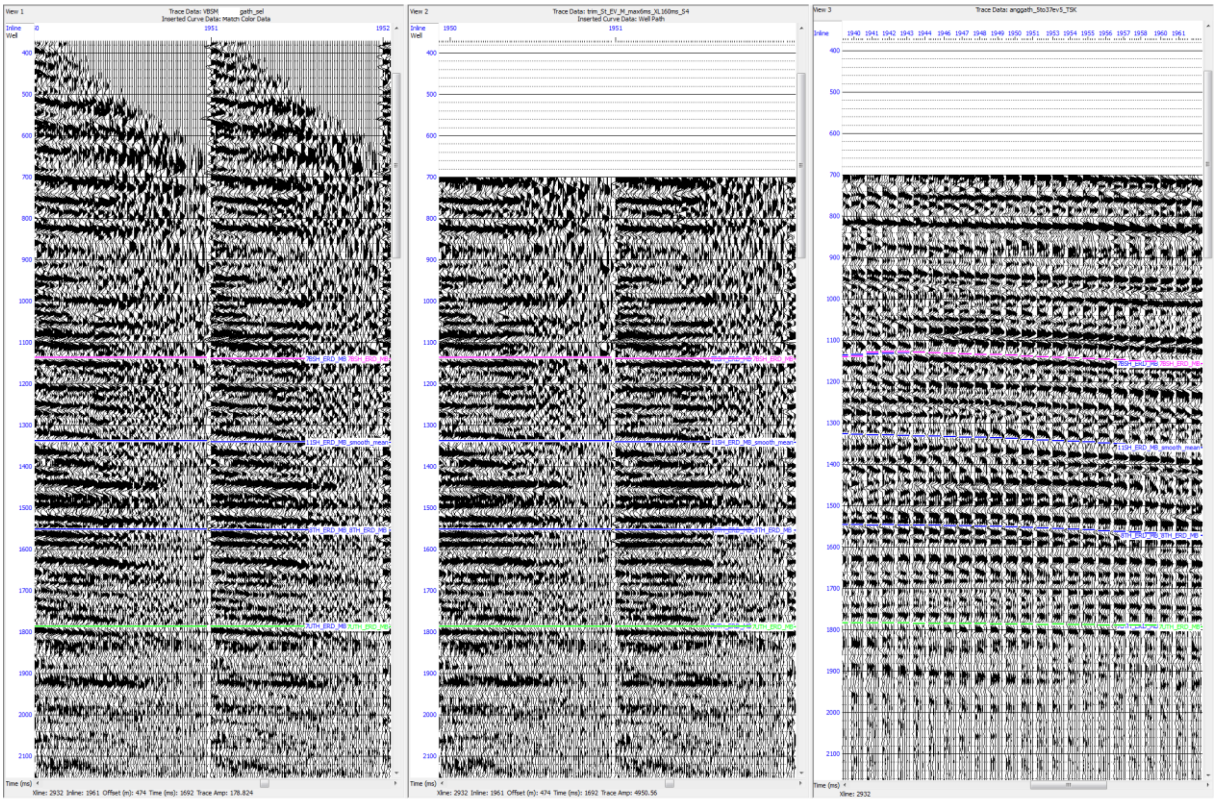

Figure 9.5. Offset gathers before (left) and after (middle) alignment. Additionally, displayed the angle stack gathers (right).

9.2. Well to Seismic tie

Accurate well ties are essential to be able to predict pore fluid and lithological properties from seismic data away from the well. The accuracy of the well ties is controlled mainly by the processing of the seismic data and the construction of the seismic reflectivity model from the well logs (White, 1998).

Well to seismic tie is a calibration process, which involves the comparison of a synthetic seismic trace with the real seismic. If the correlation is sufficient, then the seismic data can be interpreted in terms of the geology.

The well tie process includes several steps, such as the time calibration of the sonic log to the checkshots, a convolution of the time reflection series with a wavelet and comparison to the seismic (Figure 9.6). Although this methodology seems simple, well ties can present considerable problems, usually in the area of the wavelet estimation.

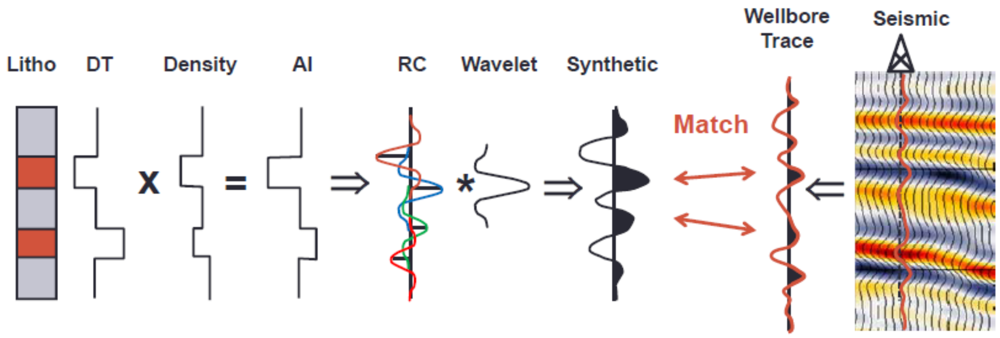

Figure 9.6. Fundament of theory of well to seismic tie.

9.2.1. Well Conditioning

Well conditioning means log editing, log analysis, generation of missing curves and depth-to-time conversion through checkshot. In this study, the sonic and density logs were converted from depth domain to the two-way travel-time domain using the available checkshot. The acoustic impedance series was calculated by multiplication of the density log and the velocity log derived from the sonic log. The reflectivity series was then derived from the acoustic impedance log. The reflectivity series can then be convolved with a wavelet to generate a synthetic seismogram. The calibrated logs are used for estimation of the wavelet that provides the best match between the seismic data and the synthetic seismogram, and also for definition of the low-frequency background models that are used in the inversion.

9.2.2. Wavelet estimation

Wavelets are estimated for each seismic anglestack volume as the convolution operator between the calibrated reflectivity logs and the seismic data. The wavelet that gives an optimum tie of a well log to a seismic section has a characteristic length, shape and timing. Wavelet estimation may be performed either at each well location one at a time, or simultaneously using several wells to determine the best overall wavelet for the wells.

In this study, one of the well (X-001) was used to extract the wavelet for well to seismic tie and for further tasks like model building and seismic inversion. The least square wavelet estimation method in the time domain was carried out. The sonic, shear sonic and density logs were applied to compute the reflectivity log and were used to carry out the synthetic seismic trace. To obtain a better fit between the well logs and the seismic data, different parameters as estimation window and methods were tested (Table 9.3). (The optimum wavelet for use in the final seismic inversion, which is written with boldface type in the following table, is determined based on test inversion results.)

Table 9.3. Tested parameters by estimation of wavelet for well to seismic tie, model building, seismic inversion.

Time window	500-1100 ms	**700-1300 ms**	880-1450 ms
Wavelet length	**120 ms**	80 ms	160 ms
Extraction Type	**Full Wavelet**	Constant Phase	Roy White Algorithm

Since pre-stack inversion was performed, the number of wavelets was determined by the angle gather number. That means that separate wavelets were estimated for each partial angle stack. The use of a separate wavelet for each partial stack allows the simultaneous AVO inversion to take into account the frequency and phase variations with offset. Figure 9.7 demonstrates the extracted wavelet, which shows that higher frequency is given at near angles. With increasing angle the decrease in high frequency content can be observed due to the attenuation which is caused by earth. It is visible that there is a shift on the far angle which can be explained that the Trim statics procedure does not completely resolve alignment issues. However, Trim statics was tested with different parameters that showed that more aggressive parameterisation degraded the final inversion result.

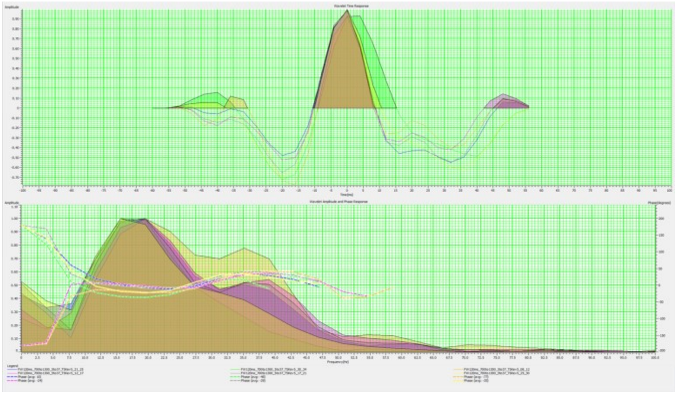

Figure 9.7. Displayed the extracted wavelets.

One of the Quality Control processes from the wavelet extraction is synthetic seismogram display (Figure 9.8 and 9.9). Synthetic seismogram was generated by convolving the reflectivity log with the extracted wavelet, and was compared with the seismic trace extracted along the well trajectory. To obtain a better fit between the well logs and the seismic data, visual ties were applied to the well logs (Figure 9.8 and 9.9). A stretch was applied to the time-depth relationship at well X-001.At the other well (X-016) only a bulk shift (10ms) was required in order to improve the fit between the well data and the seismic and to optimize the cross-correlation between the synthetic seismic data and the seismic data along the well trajectory.

Figure 9.8 and 9.9 demonstrate our well synthetic composite plots as QC. It can be observed that the generated synthetic seismogram shows a good correlation with the seismic traces at well X-001. Well X-016 represents a weak correlation between the synthetic seismogram and the seismic traces. The reason for poor well ties could be that only well X-001 was used to estimate the wavelet. Furthermore, the complicated fault system of the area causes difficulties in extraction of a sufficient wavelet and to achieve a proper match between the synthetic seismogram and the seismic traces.

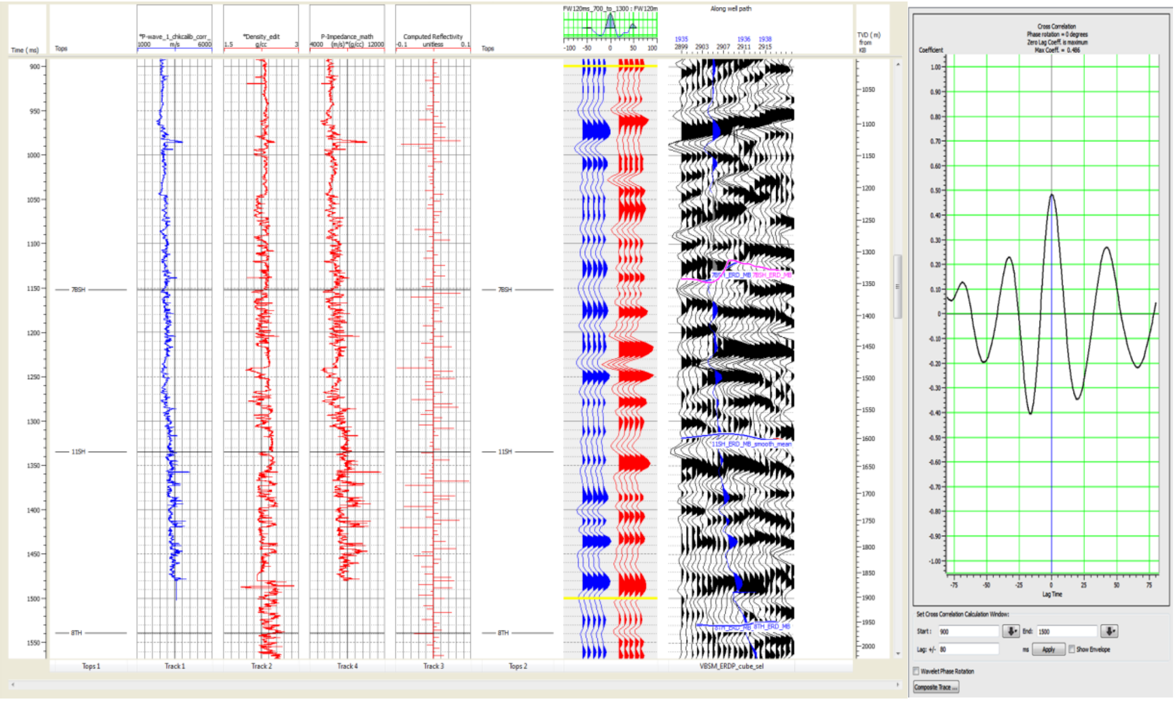

Set Cross Correlation Calculation Window:
Start : 900 End: 1500
Lag: +/- 80 ms

Figure 9.8. Displayed P-wave, density, acoustic impedance and computed reflectivity logs of X-001 well. Moreover, displayed are the synthetic seismogram, the seismic volume and the cross-correlation window.

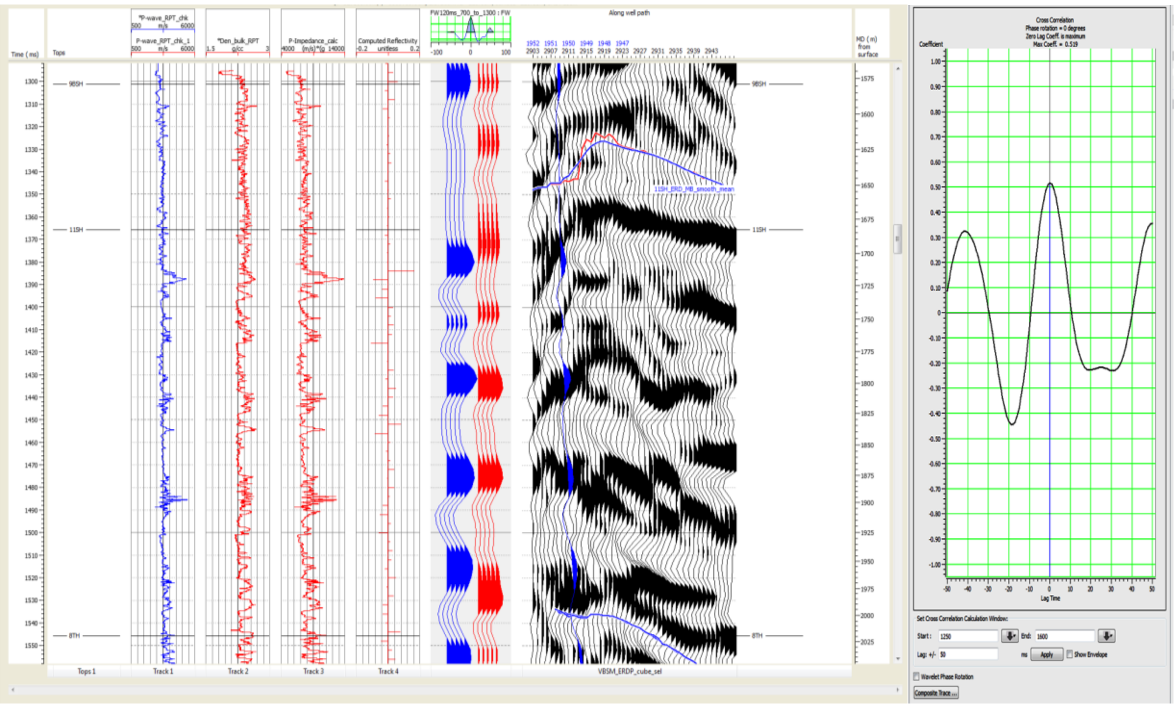

Start : 1250 End: 1600

Lag: +/- 50 ms

Figure 9.9. Displayed P-wave, density, acoustic impedance and computed reflectivity logs of X-016 well. Moreover, displayed are the synthetic seismogram, the seismic volume and the cross-correlation window.

9.3. Low-Frequency Models

Using of low frequency model during seismic inversion enhances the qualitative and quantitative interpretation levels of seismic inversion results. The seismic data is bandlimited (generally of the range from 6 Hz to 60 Hz). It lacks the low frequencies that are essential for relative to absolute property conversion. Since the bandlimited seismic data is inverted in the absence of low frequency model, the inverted physical properties are also bandlimited or relative. To achieve the absolute property we need low frequency modelling to compensate for the missing band of the seismic data. This low frequency component can be obtained from the well data in conjunction with the interpreted horizons (Kumar, 2012). Additionally velocity information may be used as a source of low frequency providing information in the 2-6Hz frequency range.

In this work, a low-frequency model was created for each output domain from the seismic inversion as acoustic impedance, v_p/v_s ratio, and density. A standard low frequency model, where the well information (density, acoustic impedance) are extrapolated away from the wells (X-001, X-016), along the horizons (11SH, 7BSH, 7UTH, 8TH), was used. The third well (X-006) was not used for model building, because its sonic log shows a different trend than the other two sonic logs and it does not fit to the X-001, X-016 wells. Model building was applied only in time window, which ranges from 700ms to 2500ms. Furthermore, the model was filtered to match the low frequency cut-off of the seismic data (Figure 9.10). Different low pass filters were tested to select one that provides the best fit (which is written with boldface type in the following list)

Low pass filters that were tested:

- 10/15 Hz
- 12/14 Hz
- **12/15 Hz**
- 14/15 Hz

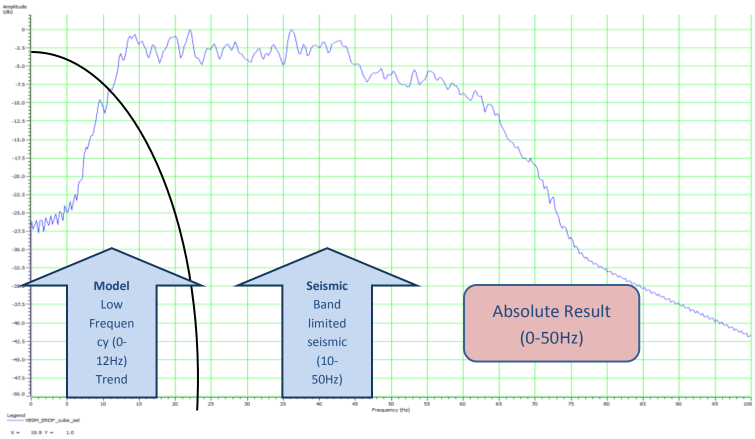

Figure 9.10. Displayed our amplitude spectrum with the predicted low pass filter, additionally displayed are the theory behind the building of a low frequency model.

Low frequency models of acoustic impedance, v_p/v_S ratio, and density were generated, which are displayed in Figure 9.11, Figure 9.12 and Figure 9.13. It can be seen that all of the models correlate with the observed structure in the seismic volume. Additionally, comparison of the models to the well trace show a good match if we ignore the well (X-006), which was not used in the model building process.

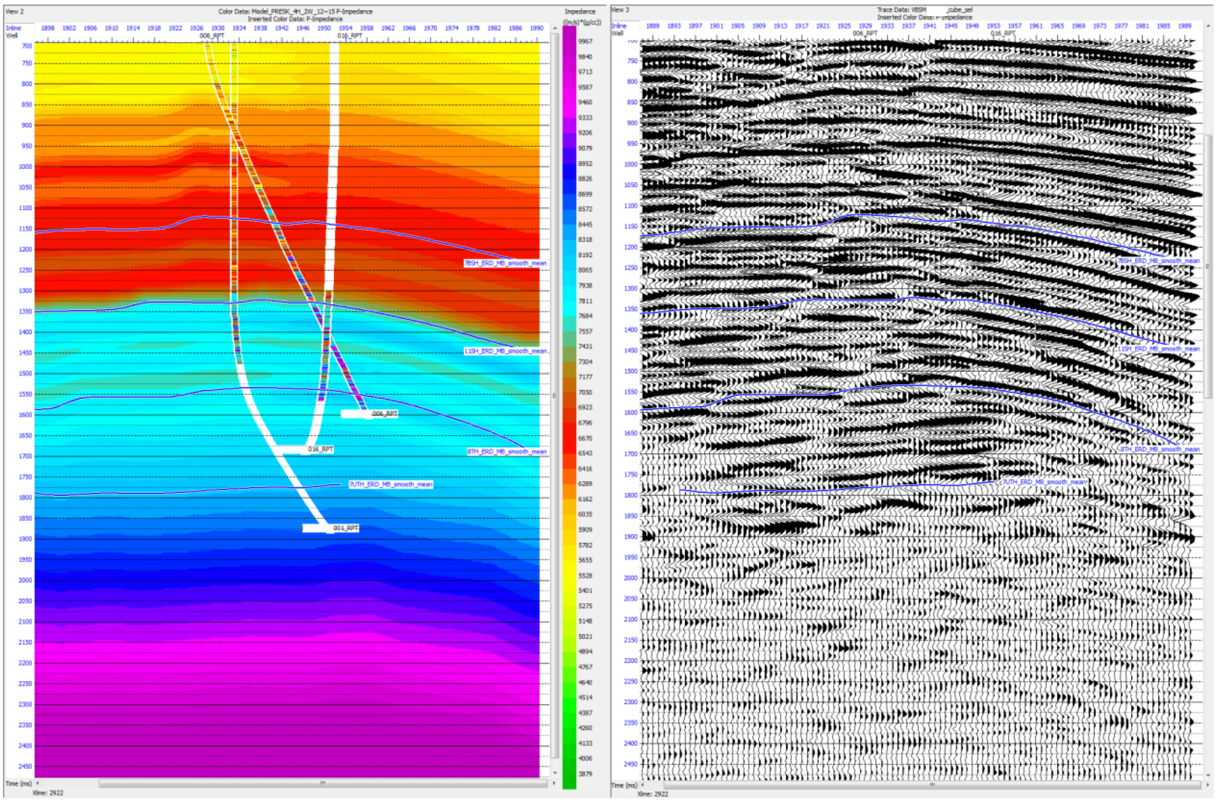

Figure 9.11. Displayed the generated acoustic impedance model with the inserted well path and the acoustic impedance log (left) and the seismic volume (right).

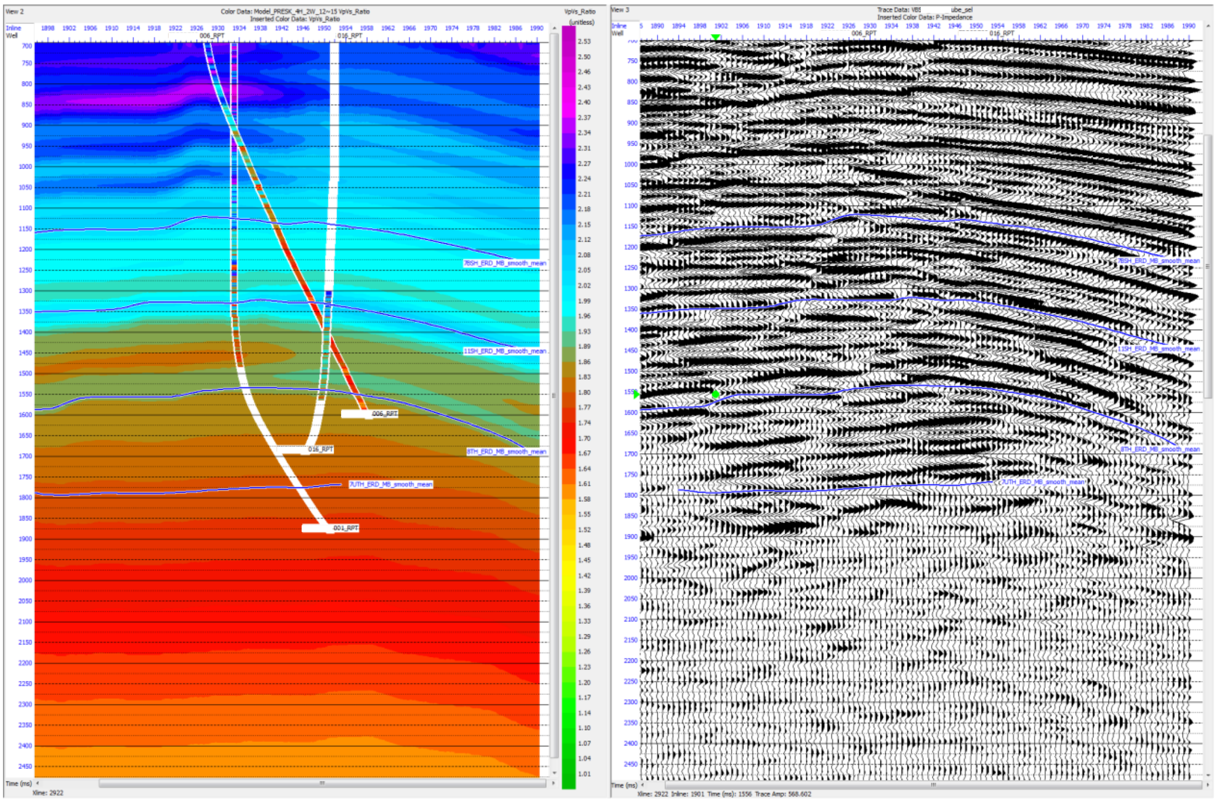

Figure 9.12. Displayed the generated v_p/v_S ratio model with the inserted well path and the v_p/v_S ratio log (left) and the seismic volume (right).

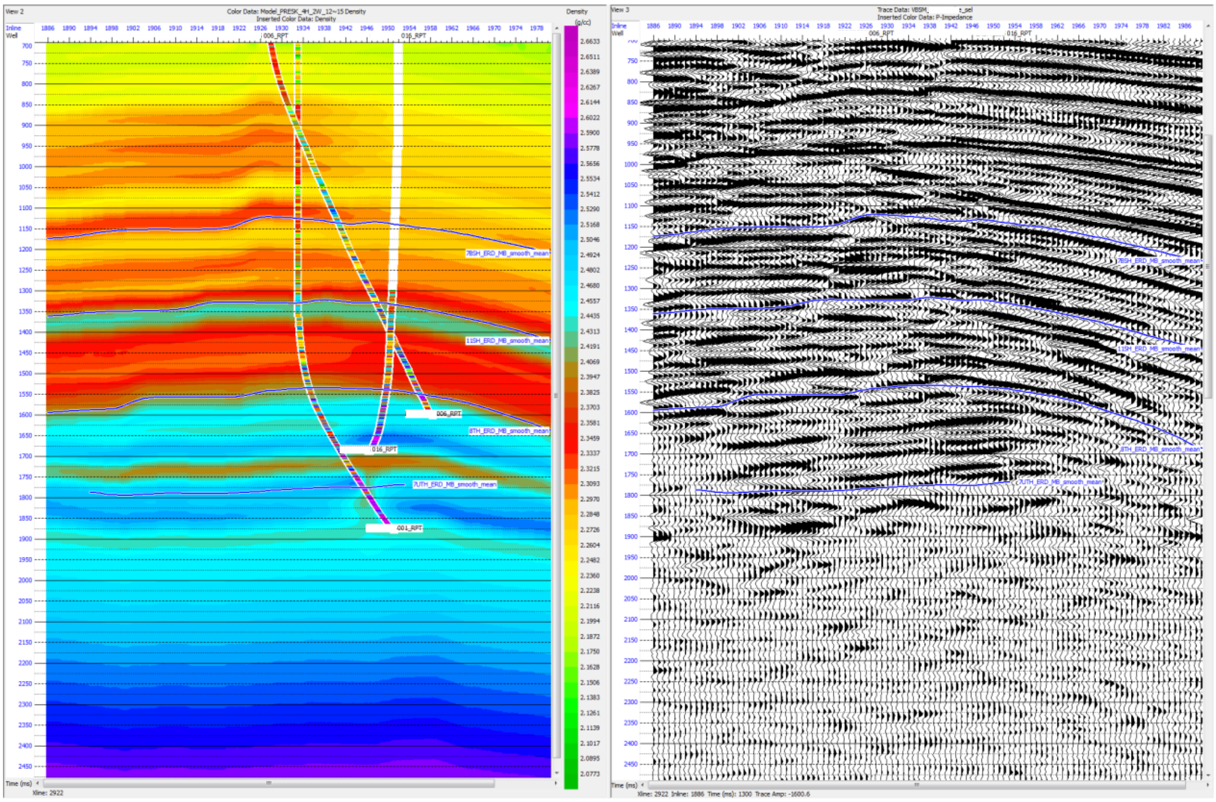

Figure 9.13. Displayed the generated density model with the inserted well path and the density log (left) and the seismic volume (right).

9.4. Seismic inversion

In this part, the inversion parameters, which were used for the final inversion process and the seismic simultaneous AVO inversion results, are described. The conditioned seismic data were inverted for acoustic impedance, v_p/v_s ratio and density, using the low frequency models and extracted wavelets.

Inversion parameter testing was carried at the well locations. Testing included single and multiwell wavelets, different low pass filters by model building, number of angles that were used, the parameterization of Trim statics process and constraining the density result. Testing showed the biggest impact on the final inversion results was due to the wavelets.

Six aligned angle stacks were inverted between 750 and 2000 ms TWT. The inversion results were delivered for the time window 750 to 2000 ms TWT. The LFM models were applied during the inversion, whose building process was defined in the previous part.

Separate wavelets were estimated for each partial stack. Using only the X-001 well, full wavelet extraction type was carried out with a wavelet length of 120ms and in a time window between 700ms and 1300ms. The top and the bottom of the inversion window includes edge effects related to the wavelets length and should not be included the evaluation.

On the following pages along, I would like to present the final inversion results. The next Figures (Figure 9.14, 9.15 and 9.16) display the simultaneous AVO inversion results, such as acoustic impedance, v_p/v_S ratio and density volume next to the corresponding model volume. The locations of the wells are also shown and the equivalent logs are displayed along the wells. As it was mentioned earlier by model building section, two of the three wells were applied for generation of low frequency model and for completion of inversion process. It can be observed that these two of the wells represent an adequate match even with the model and with the inversion result. It should also be considered that the depth of penetration of the well logs is limited to maximum depth of about 2000m which means there is no data available to directly QC the inversion results over the deeper part of the inversion window.

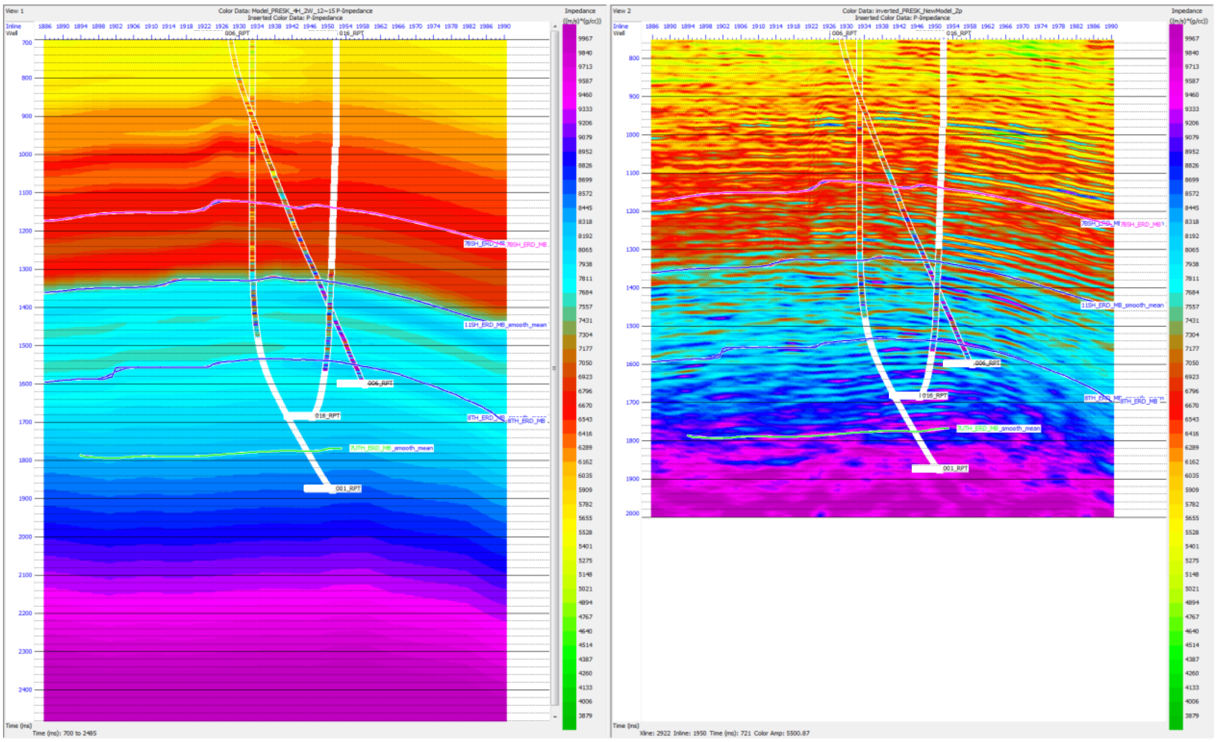

Figure 9.14. Displayed the generated acoustic impedance model with the inserted well path and the acoustic impedance log (left) and the acoustic impedance volume derived from the simultaneous AVO inversion process with the inserted well path and the corresponding well logs (right).

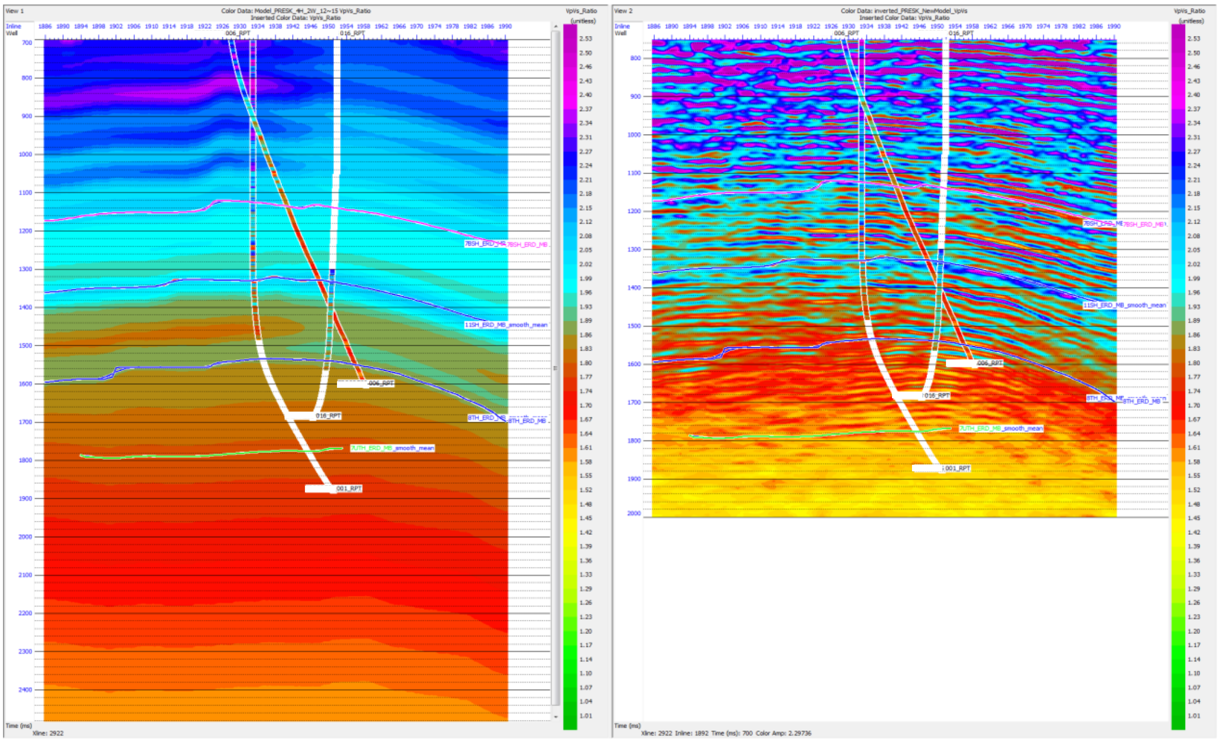

Figure 9.15. Displayed the generated v_p/v_S ratio model with the inserted well path and the v_p/v_S ratio log (left) and the v_p/v_S ratio volume derived from the simultaneous AVO inversion process with the inserted well path and the corresponding well logs (right).

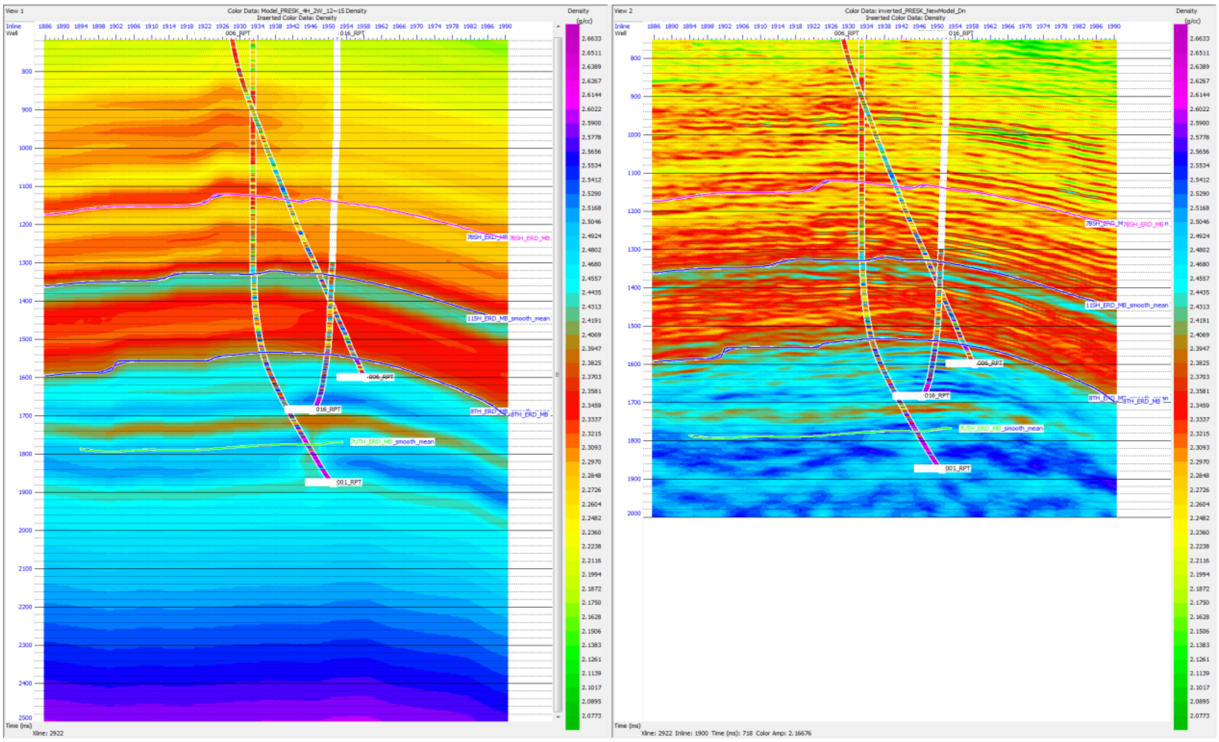

Figure 9.16. Displayed the generated density model with the inserted well path and the density log (left) and the density volume derived from the simultaneous AVO inversion process with the inserted well path and the corresponding well logs (right).

The cross plots presented in Figure 9.17 show the acoustic impedance, v_p/v_s ratio and density in the well log data and in the final simultaneous AVO inversion results. The cross plots assist as a quality control where the X-001 and X-016 well log data were used.

The match between the acoustic impedance inversion result and the well logs is considered good with a cross correlation of more than 74%. The match between the v_p/v_s ratio inversion result and the well logs is considered also good with a correlation of 69%. The match between the density inversion result and the well logs is considered weak with correlation of 58%. However, this result could be reasonable as testing showed constraining the density result improved the overall tie in terms of acoustic impedance and v_p/v_s ratio. Also, the angle ranges is limited to 37 degrees and the far angle stacks are contributing to the density volume prediction. The far angle stacks are lower frequency and noisier than the nearer angle stacks.

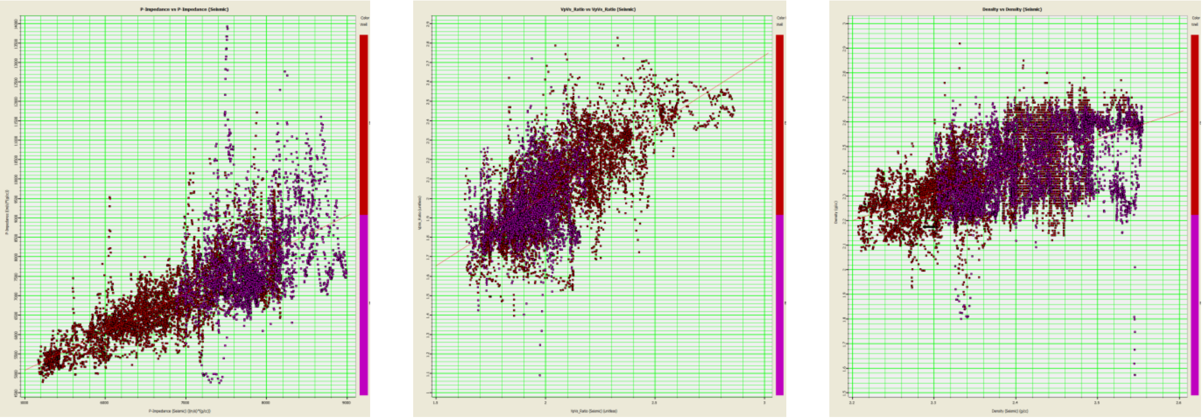

Figure 9.17. Inversion results versus well log data: acoustic impedance, v_p/v_S ratio and density, using X-001 and X-016 wells for correlation.

The next pictures (Figure 9.18 and 9.19) represent the inversion results along the wells (X-001, X-016). Sonic, acoustic impedance, v_p/v_S ratio and density logs are displayed as well as the corresponding logs derived from the simultaneous AVO inversion results. In the three seismic traces, acoustic impedance, v_p/v_S ratio and density inversion results are showed and the equivalent logs are inserted into the inversion result along the wells.

It can be observed again that the acoustic impedance and v_p/v_S ratio inversion results represent a good match with the equivalent well logs. However, the density inversion volumes show a poor match with the density logs, because the far angle stacks, which are noisier than the nearer angle stacks, were used to generate the density inversion result.

In addition, it can be seen that the inversion results of X-001 well are corresponded a better fit with the original logs than in case of the X-016 well. However, it is obviously because only the X-001 well was used to extract the wavelet.

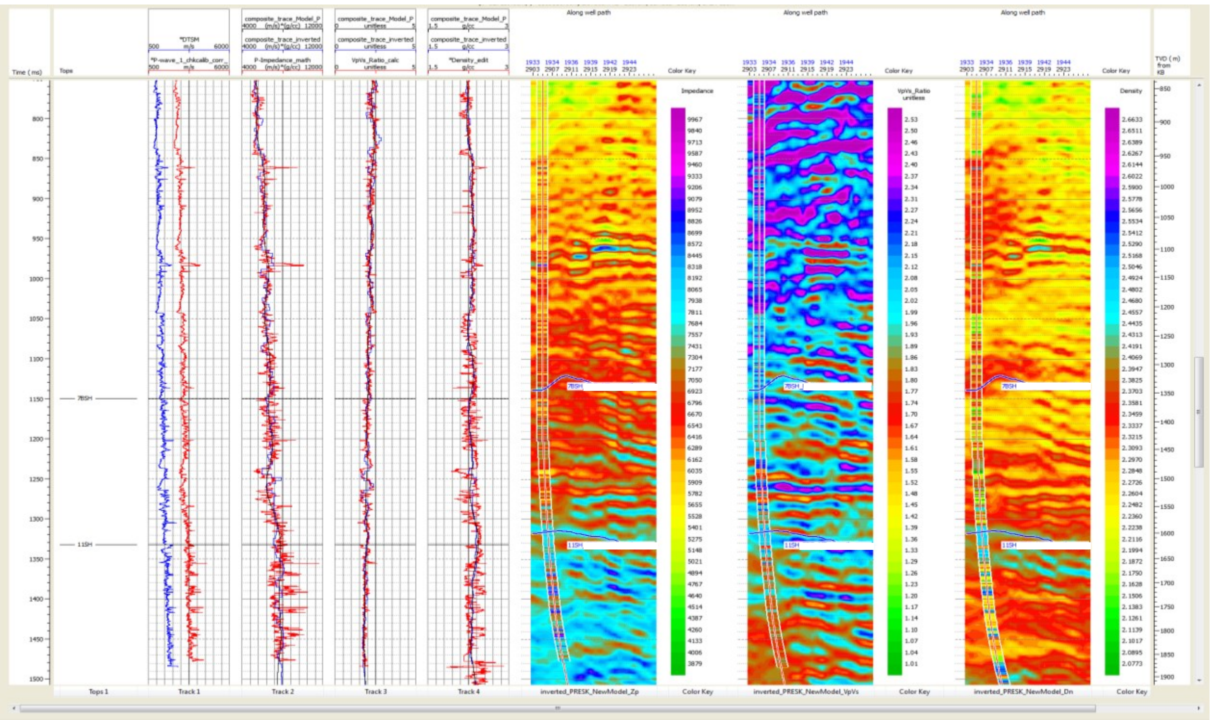

Figure 9.18. Displayed sonic, acoustic impedance, v_p/v_S ratio and density logs of X-001 well. Additionally, seismic traces represent the simultaneous AVO inversion results (acoustic impedance, v_p/v_S ratio and density volumes) with inserted corresponding logs.

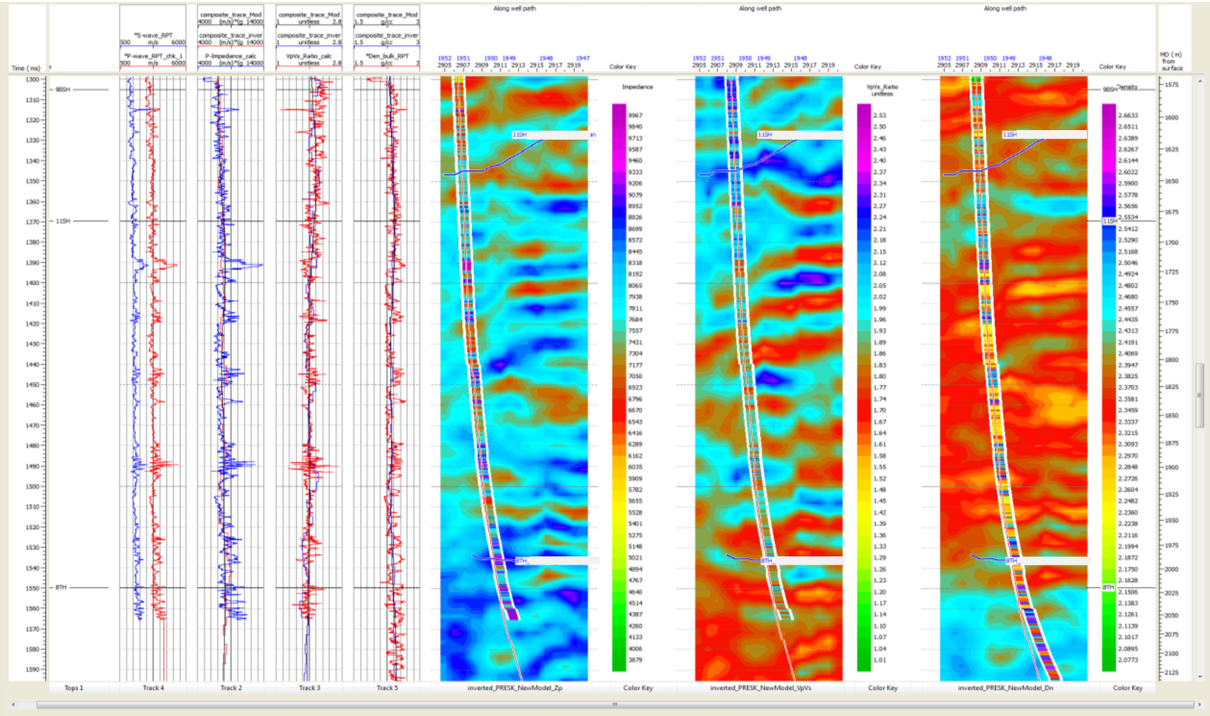

Figure 9.19. Displayed sonic, acoustic impedance, v_p/v_S ratio and density logs of X-016 well. Additionally, seismic traces represent the simultaneous AVO inversion results (acoustic impedance, v_p/v_S ratio and density volumes) with inserted corresponding logs.

10. Rock Physics Templates and its application

The Rock Physics Template (RPT) is a combination of depositional and diagenetic trend models and the Gassmann fluid substitution model, which is also a toolbox for efficient lithology- and pore fluid interpretation of well log data and elastic inversion results (Avseth, 2010). Ødegaard and Avseth (2004) developed such cross-plots to RPT where v_p/v_s ratio versus acoustic impedance are plotted and further it demonstrates the difference between sand and shale, the change of properties from pore fluids of gas to water and the influence of porosity. Figure 10.1 show a cross-plot based on a figure from Ødegaard and Avseth (2004), additionally arrows are displayed that represent the influence of pressure and grain cementation.

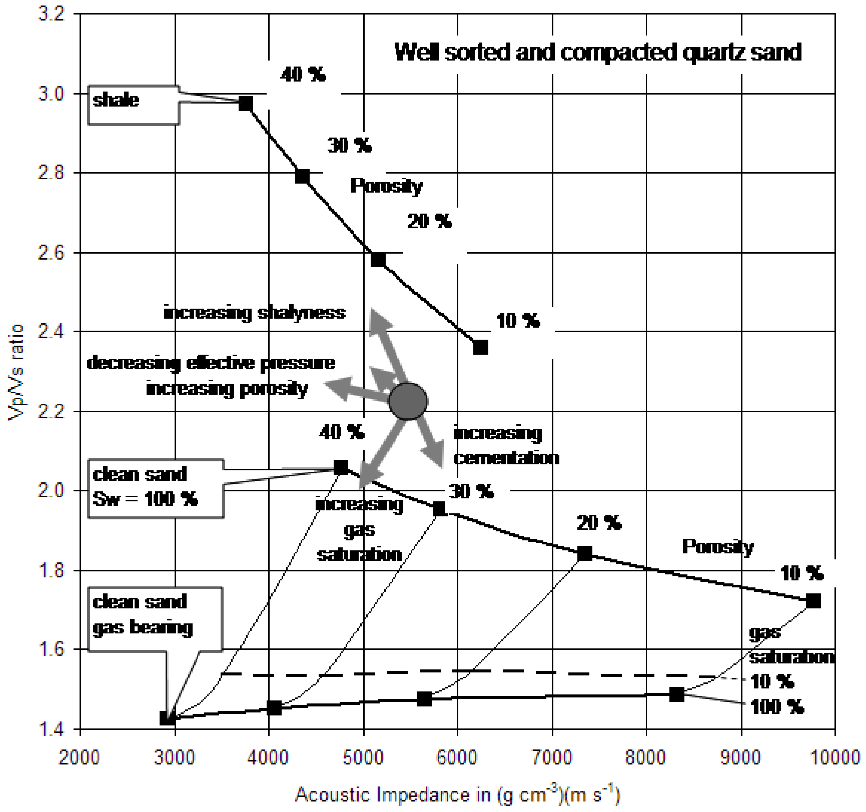

Figure 10.3. Cross-plot v_p/v_s versus acoustic impedance AI, drawn after a figure „Rock Physics Template” from Ødegaard and Avseth (2004). „The theoretical trends are shown for idealized silici-clastic lithologies. The effects of changing reservoir parameters on a point of the crossplot is here shown by arrows” (Ødegaard and Avseth, 2004).

Moreover it has to be taken into account that the RPTs are site- (basin-) specific and honour local geologic factors. Geologic constraints on rock physics models are lithology, mineralogy, burial depth, diagenesis, pressure and temperature. All these factors must be determined if RPTs are generated for a given basin. Particularly it is essential to include only the expected lithologies for the studying area when generating the rock physics templates. But even the defined system (either siliciclastic or carbonate system), the mineralogy can be highly variable.

In consequence, it can be observed that the shale trend will typically be basin-specific, whereas the clean brine sand trend will have more general validity.

The effective pressure, pore pressure and lithostatic pressure are determined by the water depth and the burial depth. These parameters are important for the calculation of fluid properties to determine the effective stress on the grain contacts and to have an idea about the level of the rock compaction and diagenesis.

In the modelling of the RPTs it is also needed to know the acoustic properties of the mud filtrate, formation water and hydrocarbons in the area of investigation. Temperature, pressure, brine salinity, gas gravity, oil reference density (API) and oil GOR are also required input parameters.

10.1. Key steps of modeling the RPTs

Modelling of RPTs is to calculate velocity-porosity trends from the expected lithologies for various burial depths using the earlier presented models. To briefly summarize we apply Hertz-Mindlin contact theory to estimate the dry bulk and shear moduli at critical porosity (Figure 10.2). In the following step we interpolate between the high-porosity end member and the zero-porosity mineral point, choosing the modified Hashin-Shtrikman bounds (Figure 10.2). The modified lower and the upper Hashin-Shtrikman bounds are considered to nicely predict the elastic moduli as function of porosity reduction from unconsolidated or cemented rocks, respectively. The next step is to calculate the elastic moduli of a brine saturated rocks using Gassmann theory (Figure 10.2). From these the v_p, v_s

the density of brine- or gas-saturated rocks can be calculated, and finally the acoustic impedance (AI) and the v_p/v_S ratio can be computed (Figure 10.3) (Avseth, 2009).

These calculation steps were applied in this study (Figure 10.2) to display the appropriate lines for our dataset in Rock Physics Template (Figure 10.3).

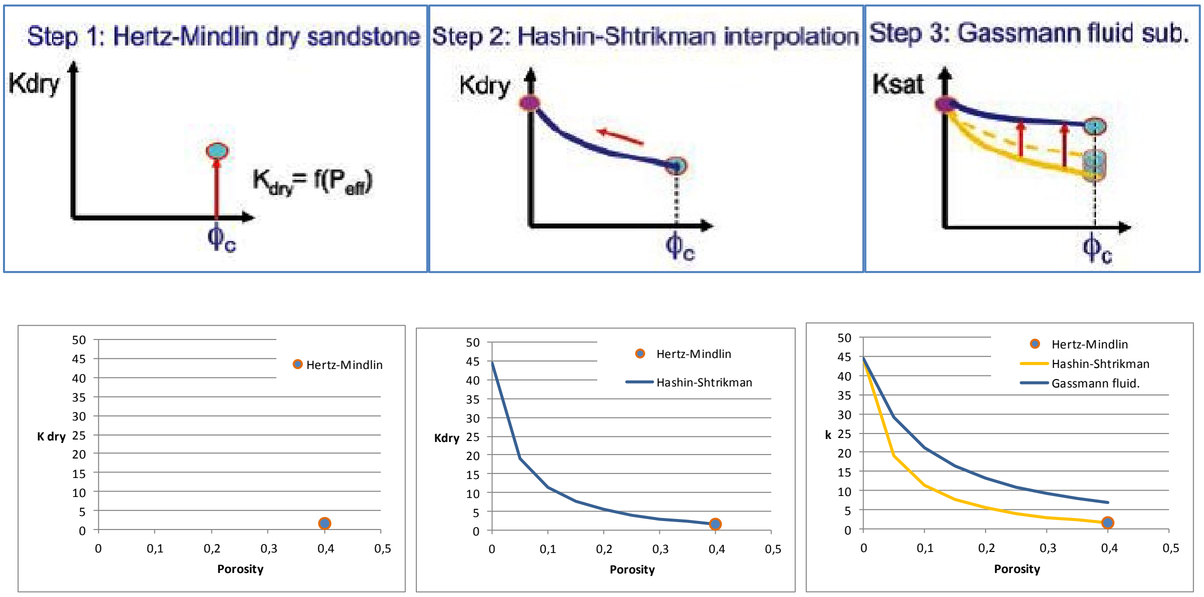

Figure 10.2. Illustration of three-step approach for modelling the effective moduli of sand, additionally the results of these model calculations is displayed to characterize our data set.

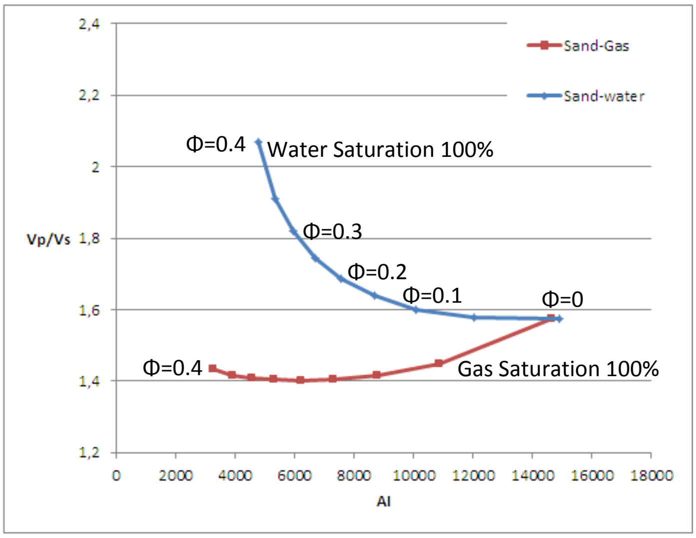

Figure 10.3. Displayed is the calculated water (blue) and gas (red) saturated sand-lines in the v_p/v_S ratio versus AI cross-plot. Furthermore, the points on the line illustrate the changing porosity.

10.2. Results and interpretation of laboratory data

Figure 10.4 shows the plot of v_p/v_S ratio versus acoustic impedance for saturated and dry carbonate and sandstone samples. The typical zones for sandstone (dry and saturated) and shale are displayed additionally. Compared with sandstones, the carbonates show higher acoustic impedance, which can easily be explained with the higher density, higher compressional wave velocity and also the low porosity. The difference between brine saturated and dry sample is clearly visible. The saturated samples show a higher v_p/v_S ratio and slightly higher acoustic impedance.

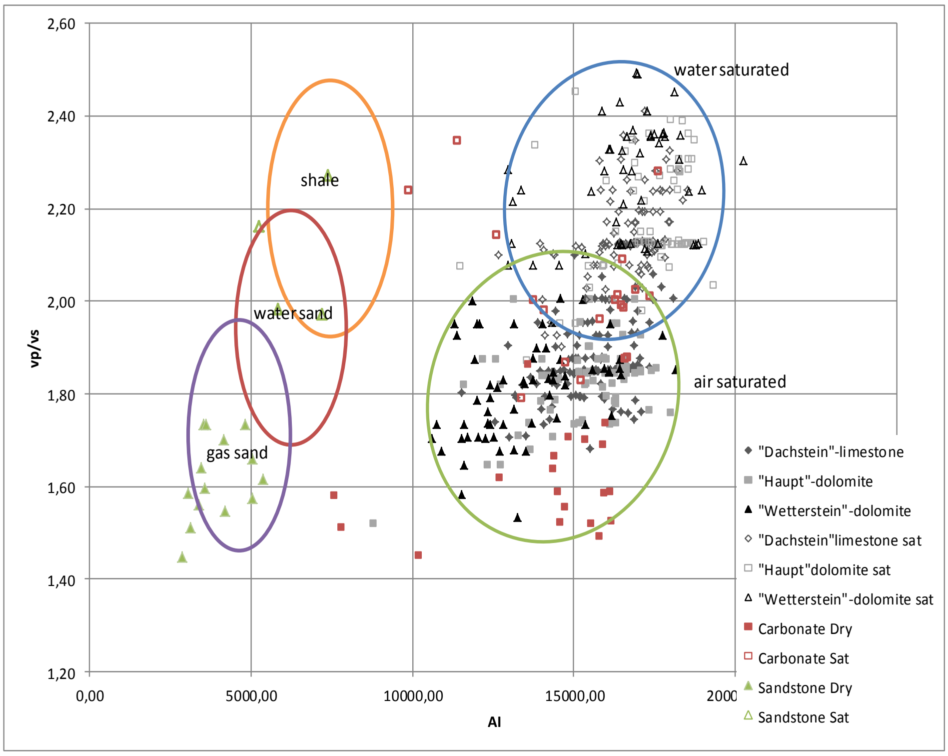

Figure 10.4. Displayed is v_p/v_S ratio versus acoustic impedance for dry and saturated carbonate and sandstone samples, additionally displayed the areas where the sandstone (dry, saturated) and shale would be positioned.

This lithology separation can be seen also in the borehole data if v_p/v_S ratio versus acoustic impedance is displayed (Figure 10.5). The carbonates have higher acoustic impedance than sandstone. This can be explained due to the lower bulk and shear moduli and higher porosity of sandstone samples.

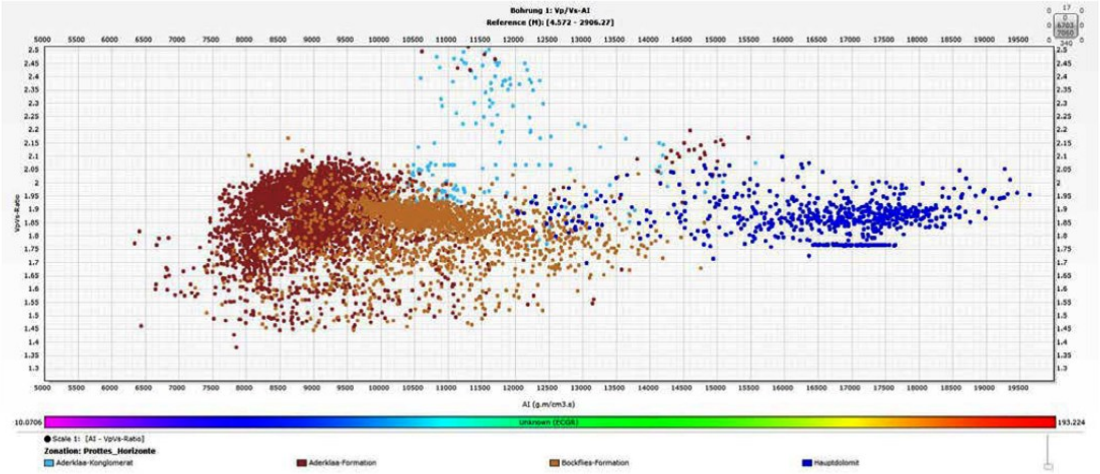

Figure 10.5. Displayed is v_p/v_S ratio versus acoustic impedance for borehole data that colour coded by lithology. Separation of the lithology becomes clearly visible.

Figure 10.6 shows the v_p/v_S ratio versus acoustic impedance with calculated brine and gas saturated lines for sand, that also represent the porosity changing (0; 0,05; 0,1; 0,15; 0,2; 0,25; 0,3; 0,35; 0,4). The input parameters of model calculations were determined as bulk modulus of sandstone is 44,63 GPa and the shear modulus of sandstone is 38,97 GPa. 0,01412 GPa was chosen as effective pressure due to the depth information of the cores.

Our sandstone samples show good results with the calculated lines. The water saturated samples lie above the 100% water saturated sand-line, which could be explained due to the mineral constituent´ properties. The dry samples are located between the 100% water and 100% gas saturated lines.

For carbonates the calculated Hashin-Shtrikman bounds are displayed, additionally the porosity (like by sandstone) is shown by markers (Figure 10.6). The used bounds are the upper one and moreover calculated are lines with 75% and 50% of the upper bound. For model calculation the input parameters were given as bulk modulus of carbonates is 95 GPa and the shear modulus of carbonates is 34 GPa.

It can be observed that the calculated model lines can display the correlation for the saturated samples. The 75% line shows good results for the “Haupt”-dolomite and the “Dachstein”-limestone, the 50% bound for the “Wetterstein”-dolomite. The “Carbonate” data scatter is too much for choosing the appropriate line. The dry samples may be characterized by upper bound that is the lower bound for the data in case of v_p/v_S ratio and acoustic impedance cross-plot. However, the porosity prediction of the bounds does not fit with our data. Possible explanation can be the low porosity, a more complex pore system of the carbonates and influences of the mineral matrix.

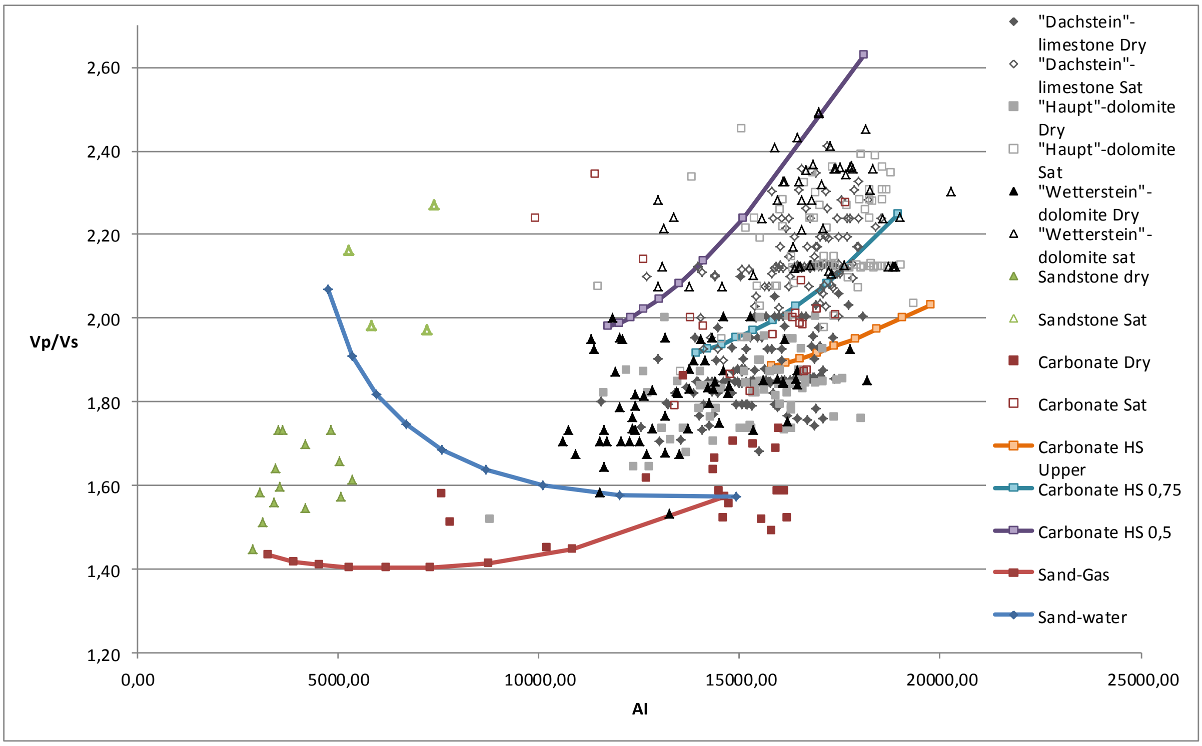

Figure 10.6. v_p/v_S ratio versus acoustic impedance with calculated 100% water and gas saturated lines for sand, additionally with the calculated Hashin-Shtrikman bounds (upper bound, 75% and 50% of the upper bound) and displayed also are dry and water saturated sandstone and carbonate samples.

10.3. RPT analysis of well-log data

In this part I present how to construct the template for well-log analysis and it is also demonstrated how well-log data can be used to calibrate/validate the RPTs before the interpretation of seismic data. The reliability of RPT interpretations depends on the validity of the lithological trends for the area under investigation. Well log data, if available, should be used to verify the validity and guide the selection of RPTs (Ødegaard, 2004).

First, the process to verify the validity of the selected RPT in siliciclastic system using well log data is shown. The available well logs, which were also used to guide the selection of RPTs, were Volume of Clay, Water Saturation and Effective Porosity. For calculation of the appropriate water and gas saturated lines, the input parameters of sand were used that are summarized in Table 10.1.

Table 10.1. Summary of input parameters of calculations.

	k [GPa]	μ [GPa]	ρ [g/cm^3]	Effective Pressure [GPa]	Critical Porosity [%]
Sand	44,63	38,97	2,69		
Brine	2,38	0	1,090		
Gas	0,021	0	0,10	0,01412	40

Figure 10.7 shows the v_p/v_S ratio versus acoustic impedance cross-plot superimposed onto the appropriate RPTs, which includes porosity trends. In addition, the v_p/v_S ratio and acoustic impedance logs of wellX-001are displayed. The logs are colour coded using the Clay Volume log. According to the Clay Volume log, we can easily discriminate between the shale and sand population. The clean 100% water saturated line, lies on the data points that contain less than 30% clay.

This calculated sand trend line was displayed in the same cross-plot, but the well-logs were colour coded using the Water Saturation log (Figure 10.8). It becomes visible that gas saturated population can be discriminated from the water saturated one due to their lower v_p/v_S ratio and acoustic impedance values. The acoustic impedance decreases due to the density effect of the gas. The `gas sand´ population plots well below brine sand trend and roughly along the lines, which indicate the effects of increasing gas saturation.

Finally, the sand trend lines were tested due to the porosity effects. The v_p/v_S ratio versus acoustic impedance cross-plot was displayed superimposed onto the appropriate RPTs. Furthermore, the log data were colour coded using the effective porosity log (Figure 10.9). It can be observed that the porosity trend shows a good match with the well-log.

Therefore, it can be considered that the appropriate RPT was determined that obtains a good validity for interpretation of elastic inversion results.

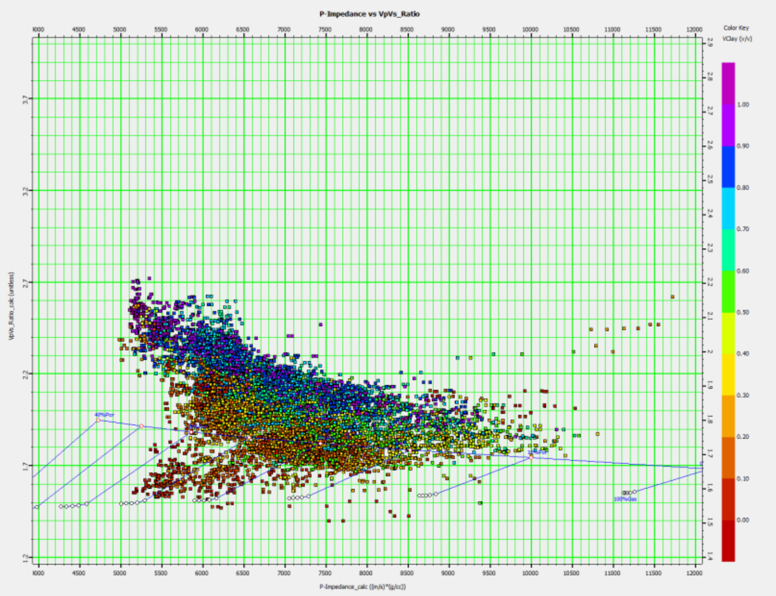

Figure 10.7. v_p/v_S ratio versus acoustic impedance cross-plot, with theoretical rock physics trend for clean compacted brine filled quartz sand superimposed. The trend is plotted as function of porosity. The effects of different gas saturations are added below the brine sand trend. The data are colour coded using the Clay Volume log.

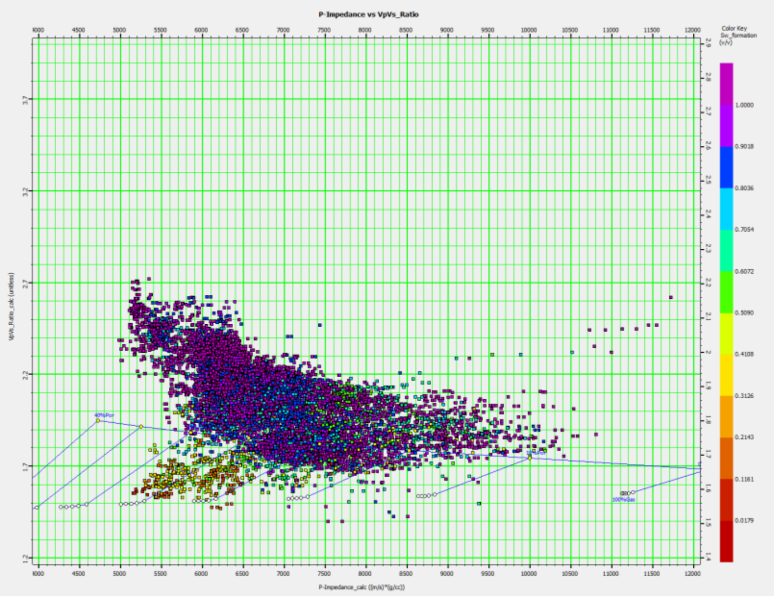

Figure 10.8. v_p/v_S ratio versus acoustic impedance cross-plot, with theoretical rock physics trend for clean compacted brine filled quartz sand superimposed. The trend is plotted as function of porosity. The effects of different gas saturations are added below the brine sand trend. The data are colour coded using the Water Saturation log.

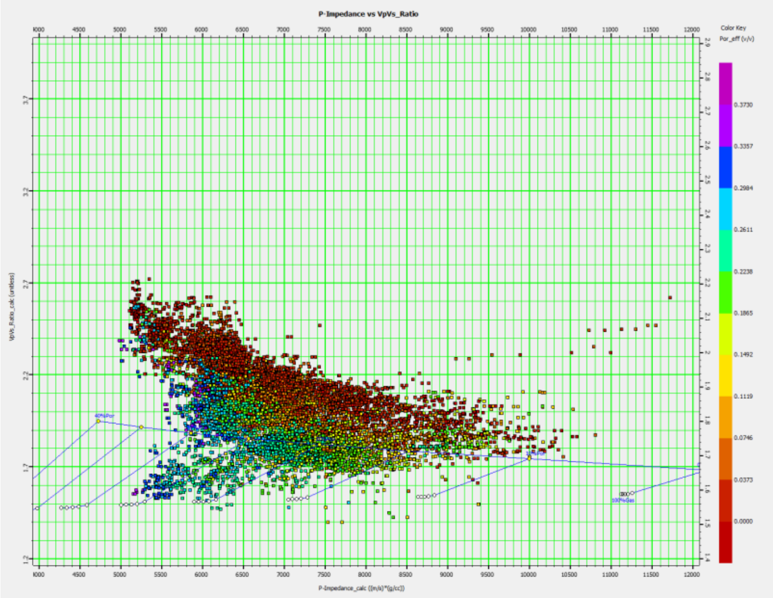

Figure 10.9. v_p/v_S ratio versus acoustic impedance cross-plot, with theoretical rock physics trend for clean compacted brine filled quartz sand superimposed. The trend is plotted as function of porosity. The effects of different gas saturations are added below the brine sand trend. The data are colour coded using the Effective Porosity log.

Furthermore, our aim was to prove the validity of the RPTs for carbonate reservoir. Carbonates have a more complex pore system due to the complicated diagenetic processes that occur in rocks after deposition. As we have seen earlier (in Chapter 7), Gassmann fluid substitution theory is not properly valid for carbonate rocks. To solve this problem, Hashin-Shtrikman bounds for dry and saturated rocks were computed that characterize our gas and water, or oil saturated carbonate dataset.

Figure 10.10, 10.11 and 10.12 show the v_p/v_S ratio versus acoustic impedance cross-plot with the calculated Hashin-Shtrikman bounds. The used bounds are the upper one and additionally calculated lines with 75% and 50% of the upper bound for saturated rocks. In addition, Hashin-Shtrikman upper bound was computed for gas saturated (dry) rocks.

The first example is the earlier mentioned (in Chapter 7) well, where only carbonate layers have shear-sonic data, so only the carbonates can be displayed in the cross-plot (Figure 10.10). It becomes visible in Figure 10.10 that porosity increases with decreasing acoustic impedance. Due to the resistivity log it is known that gas fills the pores of the rock. Thereby, Hashin-Shtrikman upper bound, which was computed for dry samples, describes our dataset well.

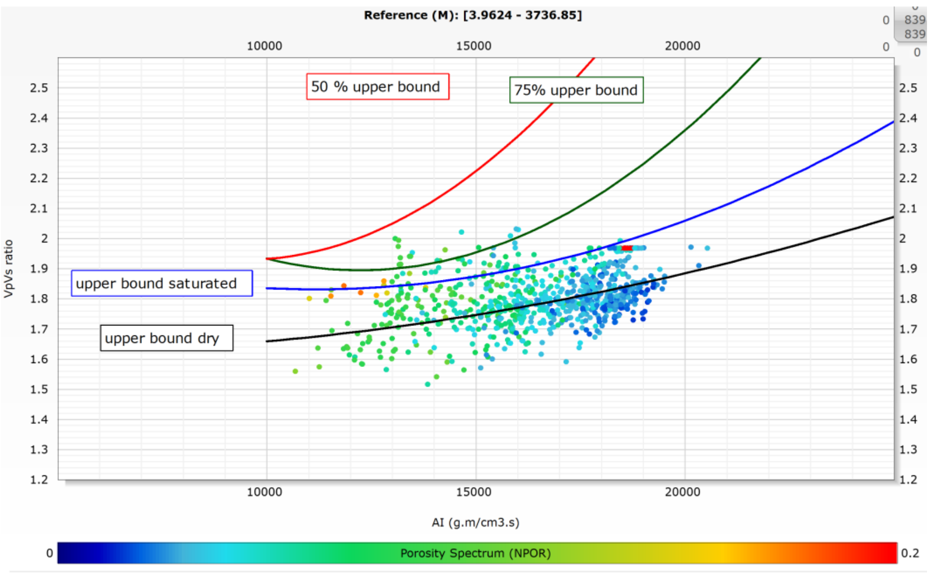

Figure 10.10. Displayed are well log data with calculated Hashin-Shtrikman upper bound for saturated and dry samples and 75% and 50% of the saturated upper bound in v_p/v_S ratio versus acoustic impedance cross-plot. The points are colour coded using Neutron Porosity log.

Figure 10.11 shows our second carbonate example, which presents that the carbonates have low Gamma Ray value, but high acoustic impedance. Thereby, the discrimination between sandstones and carbonates can be done easily. The carbonate data points can be characterized by Hashin-Shtrikman upper bound and 75% of the upper bound that were computed for brine-saturated samples.

Figure 10.12 illustrates that carbonate rocks obtain much lower porosity than siliciclastic rocks. However, increasing porosity can be observed with decreasing acoustic impedance. The prediction of porosity due to the Hashin-Shtrikman bounds is not possible, which can be explained with low porosity and a complex pore system. The prediction of pore fluid from the borehole data is also more difficult in case of carbonate system than by siliciclastic system. Possible explanation can be the influences of the mineral matrix.

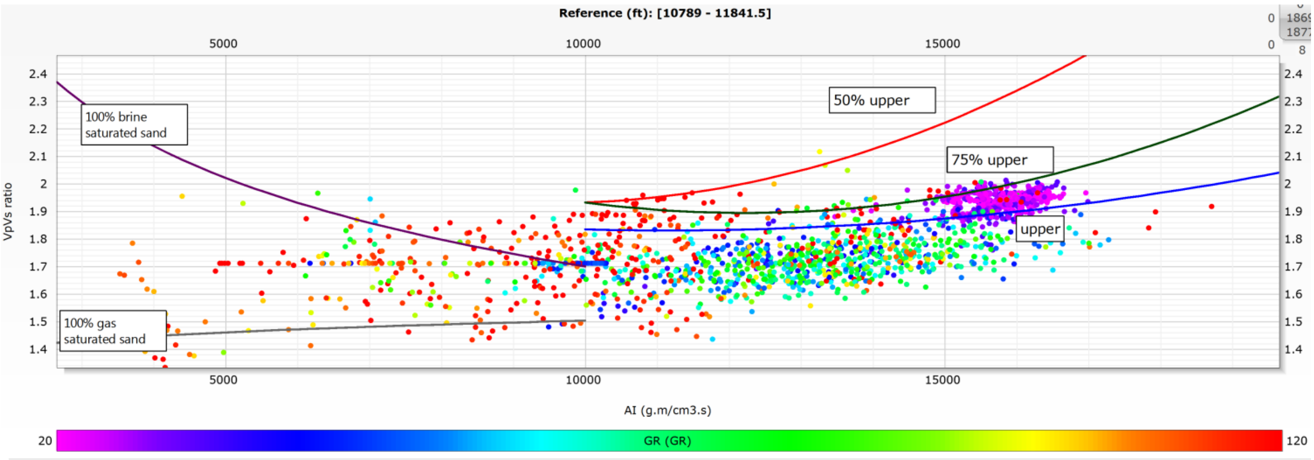

Figure 10.11. Displayed are well log data with calculated Hashin-Shtrikman upper bound for saturated (blue) samples and 75% (green) and 50% (red) of the saturated upper bound in v_p/v_s ratio versus acoustic impedance cross-plot. The points are colour coded using Gamma Ray log.

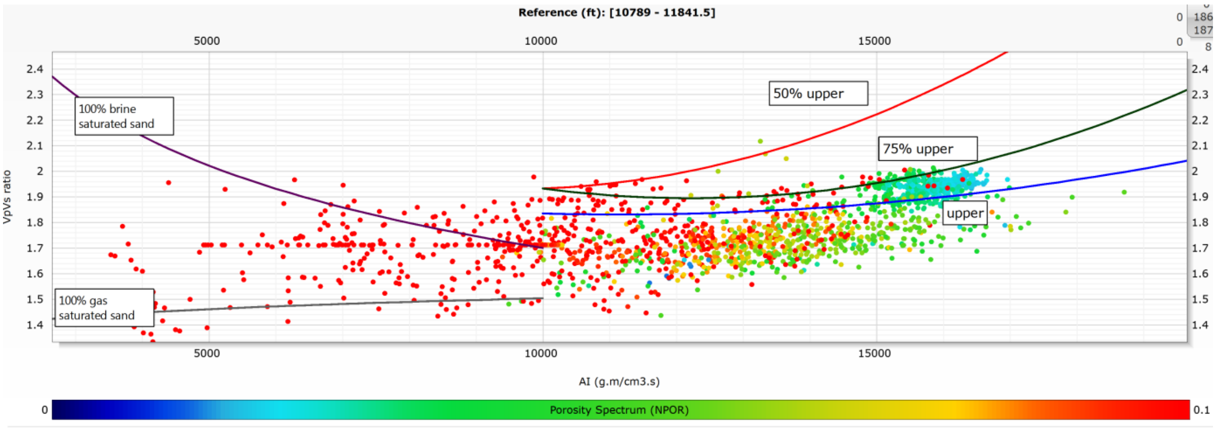

Figure 10.12. Displayed are well log data with calculated Hashin-Shtrikman upper bound for saturated (blue) samples and 75% (green) and 50% (red)of the saturated upper bound in v_p/v_s ratio versus acoustic impedance cross-plot. The points are colour coded using Neutron Porosity log.

10.4. Interpretation of elastic inversion results

In this part rock physics interpretation of elastic inversion results are demonstrated using the previously selected Rock Physics Template. The aim of this display is to be able to interpret efficiently the elastic properties inverted from seismic data in conjunction with a rock physics template, which in turn can be used to predict lithology and fluid content.

In this study, we simultaneously invert the P-velocity, S-velocity, and density using prestack seismic angle gathers. To predict and analyse the lithology and fluid contact, we derive acoustic impedance, shear impedance and v_p/v_s ratio, using the inverted velocities and density. With the posted rock physics template in the cross plots of the inverted elastic properties, we are able to analyse and interpret the final inversion results.

The following figures (Figure 10.13, 10.14 and 10.15) show the comparison between the sonic log data and the seismic data. Using the v_p/v_s ratio and acoustic impedance cross-plot with the appropriate Rock Physics Template, the borehole (well X-001) and seismic data are demonstrated in time domain.

Figure 10.13 illustrates our dataset that is colour coded by Clay Volume log. The borehole data show a good match with the RPT. Although the elastic inversion results represent some points with high clay volume, but also high acoustic impedance and low v_p/v_s ratio values.

In Figure 10.14, our dataset are colour coded by Water Saturation log. The borehole data show again a better fit with the RPT than the seismic data. However, the gas saturated seismic points obtain low acoustic impedance and v_p/v_s ratio values, which could assist to discriminate the pore fluid.

Figure 10.15 shows the borehole and seismic time domain dataset that are colour coded due to the effective porosity log. It is visible that the elastic inversion results may not be described perfectly with the previously defined RPT.

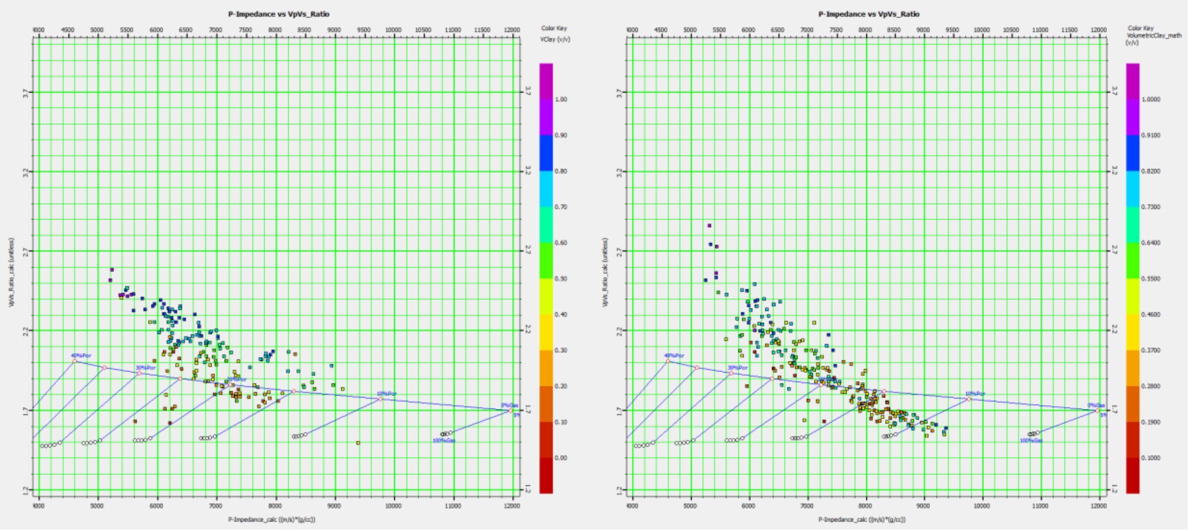

Figure 10.13. Displayed is time-domain sonic log data (left) and the seismic data (right) in v_p/v_s ratio versus acoustic impedance cross-plot with appropriate RPT. The data are colour coded using Clay Volume log.

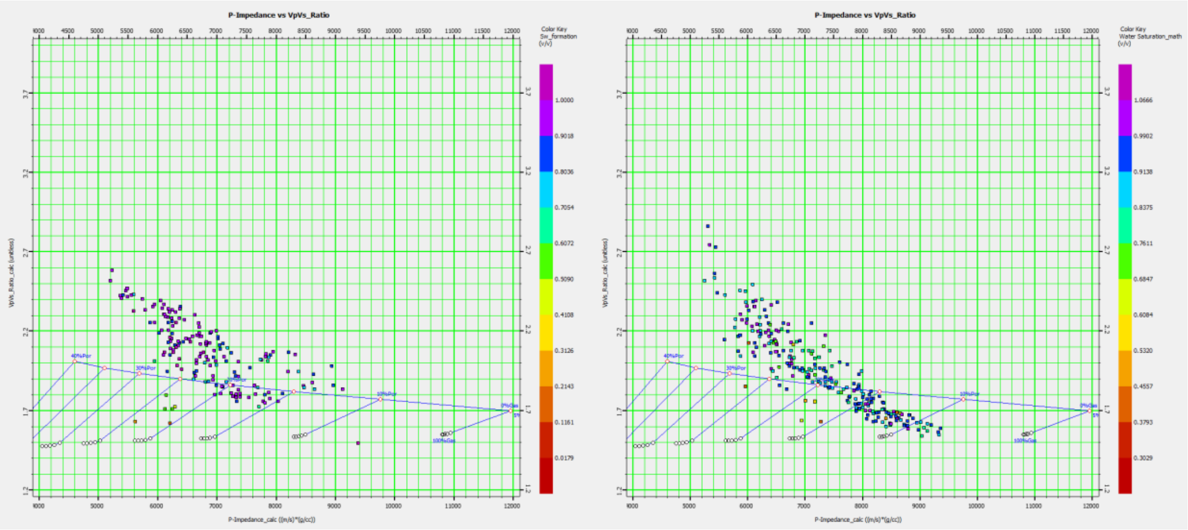

Figure 10.14. Displayed is time-domain sonic log data (left) and the seismic data (right) in v_p/v_s ratio versus acoustic impedance cross-plot with appropriate RPT. The data are colour coded using Water-Saturation log.

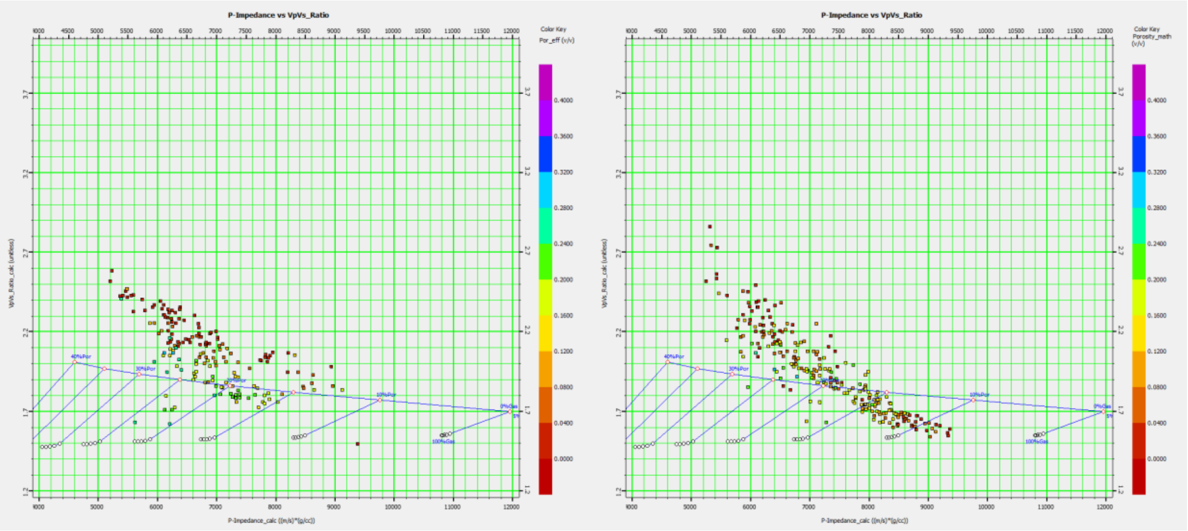

Figure 10.15. Displayed is time-domain sonic log data (left) and the seismic data (right) in v_p/v_S ratio versus acoustic impedance cross-plot with appropriate RPT. The data are colour coded using Effective Porosity log.

11. Discussion and conclusion

Elastic properties are determined for different carbonate types of Austria and for different sandstone and carbonate core plugs from the Vienna Basin in laboratory. Carbonates are of main interest not only for the oil industry but also for other geo-scientific fields like geothermal projects. However, carbonates offer still a lot of open question due to their diagenetic alterations that change the mineralogy and pore structure within the carbonate rocks.

Due to laboratory results, the carbonate and sandstone samples can be discriminated from each other easily. Furthermore, elastic properties of dry and saturated samples are investigated in laboratory. The carbonates show at the first sight the same shear weakening effect than presented by authors before. Some of them cite that this can be explained due to microporosity but there is no overall concept for this effect by now.

The main goal of this study is to construct an appropriate Rock Physics Template (RPT) for Vienna Basin using the available core samples, borehole data and seismic cube. To achieve a better understanding about the elastic properties of the investigated area, different model approaches was carried out.

The friable-sand and constant-cement models are performed in sandstone samples. The results of these model calculations, which are completed with Gassmann fluid substitution computation, provide the opportunity to correlate the laboratory data with the borehole data. The correlation shows a good match.

By carbonate samples Kuster and Toksöz inclusion model calculation is carried out to describe the pore shape of the samples. The result shows that different aspect ratios needed to be applied for different lithologies. Due to a possible different pore shape, two groups with two aspect ratios can be separated for the “Dachstein”-limestone. The “Haupt”-dolomite scatter too much, for using only one aspect ratio. The calculations were carried out for dry and water saturated samples. For the water-saturated calculations lower aspect ratios needed to be used.

In both cases (in sandstone and carbonate rocks) Hashin-Shtrikman bounds are used to compute the appropriate upper and lower bounds that characterize them properly. The calculated bounds show a good correlation in scale of laboratory and borehole data. Hashin-Shtrikman bounds are applied further to calculate the trend line for gas and brine saturated sandstones and used to characterize the carbonates in term of RPT.

The plot v_p/v_s ratio versus acoustic impedance, the rock physics template, showed good results. Compared with sandstone, the carbonates show higher acoustic impedance that can easily be explained with a higher density and higher compressional wave velocity. This is also a result from the low porosity. Clearly observable was the difference between brine saturated and dry samples. This is useful for the separation of gas and water parts in a borehole or in seismic data.

To describe this correlation the Hashin-Shtrikman bounds were used. For the saturated samples the calculated 75% and 50% of the upper bound showed good results and give the possibility for a data description. For the dry samples this method did not work sufficient. The upper and the 75% bounds can display the trends but not reach all data. Therefore, maybe other models need to be applied.

Additionally, well-log data are also used to calibrate/validate the RPTs before the interpretation of seismic data is performed. The calculated sandstone lines show a good result. The separation of gas and brine saturated rocks becomes visible. The porosity prediction is possible by sandstones. The characterization of carbonates is more difficult due to their more complex pore system. The Hashin-Shtrikman upper and the 75% bounds represent a good result, but pore fluid and porosity prediction is not possible.

Simultaneous AVO inversion was carried out that delivers absolute acoustic impedance, v_p/v_s (or shear impedance) and density cubes. The elastic inversion results were also used to verify the validity of the generated RPTs. The inversion result in terms of acoustic impedance and v_p/v_s ratio show a good match with the well log data. However, the match between the density inversion result and the well logs is considered weak. This can be explained due to the limited angle ranges and the far angle stacks, which are contributing to the density volume prediction, are lower frequency and noisier than the nearer angle stacks.

The inverted elastic properties of sandstone show a good correlation with well log data. Therefore, the selected RPT, which was constructed due to laboratory results and borehole data, is also used for interpretation of seismic data. It has to be mentioned that the elastic inversion results may not be described perfectly with the previously defined RPT.

The RPT technology has a broad range of application. Beside analysis of inverted elastic properties, it provides a good quality control of well log data and elastic inversion results.

Further studies should be performed in this topic to reach better results. More investigations of carbonates are required to achieve a better porosity and pore fluid prediction.

12. References

Avseth P., Dvorkin J., Mavko G., (1999) Rock physics diagnostics of North Sea sands: link between microstructure and seismic properties, *Geophysical Research Letters*, Vol. No. 27, 2761-2764.

Avseth P., Jørstad A., Van Wijngaarden A., Mavko G., (2009) Rock physics estimation of cement volume, sorting, and net-to-gross in North Sea sandstones, *The leading edge*, Vol. No. 28, 98-107.

Avseth P., Mukerji T., Mavko G., (2010) Quantitative Seismic interpretation, Applying Rock Physics Tools to Reduce Interpretation Risk, *Cambridge University Press*, 51-70, 101-110.

Ba j., Cao H., Carcione J., Tang G., Yan X.-F., Sun W.-T., Nie J., (2013) Multiscale rock-physics templates for gas detection in carbonate reservoirs, *Journal of Applied Geophysics*, Vol. No. 93, 77-82.

Bachmayer F., Brix F., (1980) Erdöl und Erdgas in Österreich, *Naturhistorischen Museum* (Wien), 147-172.

Baechle G., WegerR., Eberli G., Massaferro J.L., Sun Y., (2005) Changes of shear moduli in carbonate rocks: Implication for Gassmann applicability, *The leading edge*, Vol. No. 24, 507-510.

Chi X.-G., Han D.-H., (2009) Lithology and fluid differentiation using rock physics template, *The leading edge*, Vol. No. 28, 1424-1428.

Eberli G., Baechle G., Anselmetti F., Incze M. (2003) Factors controlling elastic properties in carbonate sediments and rocks, *The leading edge*, Vol. No. 22, 654-660.

Gegenhuber N., Steiner-Luckabauer C., (2012) v_p/v_S Automatic Picking of Ultrasonic Measurements and their Correlation of Petrographic Coded Carbonates from Austria, *74th EAGE Conference and Exhibition Copenhagen.*

Gomez J.P., Rai C.S., Sondergeld C.H.,(2007) Effect of Microstructure and Pore Fluid on the Elastic Properties of Carbonates, *SEG/San Antonio 2007 Annual Meeting*, 1565-1569.

Gupta S., Chatterjee R., Farooqui M., (2012) Rock physics template (RPT) analysis of well logs and seismic data for lithology and fluid classification in Cambay Basin, *International Journal of Earth Science*, Vol. No. 101, 1407-1426.

Kumar N., Negi S.S., (2012) Low frequency model and its impact on seismic inversion data, *9th Biennial International Conference & Exposition on Petroleum Geophysics*, 390.

Lucia F. J., (2007) Carbonate Reservoir Characterization, an Integrated Approach, *Springer.*

Mavko G., Mukerji T., Dvorkin J. (2011) The rock physics handbook, *Cambridge university press.*

Nair K. N., Kolbjørnsen O., Skorstad O., (2012) Seismic inversion and its applications in reservoir characterization, *First break*, Vol. No. 83, 83-86.

Ødegaard E., Avseth P.,(2004) Well log and seismic data analysis using rock physics templates, *First break*, Vol. No. 23, 37-43.

Rogen B., Fabricius I., Japsen P., Hoier C., Mavko G., Pedersen J., (2005) Ultrasonic velocities of North Sea chalk samples: influence of porosity, fluid content and texture, *Geophysical Prospecting*, Vol. No. 53, 481-496.

Schön J.H.,(2011) Physical properties of rocks, A workbook, *Elsevier*, 149-243.

Scotellaro C., Mavko G., (2008) Factors affecting the Sensitivity of the Elastic Properties of Pressure on Carbonate Rocks, *SEG Annual MeetingLas Vegas*, 1665-1669.

Sharma R., Prasad M., Katiyar G., Surve G., (2006) On the applicability of Gassmann Model in Carbonates, *6th International Conference & Exposition on Petroleum Geophysics*, Kolkata.

Sharma R., Prasad M., Batzle M, Vega S., (2011) Sensitivity of Elastic Properties to Fabric Heterogeneity in Carbonate Rocks, *Geophysical Prospecting*, Vol. No. 61, 270-286.

Sleeman R., Eck T., (1999) Robust automatic P-phase picking: an on-line implementation in the analysis of broadband seismogram recordings, *Phys. Of the Earth and Planet. Int,* Vol. No. 113, 265-275.

VeekenP.C.H., (2007) Seismic Stratigraphy, Basin Analysis and Reservoir Characterisation. Handbook of Geophysical Exploration. Vol. No. 37, *Elsevier.*

Wessely G., (2006) Geologie der österreichische Bundesländer: Niederösterreich, Geologie der österreichische Bundesländer, *Wien: Geologischen Bundesanstalt.*

White R., Simm R., Xu S., (1998) Well tie, fluid substitution and AVO modelling a North Sea example, *Geophysical Prospecting*, Vol. No. 46, 323-346.

Xu S., Payne M. (2009) Modelling elastic properties in carbonate rocks, *The leading edge*, Vol. No. 28, 66-74.

13. List of Figures

Figure 7.3. Displayed is bulk modulus for dry samples versus (effective) porosity, additionally displayed are the calculated lines from Hashin-Shtrikman (1963), (upper bound, lower bound, 0.5 upper bound and 0.75 upper bound).

Figure 7.4. Displayed is bulk modulus for saturated samples versus (effective) porosity, additionally displayed are the calculated lines from Hashin-Shtrikman (1963), (upper bound, lower bound, 0.5 upper bound and 0.75 upper bound).

Figure 7.5. Displayed is bulk modulus versus effective porosity for borehole data that is colour coded by Water-Saturation. Hashin-Shtrikman lower and upper bounds are also represented.

Figure 7.6. Displayed is v_p for dry samples versus (effective) porosity, additionally displayed are the calculated lines from Kuster and Toksöz (1974), for different aspect ratios (0.2, 0.1, 0.05, 0.025, 0.01, 0.005).

Figure 7.7. Displayed is v_S for dry samples versus (effective) porosity, additionally displayed are the calculated lines from Kuster and Toksöz (1974), for different aspect ratios (0.2, 0.1, 0.05, 0.025, 0.01, 0.005).

Figure 7.8. Displayed is v_p for saturated samples versus (effective) porosity, additionally displayed are the calculated lines from Kuster and Toksöz (1974), for different aspect ratios (0.2, 0.1, 0.05, 0.025, 0.01, 0.005).

Figure 7.9. Displayed is v_S for saturated samples versus (effective) porosity, additionally displayed are the calculated lines from Kuster and Toksöz (1974), for different aspect ratios (0.2, 0.1, 0.05, 0.025, 0.01, 0.005).

Figure 7.10. Displayed is compressional velocity versus effective porosity for borehole data, additionally displayed are the calculated lines from Kuster and Toksöz (1974), for different aspect ratios (0.2, 0.1, 0.05, 0.025, 0.01, 0.005) (blue lines) and the Time-average equation (green).

Figure 7.11. Displayed is the calculated bulk modulus based on the laboratory measurements and using the Gassmann equation.

Figure 7.12. Measured compressional (left) and shear (right) velocity versus calculated compressional and shear velocity using the Gassmann equations.

Figure 7.13. Display of changing shear moduli and its effect on velocity prediction of saturated rocks using Gassmann´s equation.

Figure 8.1. Gas reservoirs detection using neutron, density and resistivity logs.

Figure 8.2. Separation of oil and water saturated reservoirs using well logs.

Figure 8.3. Bulk density versus neutron cross plot, additionally displayed are the lithology lines and the impact of gas and shale content.

Figure 8.4. Bulk density log versus neutron log, additionally displayed are different formations which represents well the lithology lines.

Figure 8.5. Density-neutron plot, the data points are colour coded using the Gamma Ray log.

Figure 8.6. Density-neutron plot, displayed is the interpretation of the pore fluids.

Figure 9.1. Fundamental inversion workflow for seismic data (Schlumberger, 2007).

Figure 9.2. Parameters of sampling window by Trim Statics process.

Figure 9.3. Displayed offset gathers before (left) and after (middle) alignment. Additionally, displayed the offset gathers after alignment (right) that are colour coded by angle incident.

Figure 9.4. Ray paths for traces for offset and angle gathers.

Figure 9.5. Offset gathers before (left) and after (middle) alignment. Additionally, displayed the angle stack gathers (right).

Figure 9.6. Fundament of theory of well to seismic tie.

Figure 9.7. Displayed the extracted wavelets.

Figure 9.8. Displayed P-wave, density, acoustic impedance and computed reflectivity logs of X-001 well. Moreover, displayed are the synthetic seismogram, the seismic volume and the cross-correlation window.

Figure 9.9. Displayed P-wave, density, acoustic impedance and computed reflectivity logs of X-016 well. Moreover, displayed are the synthetic seismogram, the seismic volume and the cross-correlation window.

Figure 9.10. Displayed our amplitude spectrum with the predicted low pass filter, additionally displayed are the theory behind the building of a low frequency model.

Figure 9.11. Displayed the generated acoustic impedance model with the inserted well path and the acoustic impedance log (left) and the seismic volume (right).

Figure 9.12. Displayed the generated v_p/v_S ratio model with the inserted well path and the v_p/v_S ratio log (left) and the seismic volume (right).

Figure 9.13. Displayed the generated density model with the inserted well path and the density log (left) and the seismic volume (right).

Figure 9.14. Displayed the generated acoustic impedance model with the inserted well path and the acoustic impedance log (left) and the acoustic impedance volume derived from the simultaneous AVO inversion process with the inserted well path and the corresponding well logs (right).

Figure 9.15. Displayed the generated v_p/v_S ratio model with the inserted well path and the v_p/v_S ratio log (left) and the v_p/v_S ratio volume derived from the simultaneous AVO inversion process with the inserted well path and the corresponding well logs (right).

Figure 9.16. Displayed the generated density model with the inserted well path and the density log (left) and the density volume derived from the simultaneous AVO inversion process with the inserted well path and the corresponding well logs (right).

Figure 9.17. Inversion results versus well log data: acoustic impedance, v_p/v_S ratio and density, using X-001 and X-016 wells for correlation.

Figure 9.18. Displayed sonic, acoustic impedance, v_p/v_S ratio and density logs of X-001 well. Additionally, seismic traces represent the simultaneous AVO inversion results (acoustic impedance, v_p/v_S ratio and density volumes) with inserted corresponding logs.

Figure 9.19. Displayed sonic, acoustic impedance, v_p/v_S ratio and density logs of X-016 well. Additionally, seismic traces represent the simultaneous AVO inversion results (acoustic impedance, v_p/v_S ratio and density volumes) with inserted corresponding logs.

Figure 10.6. Cross-plot v_p/v_s versus acoustic impedance AI, drawn after a figure „Rock Physics Template" from Ødegaard and Avseth (2004). „The theoretical trends are shown for idealized silici-clastic lithologies. The effects of changing reservoir parameters on a point of the crossplot is here shown by arrows" (Ødegaard and Avseth, 2004).

Figure 10.2. Illustration of three-step approach for modelling the effective moduli of sand, additionally the results of these model calculations is displayed to characterize our data set.

Figure 10.3. Displayed is the calculated water (blue) and gas (red) saturated sand-lines in the v_p/v_S ratio versus AI cross-plot. Furthermore, the points on the line illustrate the changing porosity.

Figure 10.4. Displayed is v_p/v_S ratio versus acoustic impedance for dry and saturated carbonate and sandstone samples, additionally displayed the areas where the sandstone (dry, saturated) and shale would be positioned.

Figure 10.5. Displayed is v_p/v_S ratio versus acoustic impedance for borehole data that colour coded by lithology. Separation of the lithology becomes clearly visible.

Figure 10.6. v_p/v_S ratio versus acoustic impedance with calculated 100% water and gas saturated lines for sand, additionally with the calculated Hashin-Shtrikman bounds (upper bound, 75% and 50% of the upper bound) and displayed also are dry and water saturated sandstone and carbonate samples.

Figure 10.7. v_p/v_S ratio versus acoustic impedance cross-plot, with theoretical rock physics trend for clean compacted brine filled quartz sand superimposed. The trend is plotted as function of porosity. The effects of different gas saturations are added below the brine sand trend. The data are colour coded using the Clay Volume log.

Figure 10.8. v_p/v_S ratio versus acoustic impedance cross-plot, with theoretical rock physics trend for clean compacted brine filled quartz sand superimposed. The trend is plotted as function of porosity. The effects of different gas saturations are added below the brine sand trend. The data are colour coded using the Water Saturation log.

Figure 10.9. v_p/v_S ratio versus acoustic impedance cross-plot, with theoretical rock physics trend for clean compacted brine filled quartz sand superimposed. The trend is plotted as function of porosity. The effects of different gas saturations are added below the brine sand trend. The data are colour coded using the Effective Porosity log.

Figure 10.10. Displayed are well log data with calculated Hashin-Shtrikman upper bound for saturated and dry samples and 75% and 50% of the saturated upper bound in v_p/v_S ratio versus acoustic impedance cross-plot. The points are colour coded using Neutron Porosity log.

Figure 10.13. Displayed are well log data with calculated Hashin-Shtrikman upper bound for saturated (blue) samples and 75% (green) and 50% (red) of the saturated upper bound in v_p/v_S ratio versus acoustic impedance cross-plot. The points are colour coded using Gamma Ray log.

Figure 10.14. Displayed are well log data with calculated Hashin-Shtrikman upper bound for saturated (blue) samples and 75% (green) and 50% (red)of the saturated upper bound in v_p/v_s ratio versus acoustic impedance cross-plot. The points are colour coded using Neutron Porosity log.

Figure 10.13. Displayed is time-domain sonic log data (left) and the seismic data (right) in v_p/v_S ratio versus acoustic impedance cross-plot with appropriate RPT. The data are colour coded using Clay Volume log.

14. List of Table